Distribution Category:
Coal Conversion and Utilization--
Coal Science and Analysis (UC-90a)

ANL/FE-86-4

ANL/FE--86-4

DE87 004556

ARGONNE NATIONAL LABORATORY
9700 South Cass Avenue
Argonne, Illinois 60439

PARTICLE VELOCITY AND SOLID VOLUME FRACTION MEASUREMENTS WITH A NEW CAPACITIVE FLOWMETER AT THE SOLID/GAS FLOW TEST FACILITY

by

J. P. Bobis, K. G. A. Porges, A. C. Raptis,
W. E. Brewer, and L. T. Bernovich

Materials and Components Technology Division

August 1986

DISCLAIMER

This report was prepared as an account of work sponsored by an agency of the United States Government. Neither the United States Government nor any agency thereof, nor any of their employees, makes any warranty, express or implied, or assumes any legal liability or responsibility for the accuracy, completeness, or usefulness of any information, apparatus, product, or process disclosed, or represents that its use would not infringe privately owned rights. Reference herein to any specific commercial product, process, or service by trade name, trademark, manufacturer, or otherwise does not necessarily constitute or imply its endorsement, recommendation, or favoring by the United States Government or any agency thereof. The views and opinions of authors expressed herein do not necessarily state or reflect those of the United States Government or any agency thereof.

Prepared for U. S. Department of Energy
Office of Fossil Energy, Morgantown Energy Technology Center
under Advanced Research
in Instrumentation and Control Technology
FTP 49644

MASTER

DISTRIBUTION OF THIS DOCUMENT IS UNLIMITED

CONTENTS

	Page
LIST OF FIGURES	iv
LIST OF TABLES	vi
LIST OF ABBREVIATIONS AND SYMBOLS	vii
ABSTRACT	1
1. INTRODUCTION	1
2. DESCRIPTION OF EXPERIMENT	3
2.1 S/GFTF (Solid Gas Flow Test Facility) Test Facility	3
2.2 S/GFTF On-line Irradiated Particle Velocimeter	6
2.3 Summary of Experimental Tests	13
3. CAPACITIVE INSTRUMENTS	17
3.1 Design Basis	17
3.2 Capacitive Flowmeter	30
3.2.1 Description	30
3.2.2 Capacitive Flowmeter Signal Conditioning Instrumentation	30
3.2.3 Data Analysis and Reduction Techniques	36
3.3 Densitometer	39
3.3.1 Description	39
3.3.2 Densitometer Signal Conditioning Instrumentation	39
4. EXPERIMENTAL RESULTS	41
4.1 Solid Volume Fraction	41
4.1.1 Capacitive Flowmeter	43
4.1.2 Densitometer	45
4.2 Particle Velocity	47
4.3 Mass Flowrate	53
5. SUMMARY AND CONCLUSION	55
ACKNOWLEDGMENTS	56
APPENDIX A. THE BULK DIELECTRIC CONSTANT OF UNIFORM MIXTURES	57
APPENDIX B. EFFECT ON NONUNIFORM SOLIDS DISTRIBUTION ON THE CAPACITIVE DENSITOMETER READOUT	66
APPENDIX C. THE CROSS-CORRELATION FUNCTION WITH CAPACITIVE SENSING IN GAS-ENTRAINED PARTICLE FLOW	73
APPENDIX D. THE EFFECT OF A LINER ON THE CAPACITIVE FLOWMETER SOLID VOLUME FRACTION MEASUREMENT	80
APPENDIX E. AMPLITUDE DEMODULATED SIGNAL THEORY FOR PARTICLE VELOCITY MEASUREMENT WITH A CAPACITIVE FLOWMETER	82
REFERENCES	83

LIST OF FIGURES

No.	Title	Page
2.1.1	Solid/Gas Flow Test Facility (S/GFTF) at ANL	4
2.1.2	S/GFTF Solid Control Valve Transfer Function	5
2.1.3	S/GFTF Unload/Reload Modes	5
2.1.4	S/GFTF Data Acquisition System	7
2.2.1	S/GFTF Irradiated Particle Trickle Feeder	9
2.2.2	Typical Irradiated Particle Count Rate Distribution	10
2.2.3	Gamma Detectors at the Capacitive Flowmeter	11
2.2.4	Gamma Detectors at the Densitometer	12
2.3.1	Arrangement of Flow Instruments in Solid/gas Test Section of the S/GFTF	14
3.1.1	Annular Electrode Capacitor	18
3.1.2	Wrapped Electrode Capacitor	18
3.1.3	Narrow Electrode Capacitor, ANL-I Version	19
3.1.4	Overall Interior View of Capacitive Flowmeter, ANL-I Version	20
3.1.5	Capacitive Flowmeter Spoolpiece, ANL-I Version	20
3.1.6	Increased Wrapped Electrode Capacitor, ANL-II Version, with Guard-Equipped Signal Electrode	21
3.1.7	Generalized Capacitor Geometry Showing Effect of Electrode Curvature	25
3.2.1	Overall Interior View of Capacitive Flowmeter, ANL-II Version	31
3.2.2	Close-up View of Capacitive Flowmeter Electrodes and Guard	31
3.2.3	Capacitive Flowmeter Electrode Configuration for Electrodes on the Outside Surface of the Ceramic Tube	32
3.2.4	Capacitive Flowmeter Current-Sensing Electronics for Measuring Solid Volume Fraction and Particle Velocity	35
3.2.5	Capacitive Flowmeter Current-Sensing Preamplifier	35
3.2.6	Amplitude Demodulator for Capacitive Flowmeter Signals	37
3.2.7	S/GFTF Data Analysis System for Flow Instrumentation	37
3.3.1	Densitometer Electrode Configurations	40
3.3.2	Capacitive Measuring Circuit for the Densitometer	40
4.1.1	Capacitive Flowmeter Solid Volume Fraction Signal for a Range of Solid Volume Fraction Values	44

LIST OF FIGURES (Contd.)

No.	Title	Page
4.1.2	Densitometer Capacitance of a Range of Solid Volume Fraction Values	46
4.2.1	Typical Capacitive Flowmeter Measured Cross-correlation Functions at (1) M_s = 3.2 lb/s and V_p = 25.1 m/s and (2) M_s = 4.4 lb/s and V_p = 24.0 m/s for 4, 8 and 12 cm Spaced Electrodes	49
4.2.2	Typical Capacitive Flowmeter Measured Cross-correlation Function With and Without 71 H_z High Pass Filter at M_s = 4.4 lb/s and SGL = 22 for 8 cm Spaced Electrodes	49
4.2.3	Correlation Coefficient for Various Electrode Separations Used for the Capacitive Flowmeter Measured Particle Velocity for a Range of Solid Volume Fractions Values	50
4.2.4	Typical Capacitive Flowmeter Measured Cross-correlation Functions for 1, 2, and 4 Averaged Cross Correlations at M_s = 3.2 lb/s and SGL = 16 for 8 cm Spaced Electrodes	52
4.2.5	Capacitive Flowmeter Measured Particle Velocity vs Irradiated Particle Velocity	53
4.3.1	Capacitive Flowmeter Measured Solid Mass Flowrate for a Range of Solid Feedrates	54
B.1	Solid Density Gradient as a Function of Scale Parameter β	68
B.2	Parallel Vertical Plate Capacitor With Nonuniform Distribution of Solids	68
B.3	Parallel Horizontal Plate Capacitor With Nonuniform Distribution of Solids	71

LIST OF TABLES

No.	Title	Page
2.1.1	Typical DAS Channel Allocation for the S/GFTF.....	7
2.3.1	Test Section Locations of Flow Instruments and Gamma Detectors.....	14
2.3.2	Summary of S/GFTF Flow Test Conditions and Measured Results of all Test Instruments.....	15
2.3.3	Typical Physical and Chemical Properties of the Glass Beads Used in the S/GFTF Solid/Gas Flow Tests.....	16
2.3.4	Sieve Analysis of Glass Beads Used in the S/GFTF Solid/Gas Flow Tests.....	17
3.2.1	Characteristics of Capacitive Flowmeter Electrodes.....	33
3.2.2	Typical Physical Properties of the Mullite Liner Used for the Capacitive Flowmeter.....	33
3.2.3	Typical Analog Magnetic Tape Recorder Channel Allocation....	38
3.2.4	Typical Setup Conditions for the Digital Signal Processor...	38
3.3.1	Characteristics of Densitometer Electrodes.....	40
4.1.1	Statistical Errors for the Solid Volume Fraction Measurement.....	44
4.1.2	Capacitive Flowmeter Solid Volume Fraction Signal for a Range of Solid Volume Fraction Values.....	44
4.1.3	Densitometer Capacitance for a Range of Solid Volume Fraction Values.....	46
4.2.1	Correlation Coefficient for Various Electrode Separations Used for the Capacitive Flowmeter Measured Particle Velocity for a Range of Solid Volume Fraction Values.....	51
4.2.2	Capacitive Flowmeter Measured Particle Velocities for a Range of Irradiated Particle Velocities.....	52
4.3.1	Capacitive Flowmeter Measured Solid Mass Flowrate for a Range of Solid Feedrates.....	54
A.1	Model Formulas for Solids Suspended in Fluid.....	65
B.1	Model Formulas for Analysis of Nonuniform Solid Distribution in the Capacitive Flow Instrument.....	69
B.2	Bulk Capacitance Error for a Nonuniform Solid Distribution in a Vertical and Horizontal Parallel Plate Capacitor.....	72

LIST OF ABBREVIATIONS AND SYMBOLS

A	Area of parallel plate capacitor (cm^2)
A_g	Total amplifier gain in particle velocity channel
A_{gd}	Amplifier gain in downstream channel
A_{gu}	Amplifier gain in upstream channel
A_p	Pipe cross-sectional area (cm^2)
AC	Acoustic flowmeter
ACF	Auto-correlation function
A/D	Analog to digital
ANL	Argonne National Laboratory
ATSR	Argonne Thermal Source Reactor
b	Collective parameter (Eq. C.12)
B	Dielectric constant parameter (Eq. B.8)
BCD	Binary coded decimal
c	Duct-averaged concentration (Eq. 3.1.7)
CCF	Cross-correlation function
CF	Capacitive flowmeter
C_F	Densitometer capacitance with gas (without solids) (pF)
C_F^*	Capacitive flowmeter capacitance with gas (without solids) (pF)
C_M	Densitometer capacitance with solids and gas (pF)
C_M^*	Capacitive flowmeter capacitance with solids and gas (pF)
C_{MH}	Horizontal plate capacitance with nonuniform solid distribution (pF)
C_{Mi}	Capacitive flowmeter capacitance with solids and gas measured at t_i (pF)
C_{MV}	Vertical plate capacitance with nonuniform solid distribution (pF)
C_m	Liner capacitance (pF)
d	Liner wall thickness (cm)

LIST OF ABBREVIATIONS AND SYMBOLS (Contd.)

D	Electrode separation (cm)
d_e	Electrode separation in direction of flow (cm)
d_p	Particle diameter
D/A	Digital to analog
dN_i	Number of particles in the ith sample
DAS	Data acquisition system
DC	Direct current
$d\phi$	Variation in solid volume fraction
DM	Densitometer
dM_s	Variation in solid feedrate (lb/s)
DSP	Digital signal processor
dv_p	Variation in particle velocity (m/s)
E	Local field for elementary capacitor (V/m)
E_{appl}	Applied electric field (V/m)
E_{loc}	Electric field at molecule (V/m)
f	Frequency (H_z)
F	Solid volume fraction density scale adjustment (defined by Eq. B.2)
FM	Frequency modulated
f_s	Sampling frequency (H_z)
g	Dielectric constant ratios defined by Eq. 3.1.20
G	Dielectric constant ratios defined by Eq. 3.1.19
G_g	Relative change in capacitance for a particular model (Eq. B.5)
h	Height above bottom plane of rectangular duct
H	Rectangular duct height
H_s	Dispersion parameter (Eq. 3.1.7)
I	Capacitive flowmeter current (μA)

LIST OF ABBREVIATIONS AND SYMBOLS (Contd.)

ID	Pipe inner diameter (cm)
I/V	Current-to-voltage converter
K	Medium dielectric constant
K_f	Fluid dielectric constant
K_ℓ	Liner dielectric constant
K_m	Solid/Gas dielectric constant
K_o	Sample number offset
K_{RS}	Dielectric constant parameter (Eq. C.1)
K_s	Solid dielectric constant
KV	Knife valve
LDA	Laser Doppler anemometry
LSD	Least significant digit
m	Defined by Eq. C.5
M_s	Solid feedrate (lb/s)
MSD	Most significant digit
n	Local particle number density
$\bar{N}$	Average number of particles in detection volume
n_l	Number of induced molecular dipoles for component l
$\bar{N}_D$	Average number of particles at downstream electrode
n_m	Number of induced molecular dipoles
N(t)	Number of particles in detection volume
$\bar{N}_u$	Average number of particles at upstream electrode
N_{ui}	Particle sample at upstream detector at the ith time
OD	Outer diameter
p	Polarization per unit volume of molecular dipole
P	Polarization per unit volume

LIST OF ABBREVIATIONS AND SYMBOLS (Contd.)

P_g	Gauge pressure (psi)
PV_{CF}	Capacitive flowmeter particle velocity (m/s)
PV_{IP}	Irradiated particle velocity (m/s)
r	Pipe radius (cm)
s	Seconds (s)
S(t)	Arbitrary function of time
SGFTF	Solid/Gas Flow Test Facility
SGL	Solid/Gas loading
S_d	Upstream signal
S_u	Downstream signal
SVF	Solid volume fraction
t_p	Measured transit time (s)
$\bar{u}$	Average random velocity of particles
V_D	Detection volume
V_o	Current-to-voltage converter output (volts)
V_{osc}	Oscillator voltage (volts)
V_p	Particle volume
V_{pk}	Oscillator peak voltage (volts)
$\bar{v}_p$	Average particle velocity (m/s)
v_p	Particle velocity (m/s)
x	Normalized distance from duct bottom plane
X(t)	Time domain signal 1
Y(t)	Time domain signal 2
z	Distance variable
Z	Sensor location
α	Molecular polarizability

β	Scale parameter for density gradient
δ_i	Defined by Eq. C.18
ΔA	Elementary capacitor electrode area
ΔC	Capacitive flowmeter incremental change in capacitance (pF)
ΔC_M	Elementary capacitance in solid/gas flow model
ΔN_i	In-scattering for the ith sample
ΔP	Differential pressure (psi)
Δs	Elementary capacitor electrode separation
ΔV	Potential step
ε_ϕ	Relative error in solid volume fraction
ε_{m_s}	Relative error in solid feedrate
ε_{v_p}	Relative error in particle velocity
ρ_s	Solid (glass) density (gm/cm^3)
ρ_{ud}	Cross-correlation coefficient between upstream and downstream signals
ρ_{xy}	General cross-correlation coefficient
σ	Collision cross section
σ_F^2	Variance of C_F
σ_{CM}^2	Variance of C_M
σ_G^2	Variance of relative change in densitometer capacitance for solid volume fraction measurement
σ_M^2	Variance of M_s
σ_v^2	Variance of v_p
σ_ϕ^2	Variance of ϕ
ϕ	Solid volume fraction
$\bar{\phi}$	Average solid volume fraction
ω	Radian frequency (rad/s)

PARTICLE VELOCITY AND SOLID VOLUME FRACTION MEASUREMENTS WITH A NEW CAPACITIVE FLOWMETER AT THE SOLID/GAS FLOW TEST FACILITY

by

J. P. Bobis, K. G. A. Porges, A. C. Raptis,
W. E. Brewer and L. T. Bernovich

ABSTRACT

The performance of a new capacitive flowmeter has been assessed experimentally in a gas-entrained solid flow stream at the Argonne National Laboratory (ANL) Solid/Gas Flow Test Facility (S/GFTF) for solid feedrates in the range of 0.5 to 2 kg/s and solid-gas loadings up to 22, corresponding to a range of solid volume fractions extending from 0.004 to 0.016. Two types of nonintrusive instruments using the capacitive principle were fabricated at ANL and installed in the horizontal leg of a 12.3 m test section to sense the solids. An improved electrode geometry designed to maximize the coverage of the duct interior while minimizing the readout error due to a nonuniform electric field, was incorporated for one spoolpiece with the sensing electrodes on the outside surface of a ceramic liner and for another spoolpiece with the sensing electrodes mounted flush with the duct inside surface.

The capacitive instruments measured the solid volume fraction and the average particle velocity. The results are compared with time-of-flight measurements of short-lived radioactive particles that duplicate closely the size and density of the 1000μ glass beads used in these flow tests. Results show that the solid volume fraction measurements agree with the theoretical models presented and that the particle velocity deduced from the cross-correlation scheme agreed to within 5% of the irradiated particle velocity technique for the 21 to 31 m/s range generated with the S/GFTF.

1. INTRODUCTION

Solid/gas mass flow measurement is essential for pneumatic conveyors used in the chemical processing industry and for coal feed/return lines in a coal conversion or combustion plant where the coal is converted into process gas as the first step in conversion to pipeline gas or liquid fuel. An accurate reading of the feedrate in that important application is required for control of the energy and mass balances of the process feedback and hence for enhancement of the cost effectiveness of coal gasification/liquefaction. Conventional flow instruments are mostly intrusive devices

that suffer severe plugging problems, are unable to withstand the abrasive environment, and are not built to handle media with complex flow characteristics.

This report covers the development of a new capacitive flowmeter that produces the solid component mass flowrate of a gas-entrained solid on an absolute basis, without calibration or meter factor. Presented is a series of tests at the ANL Solid/Gas Flow Test Facility to evaluate the flowmeter performance in measuring the solid volume fraction and particle velocity. In combining these data to yield the component mass flowrate, only the solid component intrinsic density and dielectric constant and the duct cross-sectional area are required.

Two types of nonintrusive instruments using the capacitive principle to sense the solids were installed in the downstream section of the horizontal test section. One was a spoolpiece with the electrodes on the outside of a ceramic liner and was used to measure the particle velocity and solid volume fraction (SVF). The other was a spoolpiece with the electrodes on the inside duct surface and was used to measure the solid volume fraction. However, special circumstances that apply over the usual range of feedrates encountered in pneumatic conveyance allow the use of theoretical formulations yielding absolute values of the solid feedrate if certain sensing geometry conditions can be met. This led to the design of a specific electrode configuration whose efficacy was the main objective of the test. To provide the needed accuracy in a comparison measurement, a tagged particle scheme was developed, making use of short-lived radioactive gamma emission of fabricated particles that duplicate closely the size and density of the 1000μ glass beads used in these flow tests. Short-lived radioactivity satisfied stringent safety regulations while providing a high level of activity per particle, thus enabling accurate particle velocity measurements in the test series, which generally took 4-6 hours. This scheme was especially convenient because the ANL Thermal Source Reactor (ATSR) is located in the same building as the S/GFTF test loop used in this work.

Section 2 of this report describes the S/GFTF, the test conditions, and the irradiated particle velocimeter. Section 3 describes the signal conditioning and analysis instrumentation and sets forth the design basis of the capacitive flowmeter, along with the theoretical basis of the SVF and particle velocity measurement. The test results are presented in Section 4 and are compared with the average irradiated particle velocity and the SVF inferred from the measured solid feedrate and particle velocity. Section 5 presents conclusions of this work.

2. DESCRIPTION OF EXPERIMENT

2.1 S/GFTF TEST FACILITY

S/GFTF, shown in Fig. 2.1.1, is designed for use in developing, testing, and evaluating the calibration of flow instruments, and for use in studies on particulate flow[1]. The S/GFTF is a closed system operating at gas temperatures up to 50°C and pressures up to 34-68 kPa (5-10 psi) above atmospheric pressure. Solids, such as 500μ polystyrene or 50, 300, or 1000μ glass beads, are conveyed in dry air through a 5.2 or 7.8 cm (2 or 3 in.) schedule 40 pipe. Solid feedrates in the range of 0.14-2 kg/s (0.3-4.4 lb/s) and solid/gas loadings (SGL) of up to 22 can be maintained in the dilute phase test regions. The main elements of the S/GFTF are:

1. Two storage hoppers mounted on electronic scales for direct readout of solid weights; each hopper is capable of storing 450 kg (990 lb) of solid.

2. Valves for varying the solid feedrate from each hopper and a valve in the gas bypass line for varying the gas flowrate. The feed hopper and gas flowrate valves are each coupled to a linear differential transformer for generating a DC voltage proportional to the valve position with a 1.42 v/cm (3.6 v/in.) sensitivity as shown in Fig. 2.1.2.

3. Rotary blower and sensors for measuring the gas flowrate, temperature, and loop pressures in the gas and solid/gas lines. The rotary blower is powered with a 20 hp motor, and gas flowrates range from 0.071 to 0.165 m^3/s (150-350 CFM) at 41.4 kPa (6 psig).

4. Five pneumatic diverter valves, labeled A1-A5, (Fig. 2.1.3), that are remotely operated from the control panel, allow the operator to place S/GFTF in unload or reload mode. In the unload mode, valves A1-A5 are open, closed, closed, closed, and open, respectively, and the contents of the feed hopper (hopper 1) are transferred through the test section to hopper 2. In the reload mode the contents of hopper 2 are transferred to hopper 1, with valves A1-A5 in the closed, open, open, open, closed positions respectively. During the first reload, the irradiated particles are injected into the vertical line and the solids are transferred to the feed hopper.

5. A regulated air supply scheme for pressurizing hopper 1 to enhance the downflow of solids in the vertical dense-phase test section.

A typical operational state of S/GFTF is shown in Fig. 2.1.3. A 7.6 cm (3 in.) knife valve (KV), operated from the control panel, permits the quantity of solids delivered from the vertical dense phase flow section to be varied. A 5.08 cm (2 in.) mixing tee, with no internal jet wedges, com-

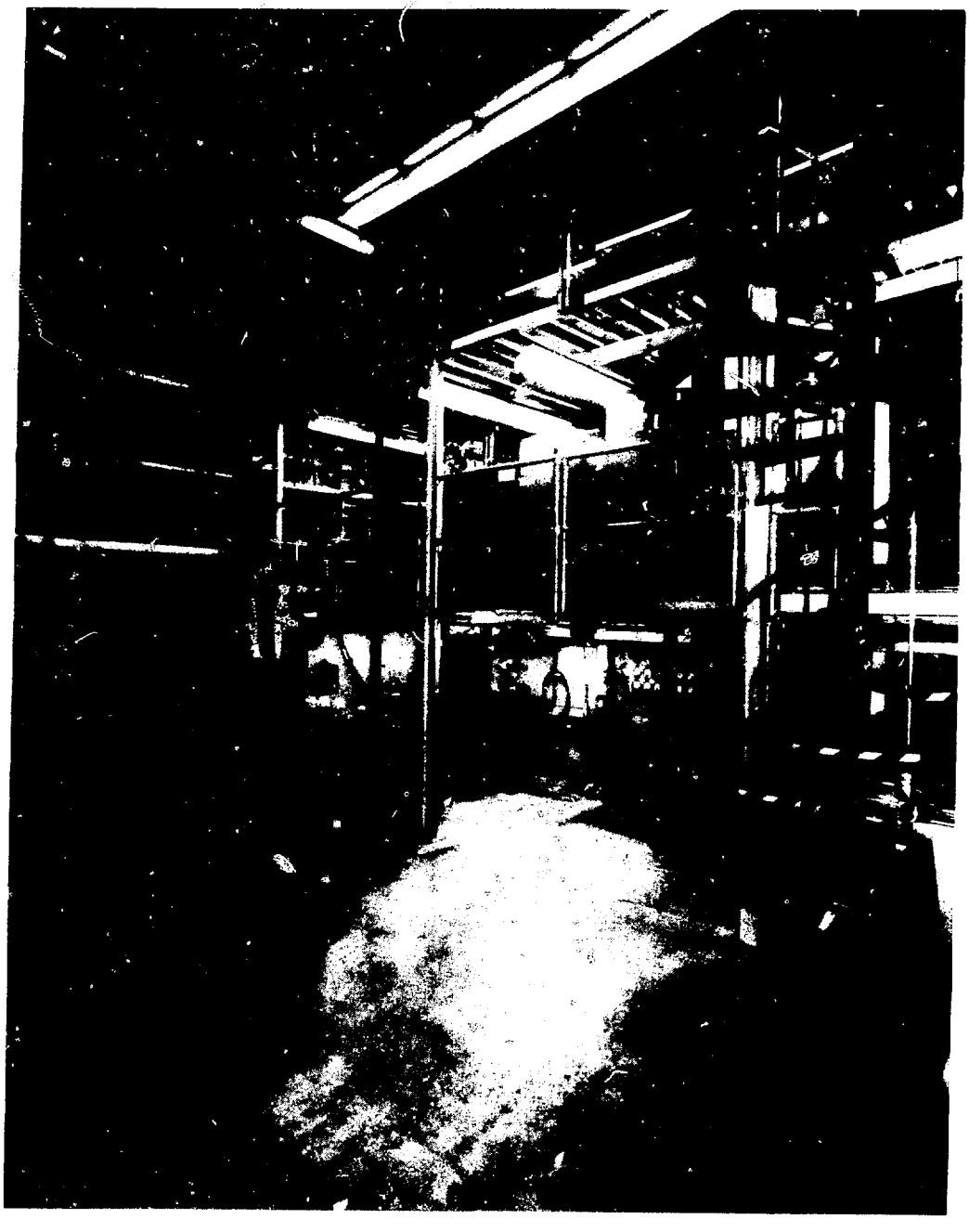

Fig. 2.1.1. Solid/Gas Flow Test Facility (S/GFTF) at ANL

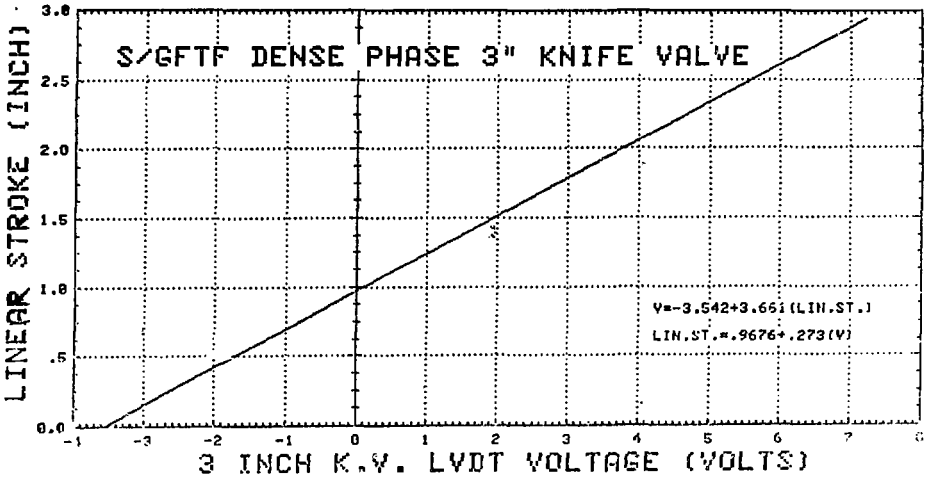

Fig. 2.1.2. S/GFTF Solid Control Valve Transfer Function

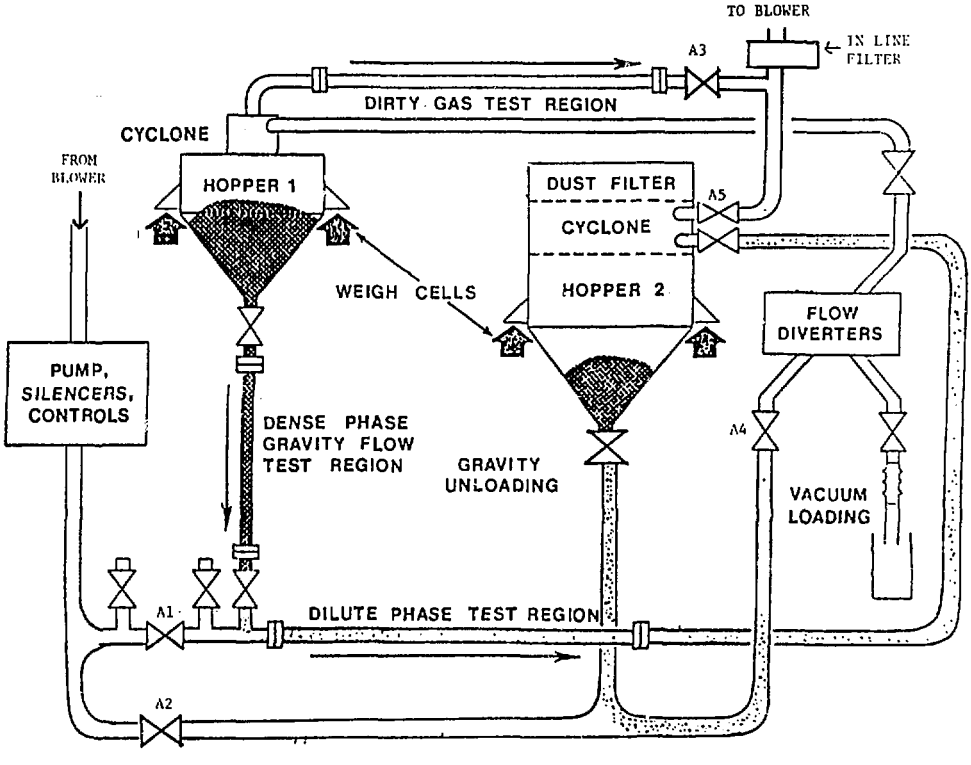

Fig. 2.1.3. S/GFTF Unload/Reload Modes

bines the solids and air, and the solid/gas flow stream is conveyed pneumatically through the 12.3 m (40.4 ft.) long horizontal test section. The gas velocity is controlled, also from the control panel, in a manual or automatic mode by means of a bypass valve and process controller which shunt the air from the loop. The solid/gas media during the unload mode are returned to hopper 2 through the test section; and the time to empty hopper 1 ranges from 15 to 3 min for the 0.5 to 2.0 kg/s (1 to 4.4 lb/s) range of solid feedrates. After hopper 1 is completely unloaded, the diverter valves are altered via the control panel and the contents of hopper 2 are reloaded into hopper 1 in 15 min.

The parameters measured by the data acquisition system (DAS), shown in Fig. 2.1.4, are the hopper weights, solid control valve position, gas velocity control signal, gas temperature, gauge and differential pressures in the gas and solid/gas lines, and the CF SVF signal. A typical channel allocation for the DAS is shown in Table 2.1.1. These analog signals are scanned as fast as a complete scan per second, by a 16 channel, 0-5 v analog-to-digital (A/D) converter system and stored in a user named disk file with the software program, SGDIS6. The loop operator can monitor, in real time via the computer terminal, the solid mass flowrate of the solids in each hopper and the instantaneous values of the gas flowrate, temperature, SGL, loop pressure, and SVF signals from the flow instruments. When the unloading of the feed hopper (hopper 1) is complete, the software program, SGDIS5, for any selected time interval, generates time plots of all analog signals, calculates their mean and standard deviation, and generates engineering units of measured voltage signals. The DAS determines the difference in hopper weight over the selected sampling time interval in the range of 3 to 20 s and calculates the solid mass flowrate. A maximum 1.5% variation in the weight system sensitivity factor was measured over a 20 month period.

2.2 S/GFTF ON-LINE IRRADIATED PARTICLE VELOCIMETER

As discussed in Sec. 2.1 the S/GFTF calibration measurements include the rate of weight loss of the feed hopper (solid feedrate) and the gas velocity. To calibrate a flowmeter that provides a separate measurement of the SVF and particle velocity, the particle velocity at the flow instrument location must be established. Knowing the particle velocity will not only verify the particle velocity measured by the capacitive flowmeter, but also with the solid feedrate will confirm the solid volume fraction measured by the capacitive flowmeter and densitometers (DM).

Local particle and velocity distribution measurements can be provided in principle by Laser Doppler anemometry (LDA)[2] provided that particles are of micron size and the SVF is less than 0.001. Likewise, isokinetic sampling devices fail for large particles and high SVF. Thus, none of the known tools of experimental two-phase fluid mechanics can be used for those SVF above 0.005 that are part of the specifications of nonintrusive flow

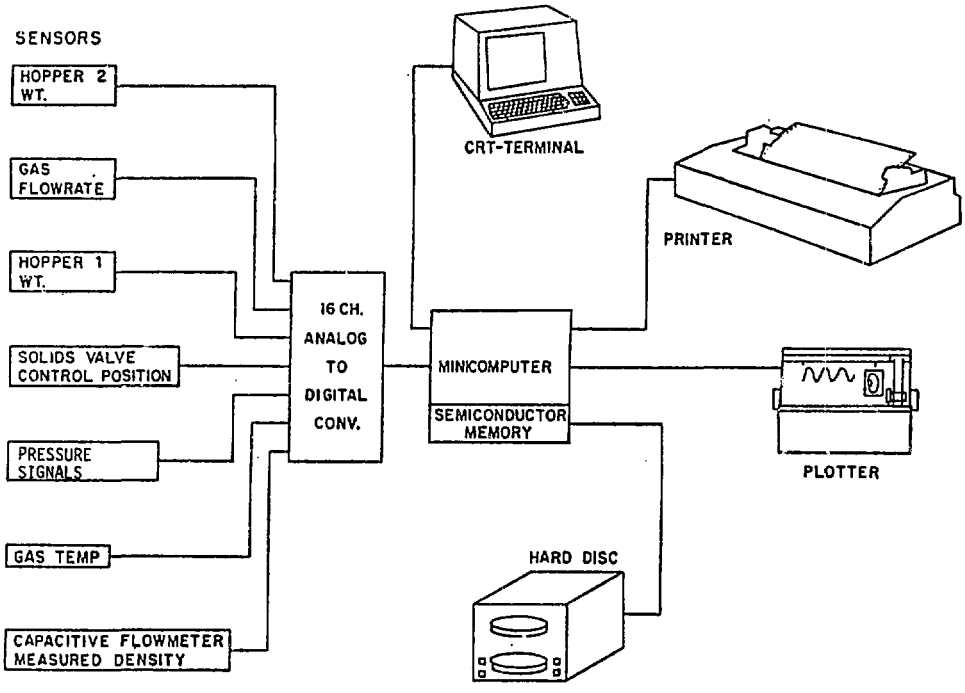

Fig. 2.1.4. S/GFTF Data Acquisition System

Table 2.1.1. Typical DAS Channel Allocation for the S/GFTF

Channel	Signal	Cable Number
1	Hopper 2 weight	
2	Orifice to gas bypass valve signal	
3	Hopper 1 weight	
4	Hopper 1 3 in. KV position	
5	0-12 ft. transducer 4, ± 1 psi	PT4
6	Gas temp cell 2/cell 3	
7	Capacitive flowmeter SVF	
8[a]	Orifice gauge pressure, 0-15 psi	
9	0-24 ft. transducer 5, ± 15 psi	PT2
10	Tee gauge pressure	PT3
11	Densitometer SVF	PT5
12	Capacitive flowmeter SVF	
13	0-40 ft. transducer 10; ± 15 psi	PT6
14[a]	Orifice ΔP; transducer 6; ± 1 psi	PT1
15	Upstream densitometer	
16	Hopper 1 pressure; transducer 3	

[a]Used to measure the gas flowrate.

instruments being developed at ANL for pneumatic conveyors.

The presence of the ATSR nuclear research reactor in the same building as the S/GFTF made available a very direct means of local particle velocity measurements averaged over the pipe cross section via a time-of-flight measurement of radioactive particles.[3,4] Sample particles to be activated were fabricated from resin, hardener, and indium oxide powder to duplicate closely the size and density of the glass beads used in the flow tests. The particles were rendered radioactive in the ATSR which resulted in a 54 min half-life of gamma activity. Twenty particles were injected into the flow stream during the reloading of the feed hopper as shown in Fig. 2.2.1 and in the process were randomly mixed with 409 kg (900 lb) of glass beads. The passage of each radioactive particle was registered by nine gamma detectors, encased in lead shields and sited along the horizontal test section, as a sudden increase in the count rate. A typical count rate is shown in Fig. 2.2.2 and was in the range of 2×10^5 to 10^4 cps. Since the radioactivity induced in these ANL-fabricated particles was of short duration, there was no need to retrieve them and access to the S/GFTF was available within 24 hr of the flow test without need for elaborate safety precautions. The glass beads and radioactive particles were recirculated back to the feed hopper 11 times during the single day of flow tests so that sufficient counts could be detected for a measurement.

Data acquisition was provided by combining the digital counts from all 9 NaI (Tl) scintillation detectors in an alternating set of scalers whose contents were temporarily stored in the PDP11/34 computer memory, and in real time were recorded as a 2-byte word on a digital tape recorder with 1024 count rate values in each tape record using the software program SCULER.[5] Each point of the typical record shown in Fig. 2.2.2 represents the counts accumulated over 1 ms. The 1024 ms record length was chosen to accommodate the maximum travel time of the particles from the solid/gas mixing tee to the last downstream detector. The first detector was connected separately to a digital count rate discriminator so as to record only when a radioactive particle entered the test section. Full details of this system will be presented in a forthcoming ANL technical memorandum.

Data analysis was performed after each flow test with the software program HSLISX,[5] and data processing consisted of computing the centroid of each peak and the channel number differences between all nine peaks produced by each particle passage. This resulted in 8 local particle velocity measurements. The records that occurred before and after steady flow, as well as a few overlapping records where two radioactive particles were within the test section simultaneously, were excluded. For each flow test this typically left, on the average, 15 particle velocity measurements at each of the 8 locations from which a good average particle velocity for each location was available. At the input and output ends of the CF and DM were gamma detector stations, as shown in Figs. 2.2.3 and 2.2.4.

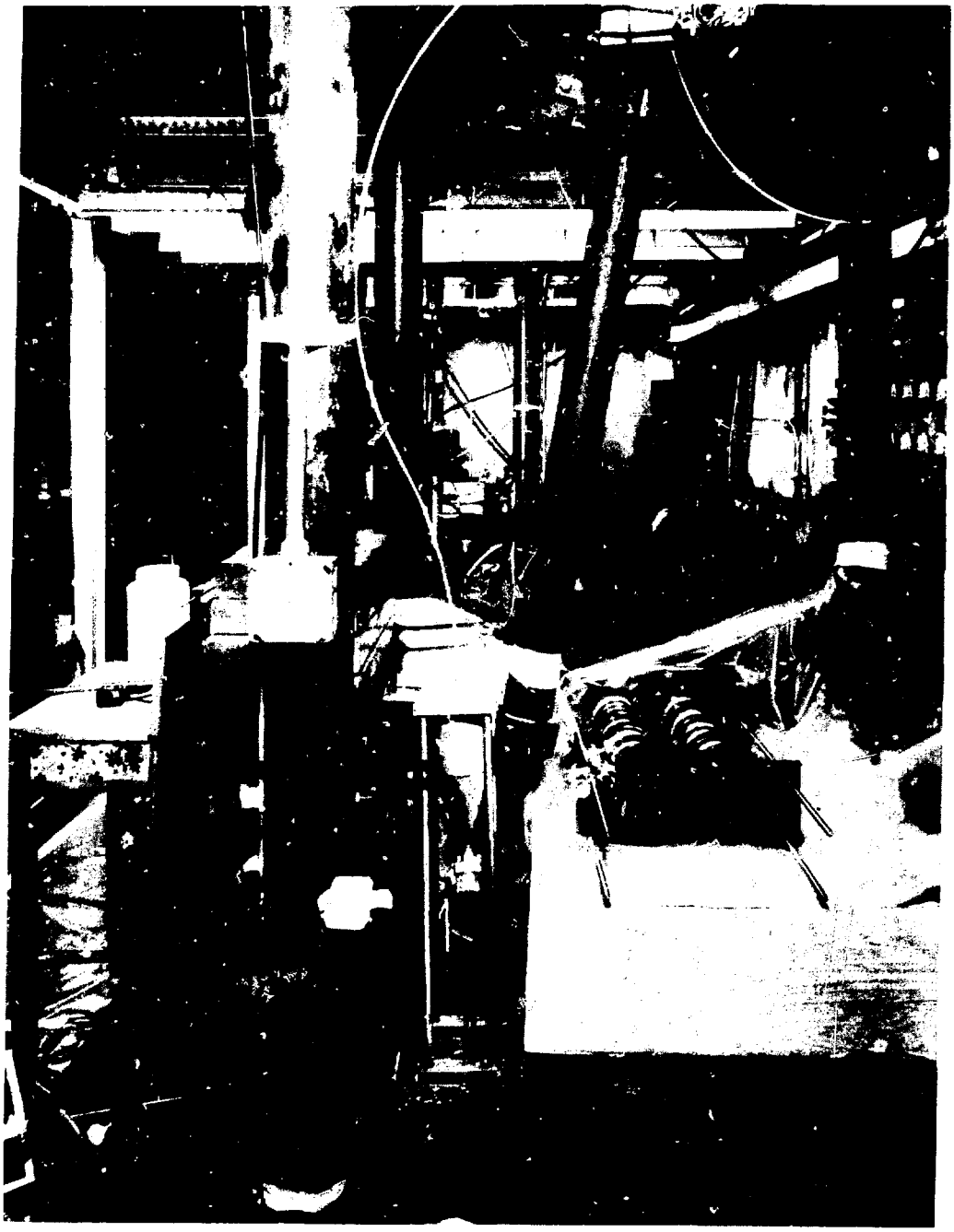

Fig. 2.2.1. S/GFTF Irradiated Particle Trickle Feeder

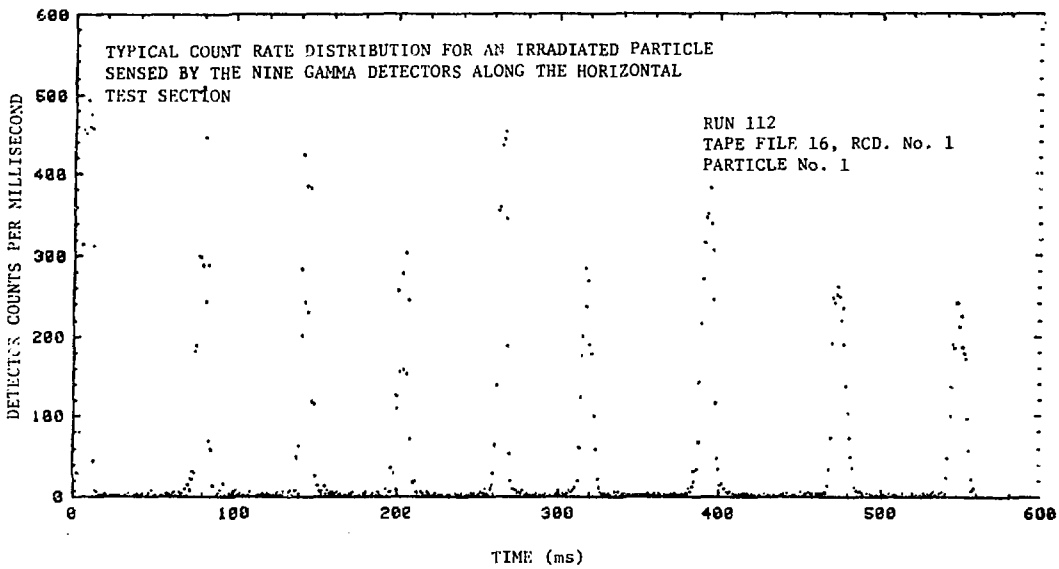

Fig. 2.2.2. Typical Irradiated Particle Count Rate Distribution

Fig. 2.2.3. Gamma Detectors at the Capacitive Flowmeter

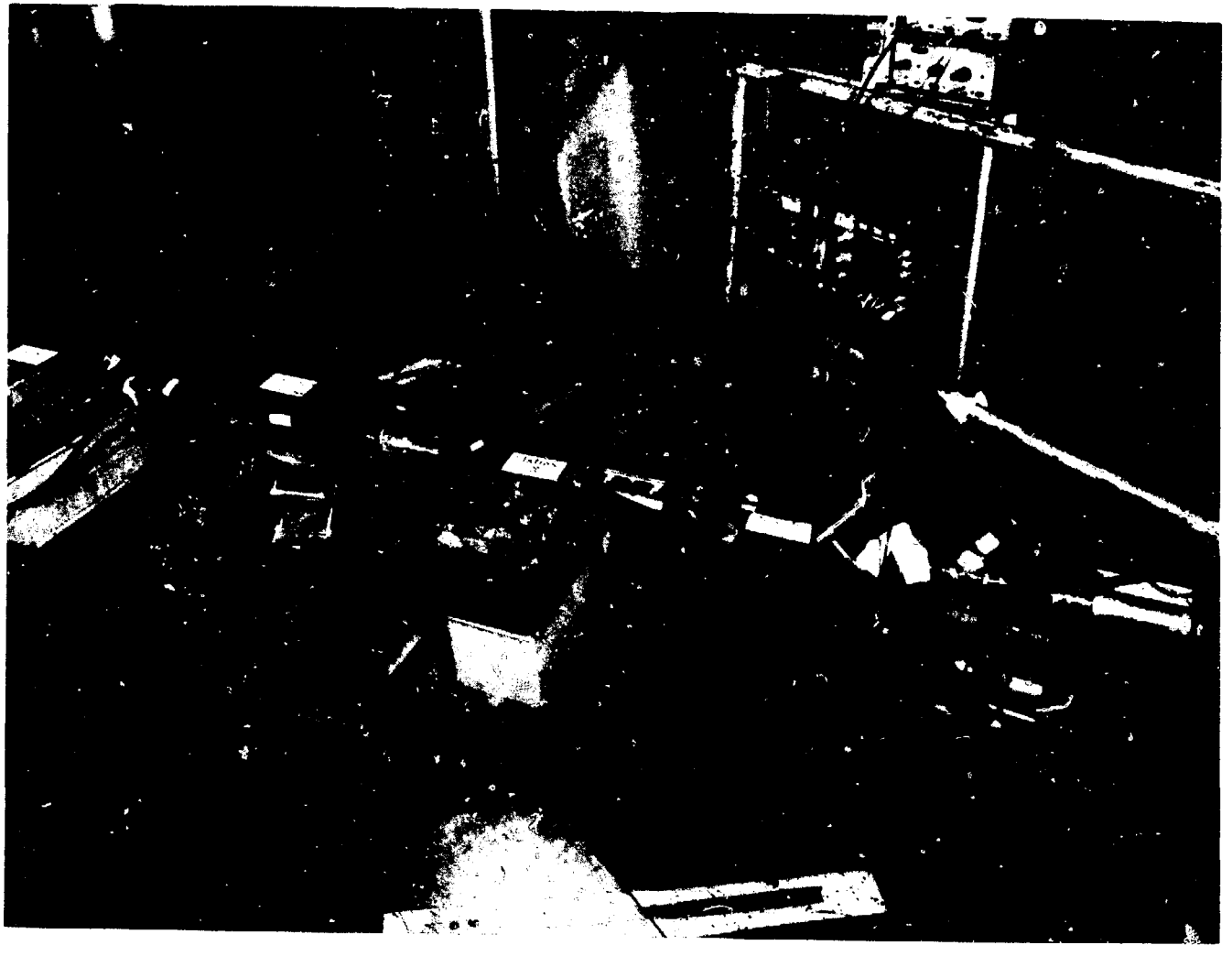

Fig. 2.2.4. Gamma Detectors at the Densitometer

The accuracy of the radioactive particle velocity measurement was within 1.5%. The detector separation was measured to 0.02%, the count rate peak locations were within 0.5% of reading, and the millisecond clock was stable to 1 ppm. The averaging of 15 particle velocity measurements reduced the typical velocity dispersion of 5.8% to 1.5%.

2.3 SUMMARY OF EXPERIMENTAL TESTS

The purpose of the tests was to evaluate the performance of several nonintrusive flowmeters for measuring solid feedrates in the range of 0.5 to 2 kg/s (1 to 4.4 lb/s) and SGL of up to 22 with an independent measure of the average particle velocity using radioactive particles. Two types of noninstrusive instruments using the capacitive principle to sense the solids were installed in the downstream section of the horizontal test section. The spoolpiece with the electrodes on the outside of the mullite liner is referred to as the CF since it measured the particle velocity and SVF. The second spoolpiece with the electrodes mounted on the inside duct surface is referred to as the DM since it measured the SVF.

The tests were performed with the CF and DM located 8.83 and 10.24 cm (28.97 and 33.6 ft) respectively from the solid/gas mixing tee. The orientation of the electrodes relative to the direction of solid/gas flow for these tests was with the plates vertical, which is shown in Appendix B to yield a small error for a vertical density gradient. Particle velocity measurements, using the cross correlation method, were made with the CF for electrode center-to-center separations of 4, 6, 8, 10, 12, and 18 cm (1.6, 2.4, 3.1, 3.9, 4.7, and 7.1 in.). The SVF and particle velocity measurements were made during time-of-flight measurements with the radioactive particles.

The local particle velocity was derived from the time-of-flight measurements obtained from the radioactive particle signal detected by nine gamma detectors situated along the horizontal test section. The installation locations of the detectors and the flow instruments are shown in Fig. 2.3.1. A gamma detector was situated at the input and output of the CF and DM. Five gamma detectors were located downstream of the mixing tee and upstream of the CF and DM to provide a complete independent measure of the particle velocity along the 12.3 m (40.4 ft.) horizontal test section. The relative locations of all devices are shown in Table 2.3.1.

The test series conditions and results are summarized in Table 2.3.2. This table is divided into Table A, B, C with the flow instrument measurements listed in Table A, and pressure measurements in Table B. The S/GFTF operating conditions and data acquisition file nomenclature are condensed in Table C. The first five columns of Table A and Table C summarize the test numbers, solid feedrates from the timed hopper weight measurement, solid to gas loadings, and the gas velocity as measured by a calibrated orifice meter. The solid feedrate mean and variation during the runs are shown in column 2. The average solid feedrate variation was 6%, indicating that the

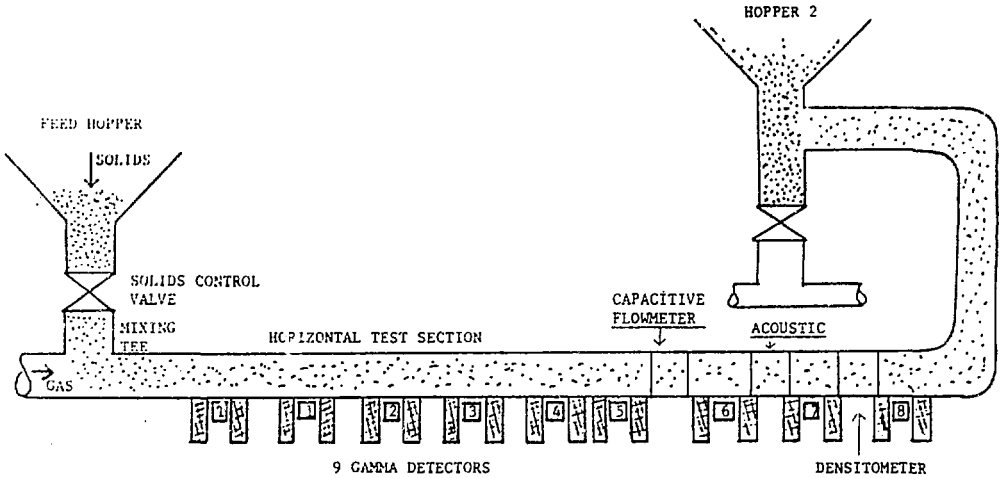

Fig. 2.3.1. Arrangement of Flow Instruments in Solid/Gas Test Section of the S/GFTF

Table 2.3.1. Test Section Locations of Flow Instruments and Gamma Detectors

Unit	Location cm (ft.)
Mixing tee	0
M.T. gauge pressure	3.8 (0.12)
Trigger detector	202.0 (6.63)
Detector 1	321.7 (10.55)
Diff. Pres. (a)	365.1 (11.98)
Detector 2	446.3 (14.64)
Detector 3	570.3 (18.71)
Detector 4	696.3 (22.84)
Diff. Pres. (a)	730.4 (23.96)
Detector 5	807.9 (26.51)
Capacitive flowmeter (center)	886.9 (29.10)
Detector 6	957.4 (31.41)
Acoustic flowmeter (center)	1024.0 (33.60)
Detector 7	1092.0 (35.83)
Densitometer (center)	1159.4 (38.02)
Diff. Pres. (a)	1216.7 (39.92)
Detector 8	1226.5 (40.24)

(a) with respect to Mixing Tee

Table 2.3.2. Summary of S/GFTF Flow Test Conditions and Measured Results Of All Test Instruments

Table A

Run	Solid Feedrate H_s(lb/s)	Solid/Gas Loading	Gas Velocity Orifice (9)	Gas Velocity CF(1) m/s	Capacitive Flowmeter (1,2) Cross Correlation Velocity (m/s)	Capacitive Flowmeter (1,2) Solid Vol. Fraction Signal (Volts)	Irradiated Particles Vel. (m/s) No.	Irradiated Particles Vel. (m/s) CF(1)	Irradiated Particles Vel. (m/s) AC(4)	Irradiated Particles Vel. (m/s) DM(3)	Densitometer Capacitance (pF) (2,3,6)	Solid Vol. (7) Fraction CF (1)(2)	Solid Vol. (7) Fraction DM(2)(3)
112	1.09 ± .06	6.5	25.8	28.3	21.9	0.189 ± .010	17	21.98	19.85	18.78	2.226	0.42	0.50
110	1.87 ± .15	10.2	25.9	30.0	23.4	0.258 ± .017	15	24.48	22.95	22.65	2.239	0.65	0.71
109	3.17 ± .19	16.6	24.6	30.3	24.3	0.445 ± .016	13	25.09	23.96	23.80	2.259	1.08	1.14
111	4.39 ± .42	22.0	23.5	29.6	23.6	0.663 ± .025	13	24.01	23.68	23.98	2.289	1.56	1.57
114	2.65 ± .15	10.8	30.7	38.1	30.7	0.300 ± .027	15	30.41	28.69	28.17	2.242	0.75	0.80
113	3.75 ± .17	14.6	29.3	38.1	30.3	0.425 ± .020	17	30.56	28.96	28.98	2.258	1.05	1.11

Table B

Run	Orifice P_g (9)	Pressure (PSI) (8) Mixing Tee P_g (10)	7.30 m ΔP (10)	9.67 m ΔP (10)	12.17 m ΔP (10)	Temp (°C) (9)
112	2.3	1.91	0.94		1.33	19.3
110	3.8	3.11	1.60		2.18	19.1
109	5.6	4.79	2.58		3.38	19.2
111	7.3	6.48	3.35		4.23	19.6
114	6.2	5.22	2.80	3.1		19.0
113	8.0	6.91	3.82	4.19		19.6

Table C

Run	Solid Feedrate H_s(lb/s)	Solid/Gas Loading	Gas Velocity Orifice (9)	Gas Velocity CF(1) m/s	S/GFTF Controls G.V (Volts)	S/GFTF Controls 3" KV (Volts)	S/GFTF Controls Hi Pres. (PSIG)	Anal. Tape No.	Anal. Tape Ind	Anal. Tape Footage	Tape File No.	Disc File Sec. Name (5)
112	1.09 ± .06	6.5	25.8	28.3	1.77	0.65	2.0	11	24-75	2724-3360	16	.230
110	1.87 ± .15	10.2	25.9	30.0	1.80	0.82	5.0	11	26-74	1797-2161	14	.130
109	3.17 ± .19	16.6	24.6	30.3	1.79	1.29	5.0	11	39-71	1363-1622	13	.100
111	4.39 ± .42	22.0	23.5	29.6	1.79	1.83	5.0	11	45-68	2413-2573	15	.200
114	2.65 ± .15	10.8	30.7	38.1	2.00	1.25	5.0	12	32-67	551-918	18	.315
113	3.75 ± .17	14.6	29.3	38.1	2.00	1.55	5.0	12	40-66	138-338	17	.300

(1) Capacitive Flowmeter; electrodes located 8.83 m from mixing tee.

(2) Horizontal Test Section with vertical orientation of electrodes.

(3) Densitometer; electrodes located 11.59 m from mixing tee.

(4) Acoustic; flowmeter located 10.24 m from mixing tee.

(5) Primary name 012585.

(6) Free Air Capacitance = 2.203 pF.

(7) $SVF = H_s/V_p \rho_s A$; $\rho_s = 2.459$ m/cm^3 for glass beads, $A = 21.65$ cm^2 for 2-in. Sch. 40 pipe

$SVF (\%) = 8.54\ H_s\ (lb/m)/V_p\ (m/s)$.

(8) $P_{atm} = 14.29$ psi.

(9) Gas Flow Stream.

(10) Solid/Gas Flow Stream; Distance from Mixing Tee.

S/GFTF system ran very steadily during the tests. Both hopper weighing systems were loaded with eight 50 kg (110 lb) weights and calibrated before and after the flow tests and agreements between these two measurements was within 1%.

The CF-measured particle velocity and SVF are summarized in Table A, columns 6 and 7. During these tests the nonintrusive acoustic flowmeter (AC) was installed between the CF and DM. The irradiated particle velocity measured at the CF, AC, and DM is shown in columns 9, 10, and 11. This velocity is the mean of the irradiated particle velocities measured during the period when the solid feedrate was steady and the number of velocities used in the calculation is shown in column 8. Comparisons between the CF measured particle velocity and the average irradiated particle velocity are discussed further in Sec. 4.2.

From the respective mean irradiated particle velocity and solid feedrate the SVF at the CF and DM is derived, details of which are discussed in Sec. 4.1. This derived SVF is shown in the last two columns of Table A and discussed in Sec. 4.1 and Appendix A. The DM measured capacitance with the solid/gas flow stream is also shown in Table A, column 12.

The solids used in this experimental study of the CF and DM on S/GFTF were 1000μ glass beads (Sinclair Abrasive and Equipment ~$2/lb) with an average density of 2.46 g/cm^3 and a dielectric constant in the range of 7 to 7.6. Typical physical and chemical properties supplied by the manufacture are presented in Table 2.3.3. A sieve analysis of the glass beads is given in Table 2.3.4 for grab samples obtained after a number of feed hopper unloadings. The average glass bead diameter remained essentially constant during the tests and was 1064 ± 21μ for 119 unloadings.

Table 2.3.3. Typical Physical and Chemical Properties of the Glass Beads Used in the S/GFTF Solid/Gas Flow Tests

Dielectric constant at 1 MHz, 20°C	7.00 - 7.6
Volume resistivity at 250°C (ohms)	$10^{6.5}$ - $10^{7.0}$
Specific gravity	2.46 - 2.49
Expansion coefficient (0-300°C) per °C	85 x 10^{-7}
Average diameter, μm	1045
Chemical element	wt - %
SiO_2	72.5
Na_2O	13.7
CaO	9.7
MgO	3.3
Al_2O_3	0.4
FeO and Fe_2	0.2
K_2O	0.1

Table 2.3.4. Sieve Analysis of Glass Beads Used in the S/GFTF Solid/Gas Flow Tests

U.S. Mesh Number	Sieve Aperture Microns (mils)	Glass % by Weight After H1 Unloadings[1] Virgin	8	23	39	80	119
18	1000 (39.4)	55.2	64.9	68.4	60.1	59.6	54.0
25	710 (27.8)	44.8	35.1	31.6	37.5	40.4	41.8
Avg. diam (microns)		1045	1082	1090	1042	1061	1023

[1] Hopper 1

3. CAPACITIVE INSTRUMENTS

3.1 DESIGN BASIS

Capacitive sensors are particularly useful for in-situ measurements of the flow of gases or liquids with solids since they are nonintrusive, have no moving parts, are economical, and can provide a real-time readout of the SVF and particle velocity. A typical application requires a reading of the capacitance of the device in the presence of the two-phase medium and a reference reading of the device with gas or liquid. With a calibration plot that covers the expected two-phase compositions and the temperatures and pressures at the measurement site, the SVF can be extracted from a combination of the sensor signals.

The accuracy, dynamic range, and time response of the reading depends on the electrode geometry, flow profile, electrical characteristics of the fluid, electric field distribution in the flow stream, and the signal conditioning electronics. A nonuniform dispersion of the solid which one would find in pneumatic conveyors also affects the readout, as discussed in Appendix B; it is shown that the effect is small. Alternatively, some specific schemes discussed in Appendix B, have been claimed to provide a reduction of the readout error for a nonuniform solid distribution within the duct.

A variety of capacitance meter electrode geometries have been described in the literature. The annular capacitor[6,7] shown in Fig. 3.1.1 evidently senses outside the duct and features a non-uniform field. The classical wrapped electrode device, shown in Fig. 3.1.2, also senses outside the duct, yet features a relatively homogeneous field within the duct except at the electrode edge. A narrow strip version of this device,[8-12] ANL-I, was the first unit developed at ANL and, while closely approximating a parallel plate geometry as shown in Fig. 3.1.3, senses the centerflow more strongly and has a small value of capacitance. To maintain a uniform electric field, five parallel electrodes are placed between the drive and pickup electrodes. The electrode voltages are derived from a resistance divider that

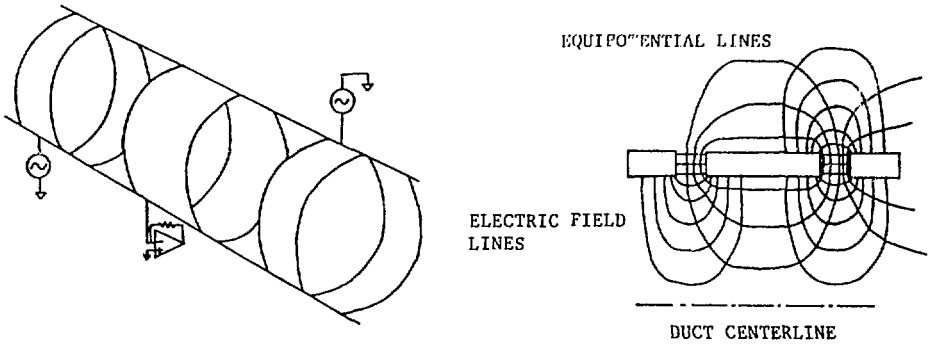

Fig. 3.1.1. Annular Electrode Capacitor

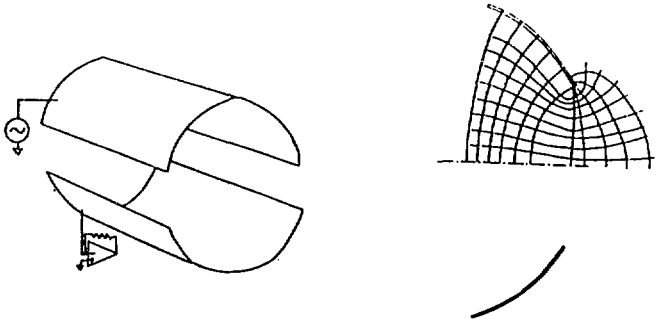

Fig. 3.1.2. Wrapped Electrode Capacitor

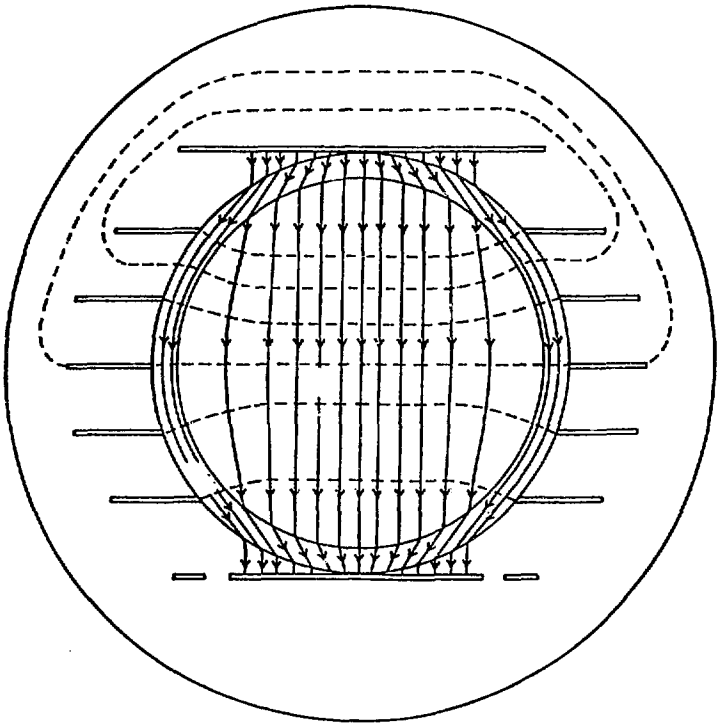

Fig. 3.1.3. Narrow Electrode Capacitor, ANL-I Version

equally divides the drive voltage. Internal and overall views of the ANL-I device are shown in Figs. 3.1.4 and 3.1.5, respectively.

The devices shown in Figs. 3.1.1 to 3.1.3 are typical of the better solutions that have been published or incorporated into commercial densitometers intended for duct installation. Measurements in a hopper are readily feasible with a rectangular cross section. Though this scheme is simple and highly effective, it would represent a line impedance and encounter erosion problems in a pneumatic conveyor.

In 1982 a second design, ANL-II, was developed at ANL. This design, an improved wrapped-electrode configuration, is shown in Fig. 3.1.6. The device capacitance has been enhanced by a factor of 4 and the coverage of the duct cross section has been increased to 85%. A guard electrode was incorporated to eliminate the inhomogeneous field at the plate edges. Details of this spoolpiece are described in Sec. 3.1.1.

The capacitive instrument described and evaluated in this report makes use of capacitive sensors whose design to a major extent relies on fluid dynamics as well as dielectric theory, which pointed to a minimum-error geometry. A full discussion of the design rationale will be provided in an

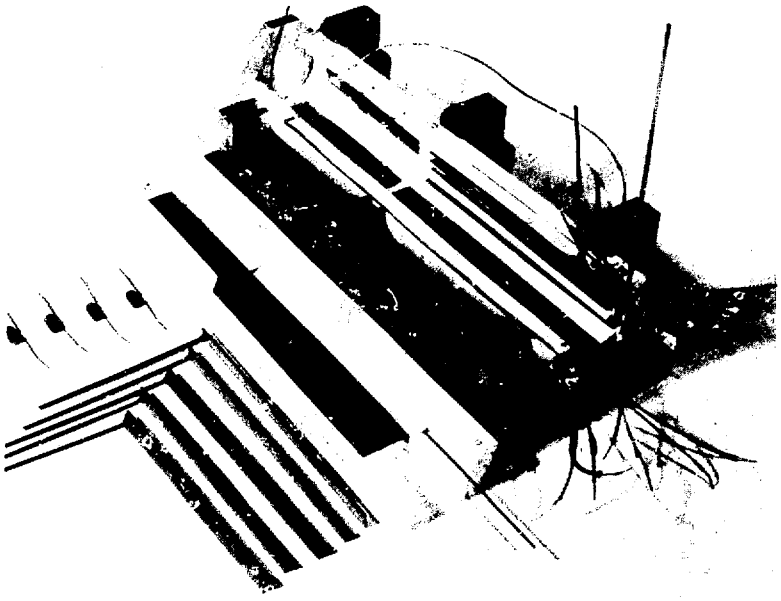

Fig. 3.1.4. Overall Interior View of Capacitive Flowmeter, ANL-I Version

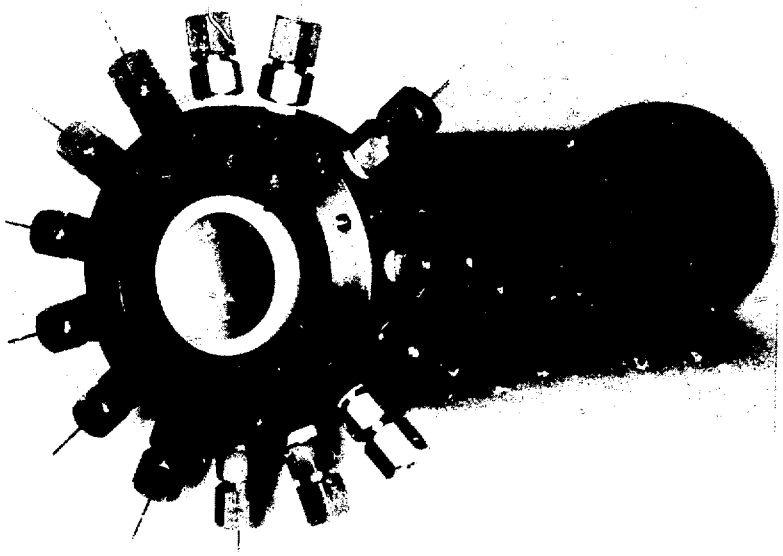

Fig. 3.1.5. Capacitive Flowmeter Spoolpiece, ANL-I Version

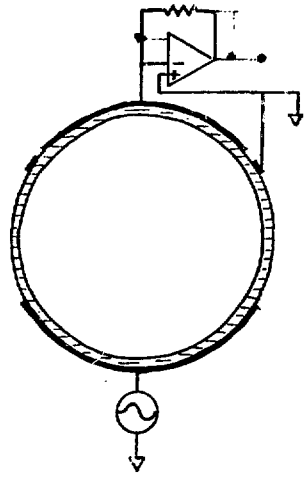

Fig. 3.1.6. Increased Wrapped Electrode Capacitor, ANL-II Version, With Guard Equipped Signal Electrode

accompanying report, now in preparation.[13] For the present report, which emphasizes experimental details and results, only an outline of the design basis is needed. It will be the aim of this outline to indicate, with no more than the necessary minimum of equations, the relationships between the mass flowrate and the duct-averaged solid component velocity and SVF, and then to consider how separate measurements of each of these variables can best be made with minimum error.

To begin this outline of the design basis the local duct-average particle velocity is defined as

$$v_p(z, t) = \frac{\iint v_p(z, r, \theta, t)\, \phi(z, r, \theta, t)\, r dr d\theta}{\iint \phi(z, r, \theta, t)\, r dr d\theta} \tag{3.1.1}$$

where

$v_p(z, r, \theta, t)$ = local particle velocity, and

$\phi(z, r, \theta, t)$ = local SVF.

For particles of diameter d_p, the SVF is

$$\phi = \frac{\pi d_p^3 n(z, r, \theta, t)}{6} \tag{3.1.2}$$

where

n = local particle number density.

The denominator of Eq. 3.1.1 is the averaged SVF multiplied by the duct cross section area A_p:

$$\phi(z, t) = \frac{\iint \phi(z, r, \theta, t)\, r dr d\theta}{A_p} \tag{3.1.3}$$

The solid component mass flowrate thus can be defined as

$$M_s(t) = A_p\, \rho_s\, \phi\,(z, t)\, v_p\,(z, t) \tag{3.1.4}$$

where

ρ_s = intrinsic density of the particle, and

$\phi\, \rho_s$ = bulk density.

Equation 3.1.4 defines the needed relation between the solid component flowrate, and the bulk density and velocity of the solid component. In particular, it suggests that an accurate measurement requires that both devices or schemes establish the same reference point z along the duct: as shown by Eq. 3.1.4, ϕ_s and v_p individually vary with z, even though their product remains constant.

The ANL-II CF is based on such a dual measurement by means of electrodes whose location averages each measurement to the same point as described in Sec. 4. The following discussion, which is provided in more detail in Ref. 13, indicates how each measurement can be made without error. The method essentially involves an unbiased sampling of the whole duct by the sensing device.

The first measurement to be discussed is the cross-correlation measurement of the particle velocity defined by Eq. 3.1.1. The cross-correlation is based on repeated sampling of the sensor readout from an upstream and a downstream sensor separated by a distance d_e. The double arrays of samples

Su_i and Sd_i yields the cross-correlation function (CCF):

$$CCF = \frac{1}{N} \sum_{i=1}^{N} Su_{i+k} \, Sd_i \qquad (3.1.5)$$

where

Su_i = ith sample of the upstream electrode
Sd_i = ith sample of the downstream electrode, and

$k = 1, 2, \ldots M.$

M typically amounts to 50-150 for a CCF that covers the peak, whereas $N = 10^3 - 10^4$ samples are needed to reduce statistics. Since the samples are consecutive in time and are obtained at a real-time sampling rate f_s such that the elapsed time t_{ij} between samples Su_i and Su_j amounts to $t_{ij} = (j - i)/f_s$, the CCF point k represents an offset time $t_k = k/f_s$.

If some local inhomogeneity in the flowing medium causes a signal excursion in both electrodes, then the samples Su_i and Sd_j will feature correlated excursions at the offset $t_{ij} = t_k$, in addition to random (channel noise) excursions that are uncorrelated. Thus a sufficiently large number of correlated excursions within the span of N samples or time span N/f_s will result in a peak in the CCF at the offset t_p. If all local inhomogeneities travel down the duct at the same speed v, it follows that

$$v = d_e/t_p = d_e f_s/k_p. \qquad (3.1.6)$$

However, in turbulent flow, individual particles and local clusters or voids move at local velocities $v(r,\theta)$, each resulting in a different transit time t_p; the location of the CCF peak thus appears to average the transit time rather than the velocity. A number of reports[12,14,15] on CCF velocity measurements in turbulent flow show that the velocity computed by Eq. 3.1.6 tends to be proportional to the true medium flow speed but differs from it by a "meter factor" of up to 30%.

The root cause of such readout errors differs for laminar and turbulent flows. For the former case, of no interest here, the argument made with respect to transit time vs velocity averaging is pertinent and leads to a sensor geometry design that can minimize, though not eliminate, this error, as discussed in an accompanying report. For turbulent flow, rapid mixing invalidates the argument as individual clusters spread out radially and thus end to average over the weak radial velocity distribution that characterizes this flow regime.

To show this, the equivalence of local clustering and artificial tagging of a flowing stream is introduced. Either "tag" is dispersed through turbulent diffusion hence, the Taylor/Aris equation,[16,17,18]

$$C(z, t) = C(0, 0)\left(2\pi H_s t\right)^{-1/2} \exp - \frac{\left(t-Z/\bar{v}\right)^2}{2H_s t} \tag{3.1.7}$$

may be used. This equation describes the duct-averaged tag concentration $C(z, t)$ at z and t as a function of a dispersion parameter H_s, the duct-averaged velocity $\bar{v}$, and the injected tag concentration $C(0, 0)$ at the time $t = 0$ and $z = 0$. The peaking time difference for two tag-sensing stations at Z and at $Z + d_e$ is obtained by differentiating Eq. 3.1.7:

$$t_u = \left(\frac{Z^2}{\bar{v}^2} + \frac{H_s^2}{4}\right)^{1/2} - \frac{H_s}{2}, \tag{3.1.8}$$

$$t_d = \left[\frac{(Z + d_e)^2}{\bar{v}^2} + \frac{H_s^2}{4}\right]^{1/2} - \frac{H_s}{2}. \tag{3.1.9}$$

Expanding the root,

$$t_d - t_u = \left(\frac{d_e}{\bar{v}}\right) \left[1 - \frac{H_s^2\, \bar{v}^2}{8Z(Z + d_e)} \cdots\right]. \tag{3.1.10}$$

For fully turbulent flow, it is found[19] that the peak width $2.36\ (H_s Z/\bar{v})^{1/2}$ is about 40% of the transit time $Z/\bar{v}$; hence, the term in brackets is equal to 3.6×10^{-3} and can be neglected. It follows that for fully developed turbulent flow, the duct-averaged velocity $\bar{v}$ is accurately found by Eq. 3.1.6, provided only that the CCF peak corresponds to the tag distribution function peak given by Eq. 3.1.7 and the entire flow is sensed, without bias.

The kind of tag that is represented by a solid cluster or void differs from one that is injected into a liquid stream, in that clusters or voids tend to be flanked upstream and downstream by concentrations of opposite sign. As a consequence, the CCF peak is inevitably flanked by anti-correlation and correlation secondary peaks; signal filtering can add further secondary structures. This is indicated in Figs. 4.2.1 and 4.2.4, which present typical measurements in which Eqs. 3.1.5 and 3.1.7 are effectively convoluted. This convolution, however, affects only the detailed shape but not the peak location; hence, the requirement that the CCF peak correspond to the peak of Eq. 3.1.7 is satisfied (this would not be the case for laminar flows typical for slurries).

The practical conclusion for the design of a turbulent-flow CCF velocity sensor is that a geometry that can sample the entire duct cross section without significant bias should also yield a duct-averaged solids velocity through Eq. 3.1.6, from the location of the CCF peak offset, without a "meter factor."

Regarding the design of the bulk density sensor, four topics are addressed below:

(a) The relation between sensed capacity and electrode geometry,
(b) The connection between sensed capacity and duct-averaged SVF,
(c) The possible effect of nonuniform solids distribution on the sensed capacity, and
(d) The equation that yields the SVF in terms of the channel voltage readout.

To develop the first topic, we consider a generalized capacitor geometry as shown in Fig. 3.1.7 where the capacity C_M is composed of contributions from elementary capacitors ΔC_M,

$$\Delta C_M = \frac{K_o K_m \Delta A}{\Delta s} . \qquad (3.1.11)$$

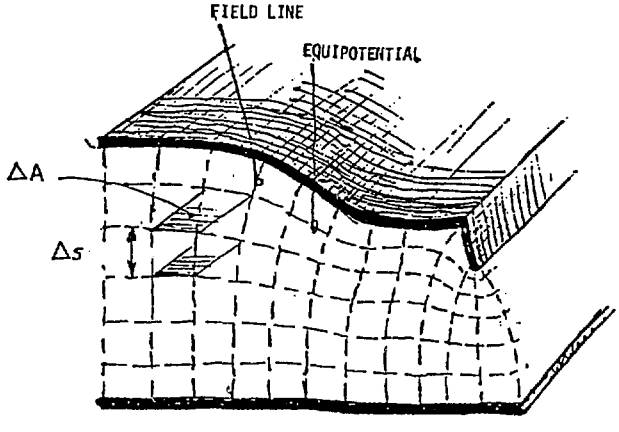

Fig. 3.1.7. Generalized Capacitor Geometry Showing Effect of Electrode Curvature

The plates of area ΔA lie along equipotentials while the plate separation

$$\Delta s = \frac{\Delta V}{E} \tag{3.1.12}$$

is expressed in terms of the local field E and a uniform potential step ΔV. Equations 3.1.11 and 3.1.12 illustrate the equivalence of the terms "capacitive" and "electromagnetic field" sensing. Within regions spanned by plates that are relatively flat, equipotentials are evenly divided and the field is uniform, while in the immediate vicinity of a sharp edge in an electrode, the field drops as 1/r, where r = distance from the edge. The elementary capacitors are combined by integrating first along field lines and then over the plate area:

$$C_M = K_o \int dA \left[\int ds/K_m(s)\right]^{-1} \tag{3.1.13}$$

where $K_m(s)$ a local medium dielectric constant is related (as discussed below) to the SVF. Equation 3.1.13 can be integrated only for simple geometries, but suggests, in conjunction with Eqs. 3.1.11 and 3.1.12, that uniform sensing of a medium enclosed by capacitor plates requires the avoidance of edge fields and, likewise, the exclusion of regions outside the duct. The equation further suggests the desirability of a geometry that maximizes the overall capacity C_M, thus enhancing sensitivity to small changes in the medium dielectric constant K_m.

All of these desired performance characteristics are readily obtained by using a rectangular or annular duct section for the measurement. Transition pieces at either end that connect to a duct of circular cross section can be readily designed as to keep the cross-sectional area constant. Design studies indicate that such devices could be built to withstand the expected erosion. An annular geometry offers an especially favorable overall capacity and should permit the flow to be sensed with an almost perfectly uniform sensitivity, thus causing the flowmeter to be of exceptional accuracy. The two chief problems inherent in this design, a considerable initial cost and the introduction of an unavoidable impedance in the gas-entrained solid flow, suggest an alternate, duct-conforming geometry, at least for initial testing.

A number of duct-conforming capacitive sensors have been described in the literature.[6,7,14] However, none of these comes close to meeting the three requirements of uniform sensing. Concentric ring electrodes, depicted in Fig. 3.1.1, are particularly inappropriate; a strongly inhomogeneous field reaches outside the duct, while the overall capacity is modest. A wrapped-plate arrangement, shown in Fig. 3.1.2, is somewhat better but still features an edge-field whose relative intensity varies with the area

covered. A version of that geometry that reduces the signal electrodes to a strip, introduces an inner liner, and tries to homogenize the field within the duct by making electrodes flat instead of surface-confirming is shown in Fig. 3.1.3. The signal electrode at the bottom is equipped with lateral grounded guard strips.

This geometry was used in a series of tests,[8,9,11] but proved to have some problems, because it emphasized center flow (which resulted in a strong velocity error, as discussed above) and had a small overall capacity, 0.5 pF. As indicated in Fig. 3.1.3, the geometry still sensed regions outside the medium, within the wedge-shaped spaces between the liner and plate, within the liner itself, and between the signal electrode and the nearest voltage divider plate.

In 1982, as these problems became apparent, it was realized that a modification of the conventional wrapped-plate design could eliminate outside sensing as well as the edge-field problem. A grounded guard strip flanking the signal electrode(s) was arranged so as to sense most of the duct with a reasonably uniform electric field, spanning an angle of about 120°. This is shown in Fig. 3.2.3, which may be compared with Figs. 3.1.2 and 3.1.3. As compared with the unmodified wrapped-plate scheme, the edge field, increasing by a factor of 5-10 compared to the field at the center of the plates, has been shunted off on the guard electrode. Figure 3.2.3 indicates a possible increase of the plate area by a factor of about 4. This geometry was, therefore, further developed into the spoolpiece described in Sec. 3.2.1.

Concerning the second topic, the relation between the SVF and the duct capacity, there exists a long-standing but unresolved problem: the bulk properties of mixtures of substances, each of which has well-defined individual properties, cannot be expressed by an accurate formula, whether the property in question is the dielectric constant, the conductivity, or the magnetic susceptibility. However, for the case of a very dilute distribution of one substance within another, asymptotic expressions, accurate to the first order in the SVF of the dilute constituent and fairly accurate to the second order, can be found. To put the SVF measurement in perspective, consider the elementary model representing slabs of dielectric interleaved with spaces that contain the fluid (gas or liquid). Slabs can be set normal or parallel to the plates that produce a uniform field and thus form a set of parallel or series-connected capacitors. The details of the following derivations are shown in Appendix A.

For the parallel connection (slabs normal to the plates) the total capacitance, C_M with solid and fluid is

$$C_M = [K_s\phi + K_f\ (1 - \phi)]A/D \qquad (3.1.14)$$

where

ϕ = solid volume fraction,
K_s = solid dielectric constant,
K_f = gas or liquid dielectric constant,
D = plate separation, and
A = plate area.

The relative change in capacitance, $\frac{C_M - C_F}{C_F}$, where C_F is the capacitance with no solids is

$$\frac{C_M - C_F}{C_F} = \left(\frac{K_s - K_f}{K_f}\right) \phi \tag{3.1.15}$$

For the series connection (slabs parallel to the plates), the total capacitance, C_M with solid and fluid, is

$$C_M = \frac{K_s K_f A}{[K_f \phi + K_s(1 - \phi)]D} \tag{3.1.16}$$

The relative change is capacitance is

$$\frac{C_M - C_F}{C_F} = \frac{(K_s - K_f)\phi}{K_f \phi + K_s(1 - \phi)} \tag{3.1.17}$$

The Maxwell-Rayleigh[36] formula for uniform dispersion of solids in the fluid and small SVF expresses the relative change of capacitance as

$$\frac{C_M - C_F}{C_F} = \frac{(K_s - K_f)\phi}{K_f + \frac{(K_s - K_f)(1 - \phi)}{3}} \tag{3.1.18}$$

Introducing the useful parameters

$$G = \frac{C_M - C_F}{C_F} \tag{3.1.19}$$

$$g = \frac{K_s}{K_f} - 1 \tag{3.1.20}$$

these three models reduce to

$G = g\phi$ for dielectric slabs normal to plate, to (3.1.21)

$$G = \frac{g\phi}{1 + g\,(1 - \phi)}$$ for dielectric slabs parallel to plates, and to (3.1.22)

$$G = \frac{g\phi}{1 + \frac{g}{3}\,(1 - \phi)}$$ which is the Maxwell-Rayleigh model for small amounts of solid uniformly dispersed in the gas. (3.1.23)

These results assume a uniform electric field within the entire duct. The effect of a nonuniform solid distribution on the sensed capacity is discussed in Appendix B, where it is shown that the type of nonuniformity found in pneumatic conveyors has a small effect on the readout. However, the readout error becomes large if phase separation is allowed to develop as may be the case in horizontal ducts. For higher concentrations Eq. 3.1.23 is not valid. Thus, it is unclear whether a significant improvement can be achieved by the "averaging" schemes that have been advocated and incorporated into capacity sensing devices.[20-22]

To determine the SVF from the capacitance readings requires a calibration curve as was done in the flow tests with the irradiated particle velocimeter. A calibration curve must be provided over the entire range of concentrations at the temperatures and pressures that prevail at the site. In general, as was shown with the three models and above with other models discussed in Appendix A, the calibration curve will be linear for SVF <0.05 which is typical of pneumatic conveyors. Also, as represented in the models, the SVF can be inferred from the measured relative change in capacitance if the dielectric constants of the solid and gas are known.

As the last topic, some remarks may be added concerning an electronics scheme suitable for long-term unattended operation in an industrial plant. For the velocity measurement, a scheme based on the buckout channel described in Sec. 3.2.1 should be suitable since the location of the CCF peak is not sensitive to small drifts in gain, phase, or oscillator amplitude. However, the capacitive flow instrument will need a readout as given by Eq. 3.1.23, and further needs the highest degree of stability that can be devised in order to keep the fractional statistical error as low as possible. A suitable scheme can be provided at modest cost by switching the entire channel back and forth between the duct capacitor and a dummy capacitor exactly equal to the empty-duct capacity C_F. Direct rectification, amplification, and digitization through a voltage-to-frequency converter (VFC) delivers a pulse train to a scaler that is read out and reset at an interval of the order of 1 sec. For such an interval, a suitably designed VFC can deliver 10^6 counts, thus obtaining a digital precision that is far beyond the capability of other types of digitizers. Successive intervals thus produce a pair of digital numbers, one proportional to C_M and the other to C_F. A single-chip computer then does a double-precision digital division, subtracts 1 from the quotient, and multiplies the result

by $\frac{3+g}{3g}$, the scaling constant, thus obtaining the SVF.

This simple scheme eliminates all errors due to channel gain, driving amplitude, oscillator frequency and phase, or VFC conversion-constant drift, and largely eliminates errors resulting from channel nonlinearity. Design considerations that must be addressed include construction of the dummy capacitor and elimination of offsets throughout the channel. Pending availability of funds, a prototype of this significantly improve electronic channel will be designed and tested in the future.

3.2 CAPACITIVE FLOWMETER

3.2.1 Description

The CF used in the solid/gas tests is shown in Fig. 3.2.1 and consists of two separate capacitive measurement units: one for SVF and the other for particle velocity. In the design of this improved version of the first-generation unit (ANL-I) tested at Hygas[8] and the S/GFTF,[9-11] attention was given to maximizing the signal-to-noise ratio since the change in capacitance signals is inevitably weak in a solid/gas flow stream. An electrode geometry was chosen to maximize the coverage of the duct interior while minimizing the readout error due to a nonuniform electric field. A close-up view of the spoolpiece's electrodes based on these considerations is shown in Fig. 3.2.2. Two electrodes are used to measure the SVF and are on the sides of the velocity measuring electrodes so as to average the SVF over the measuring region. The SVF electrode capacitance is 2.210 pF. Four velocity measuring electrodes were incorporated and provide a range of electrode separations for examining its effect on the quality of the cross-correlation function. The velocity electrode capacitance is ~0.2 pF. These measuring electrodes, as shown in Fig. 3.2.2, are economical copper sheet cutouts with a pressure-sensitive adhesive back that were easily fastened to a 91.5 cm (36.0 in.) long, 5.4 cm (2.1 in.) I.D. ceramic tube. The splicing of the drive electrode as well as the attachment of signal connections was provided by soft-soldering. Figure 3.2.3 shows the layout of the SVF and velocity sensing electrodes, drawn to scale and unrolled from the duct surface. Table 3.2.1 summarizes the characteristics and functions of each electrode, and Table 3.2.2 summarizes the physical properties of the ceramic liner. To minimize the effects of external fields, the spoolpiece was encased in a 78.7 x 12.7 x 15.2 cm (31 x 5 x 6 in.) steel enclosure with quick disconnect connectors for each electrode. This external electrode scheme is immune to erosion, and it is shown in Appendix D that the mullite liner has a negligible effect on the CF measurement of the SVF. Drawbacks may be the possible difficulty in matching the pipe dimensions exactly, as well as the possibility of generating a certain amount of electrostatic charge.

3.2.2 Capacitive Flowmeter Signal Conditioning Instrumentation

A schematic diagram of the entire chain of instrumentation for

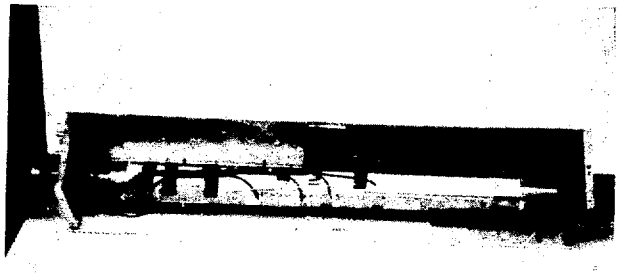

Fig. 3.2.1. Overall Interior View of Capacitive Flowmeter, ANL-II Version

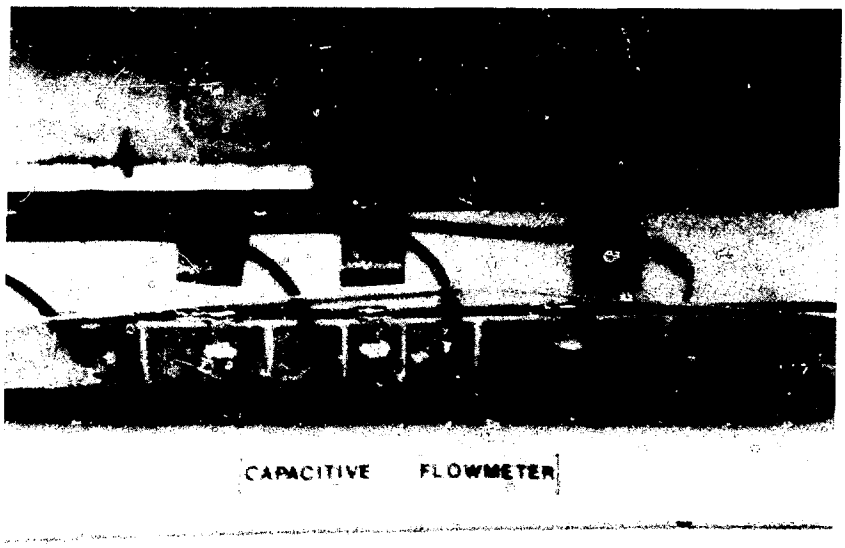

Fig. 3.2.2. Close-up View of Capacitive Flowmeter Electrodes and Guard

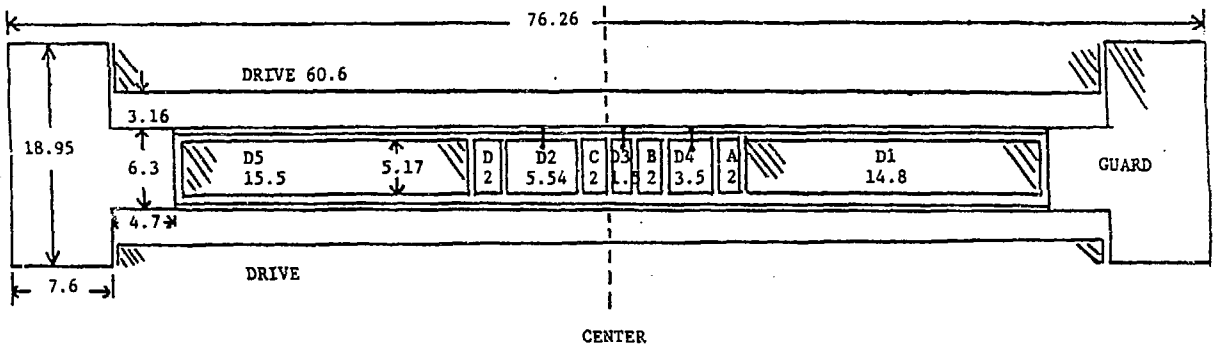

Notes:

1. All dimensions in cm
2. Electrode gap 0.23 cm
3. Guard strip width 0.34 cm
4. Unrolled view
5. ~4:1 scale
6. All electrodes are 0.036 mm copper foil

Fig. 3.2.3. Capacitive Flowmeter Electrode Configuration for Electrodes on the Outside Surface of the Ceramic Tube

Table 3.2.1. Characteristics of Capacitive Flowmeter Electrodes

Electrode	Length cm (in.)	Width cm (in.)	Angle	Measured Capacitance (pF)
Drive	60.6 (23.9)	6.32 (2.5)	120°	
Solid Vol. Frac.	15.5 (6.1)	5.17 (2.0)	98.2°	2.21
	14.8 (5.8)	5.17	98.2°	
Velocity				
D	2.0 (0.8)	5.17	98.2°	0.32
C	2.0	5.17	98.2°	0.15
B	2.0	5.17	98.2°	0.14
A	2.0	5.17	98.2°	0.21
Guard strips (2)	51.7 (20.4 in.)	0.34 (0.1 in.)	6.5°	

Velocity Electrode Pairs

Designation	Separation cm (in.)
CB	4 (1.57)
BA	6 (2.36)
DC	8 (3.15)
CA	10 (3.94)
DB	12 (4.72)
DA	18 (7.09)

Ceramic Liner

Length - cm	91.5 (36.02 in.)
ID - cm	5.4 (2.12 in.)
OD - cm	6.0 (2.36 in.)
Wall thickness (cm)	0.3 (0.12 in.)

Table 3.2.2. Typical Physical Properties[1] of the Mullite Liner Used for the Capacitive Flowmeter

ID	5.4 cm
OD	6.0 cm
Wall Thickness	0.3 cm
Length	91.5 cm
Coefficient of Linear Thermal Expansion (25 - 200°C), $\frac{\Delta L}{L}$	3.7×10^{-6}/°C
Specific Gravity	2.82
Flexural Strength 25°C	27K PSI
1000°C	22K PSI
Tensile Strength 25°C	18K PSI
Dielectric Constant	6.2[2]

[1] All property values are from the Coors Porcelain Company
[2] ANL measurement

processing the SVF and particle velocity signals from the CF is shown in Fig. 3.2.4. An amplitude and frequency-stable 100 kHz sinewave oscillator are applied to the drive electrode, and each sensing electrode is connected to a current-to-voltage (I/V) converter preamplifier as shown in Fig. 3.2.5. The gain for all I/V converters is identical and their time delay differences are insignificant. The output voltage, V_o, of the I/V converter is given by

$$V_o = V_{osc} 2\pi f \, C_F Z \tag{3.2.1}$$

where

V_{osc} = amplitude of the oscillator signal,
f = oscillator frequency (Hz),
C_F = capacitance of CF electrode pair, and
Z = impedance at oscillator frequency of feedback network 150 kΩ in parallel with 5 pF.

At 100 kHz, Z = 135.7 kΩ and for C_F = 1 pF, the I/V converter output is given by

$$V_o = 0.85 \, V_{osc} \tag{3.2.2}$$

and the CF output current, I, is

$$I = 6.3 \times 10^{-7} \, V_{osc}. \tag{3.2.3}$$

For these flow tests, the oscillator amplitude was 1.6 Vrms. The CF output current levels wandered around 1 μA and were easily measured at the chosen oscillator frequency. The main criterion for selecting the oscillator frequency was to make the reactive component of current to be larger than the resistive component, as determined by the resistance across the duct.

To enhance the sensitivity of the electrodes to SVF values in the range of 0.01, an out-of-phase buckout current scheme with amplitude and phase adjustments, as shown in Fig. 3.2.5, was introduced between the oscillator drive signal and the I/V converter input. A null signal was generated when solids were not present in the flow stream and was detected with the circuit shown in Fig. 3.2.5. Measured variations of the CF current sensing preamplifier gain were less than 0.1% during a gas only flow stream.

The preamplifier outputs were amplitude-demodulated and amplified,

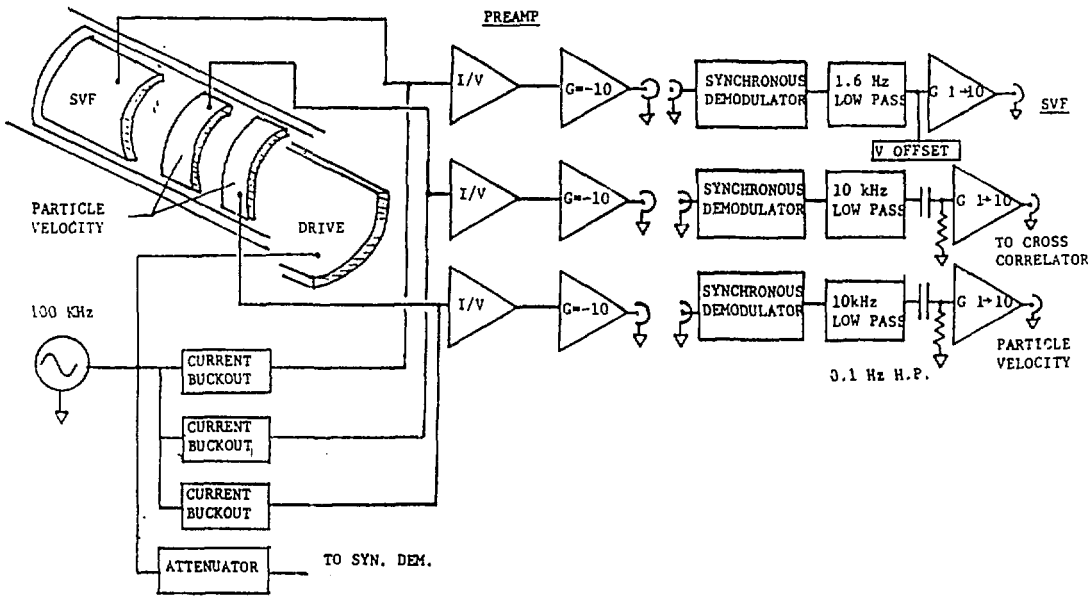

Fig. 3.2.4. Capacitive Flowmeter Current-Sensing Electronics for Measuring Solid Volume Fraction and Particle Velocity

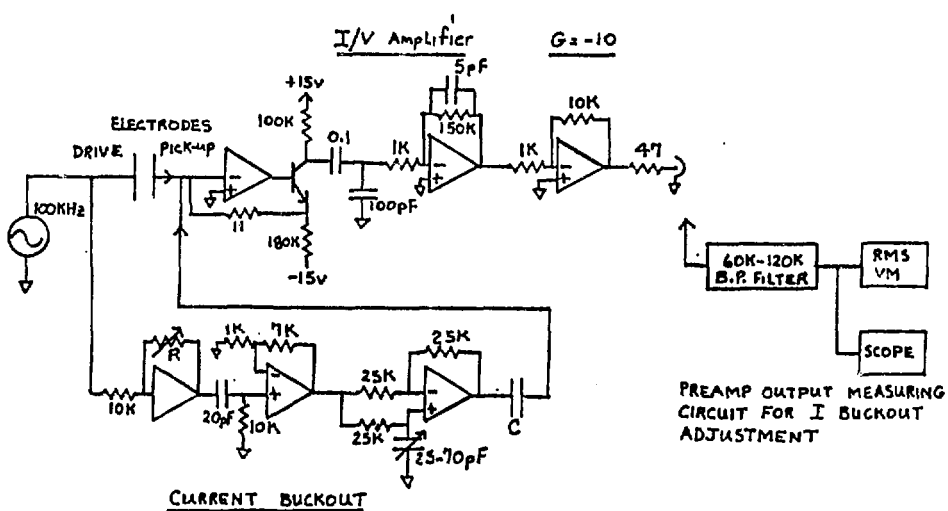

Fig. 3.2.5. Capacitive Flowmeter Current-Sensing Preamplifier

as shown in Fig. 3.2.6. The modulated signals from all electrodes were transmitted to their respective AD 630 synchronous demodulators whose carrier inputs were optimized with a phase trim network. The 100 kHz signal applied to the drive electrode was attenuated and then fed to the phase trim network. As indicated, the cross-correlation particle velocity analog channels differ from the SVF channel only in the output filtering stage. The SVF demodulated signal was DC coupled to a 0.1 s first-order low-pass filter and amplified with an offset voltage signal which allows preselection of a specific frequency component in the sensed-medium SVF fluctuation. This SVF signal conditioning scheme was convenient for testing purposes and while it does not allow full exploitation of Eq. 3.1.23, it produced a channel output that was proportional to the relative change in capacitance, as shown by Eq. 3.2.1.

The particle velocity demodulated signals were filtered with a 10 kHz two-pole low-pass active filter and AC coupled (0.1 Hz) to a variable gain DC amplifier before being processed on the SD 360 digital signal processor. This amplitude-modulated consequence experienced by the CF with a solid/gas flow is discussed in Appendix E.

3.2.3 Data Analysis and Reduction Techniques

A block diagram of the instrumentation for performing time and frequency domain analysis on the particle velocity and SVF signals is shown in Fig. 3.2.7. The instrumentation included on-line monitoring, magnetic tape recording, and real-time analysis of all signals. For on-line monitoring the SVF signal was monitored with the S/GFTF DAS and the time domain characteristics of conditioned signals were monitored with a multichannel oscilloscope and a two channel digital signal processor (DSP) with associated scope display (Spectral Dynamics Model SD 360). All CF signals were recorded at 15 ips in an FM mode on the Ampex PR 2230 IRIG standard instrumentation recorder. A typical tape recorder channel allocation is shown in Table 3.2.3. All recordings were preceded by a 1 Vrms, a 1 kHz and a 10 kHz calibration signal on all channels. This enabled the record and reproduce amplifiers of the tape recorder to be adjusted for a gain of 1 and allowed the bandwidth to be measured for the recorder amplifiers.

Dual-channel cross-correlation also was performed on the DSP with a 10 kHz analysis range and 256 linear averages for the pair of particle velocity electrodes. Each cross-correlation was computed with 1024 sampled data values. Table 3.2.4 summarizes typical operating conditions for the DSP during these flow tests. With the four velocity electrodes, A, B, C, and D (Fig. 3.2.3), cross-correlations were obtained for six electrode separations. With the DSP 10 kHz analysis range, a ±25 ms time with a 0.05 ms resolution correlogram was measured leading to a measurement precision of ~1%. For improved resolution for higher particle velocities and more closely spaced electrodes, a 40 kHz analysis range was used with an effective 0.01 ms resolution.

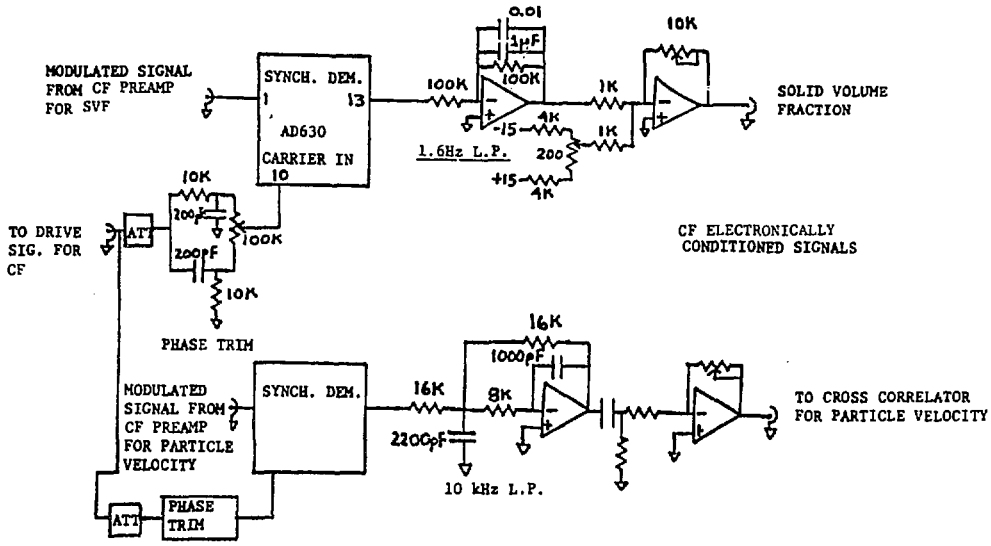

Fig. 3.2.6. Amplitude Demodulator for Capacitive Flowmeter Signals

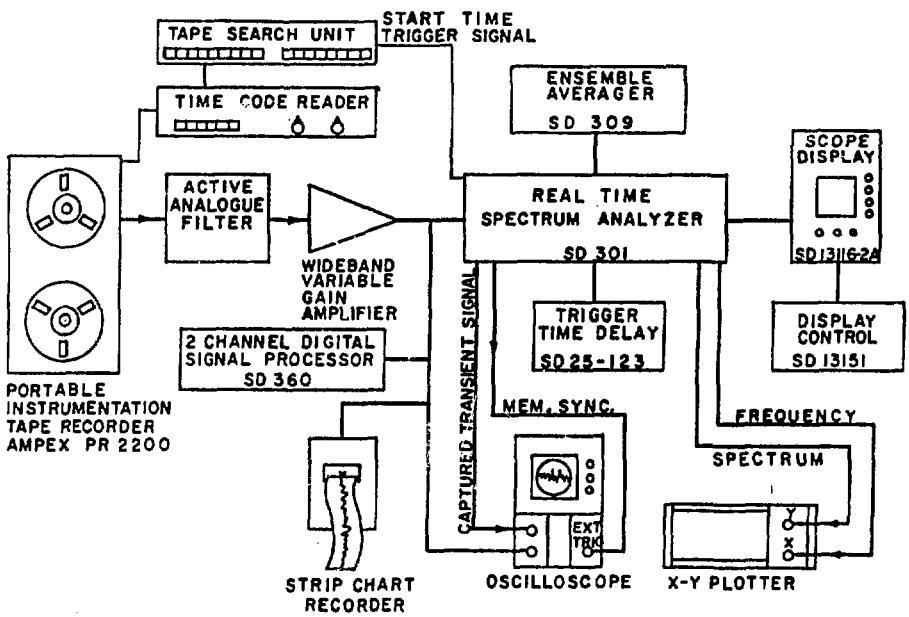

Fig. 3.2.7. S/GFTF Data Analysis System for Flow Instrumentation

Table 3.2.3. Typical Analog Magnetic Tape[1] Recorder Channel Allocation

Channel	Mode	Allocation	Cable Number
1	FM	CF D Electrode, ΔC	11
2	FM	CF D Electrode, ΔQ	7
3	FM	CF C Electrode, ΔC	12
4	FM	CF C Electrode, ΔQ	8
5	FM	CF B Electrode, ΔC	13
6	FM	Acoustic Cross-correlation Flowmeter	
7	FM	CF A Electorde, ΔC	14
8	FM	Acoustic Cross-correlation Flowmeter	
9	FM	CF D1, D5 Electrode, ΔC	PT5
10-14		Not Used	
A[2]		Voice Log	

[1]Tape speed 15 ips, 0-10 kHz bandwidth

[2]Edge track

Table 3.2.4. Typical Setup Conditions for the Digital Signal Processor

Processor	SD36D
Input Attenuation	10 dB
Analysis Range	10 kHz
Time Resolution	0.05 ms
Average Mode	Linear
Number of Averages	256
Cross-correlation Processing Time	~16s
Cross-correlation Time Scale	±25 ms
Number of Samples	1024

3.3 DENSITOMETER

3.3.1 Description

The second flow instrument using the capacitive principle to measure the SVF was the DM as shown in Fig. 3.3.1. To minimize particle-impact charging and possible significant readout errors due to the liner, the spoolpiece was designed with the electrodes on the inside surface. The CF-wrapped electrode scheme was used for both electrodes to allow maximum duct coverage, and long electrodes furnished a large device capacitance of 2.20 pF. Table 3.3.1 summarizes the characteristics of each electrode. The electrodes were produced by milling from 5.2 cm (2-in.) schedule 40 pipe. During fabrication the electrodes were held in place on the surface of a teflon-faced mandrel whose diameter exactly matched the pipe ID of the test section and wrapped with resin-impregnated glass tape. The insulating spaces between the electrodes were filled with alumina-loaded resin.* The assembly mandrel used a piece of 5.08 cm OD (2.00-in.) highly polished brass tubing. After allowing the resin to set, the brass tubing was slipped out and the teflon sheet then peeled off, making the inner surface of the DM smooth. Mechanical integrity was enhanced by external wrapping with resin-impregnated tape. Signal connections to the electrodes pass through the glass tapewrap and coaxial cables connected to them pass through the outer box to the instrumentation.

The DM did not show any visible signs of erosion in over 100 runs. However, these runs represent only 8 hr of solid/gas flow and thus do not constitute a realistic test for an industrial application.

For future flow tests it is planned to use the DM to predict the particle velocity. Three DMs will be installed in the horizontal test section and, after a series of flow tests with irradiated particles, the DM capacitance reading could be empirically related to the in-situ SVF. During flow tests without the irradiated particle velocimeter the particle velocity at various test section locations could be determined from the measured solid feedrate and the DM of measurements the SVF.

3.3.2 Densitometer Signal Conditioning Instrumentation

The electronic measuring circuit for the DM, as shown in Fig. 3.3.2, directly measures the capacitance with and without solids. The SVF, as discussed in Sec. 3.1.1 and Appendix A, can be inferred from these measurements. An automatic capacitance bridge (Hewlett Packard Model HP4270A) with a four digit readout of the measured capacitance was used and could be operated at frequencies of 1, 10, 100 and 1000 kHz with a response time of 70 ms to 5 s. It has a measuring range from 1 pF to 1.2 μF in 6 ranges. The SVF test data reported for the DM were collected at 100 kHz and the measuring rate was 0.5 s. The digital output used a BCD format and was converted to an analog signal for the S/GFTF DAS. To enhance the sensi-

*Biggs, Inc.

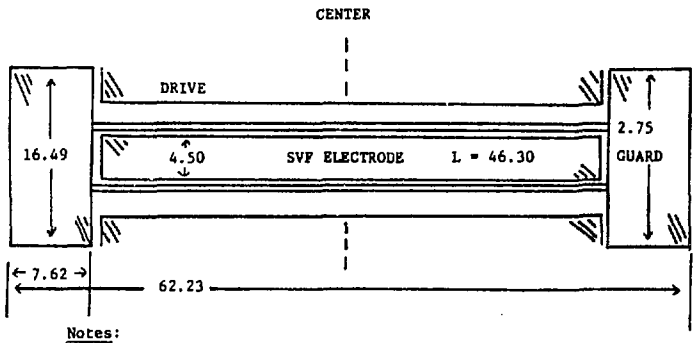

Notes:
1. All dimensions in cm
2. Electrode gap 0.23 cm
3. Guard strip width 0.34 cm
4. Unrolled view
5. ~4:1 scale

Fig. 3.3.1. Densitometer Electrode Configurations

Table 3.3.1. Characteristics of Densitometer Electrodes

Electrode	Length cm(in.)	Width cm(in.)	Angle	Measured Capacitance (pF)
Drive	46.3(18.2)	5.5(2.16)	120°	
Solid Volume Fraction	46.3(18.2)	4.5(1.77)	98.2°	2.203
Guard Strips	47.0(18.5)	0.48(0.19)	6.5°	

Overall Length - 62.23 (24.5)
ID - 5.25 (2.067)
OD - 6.03 (2.375)

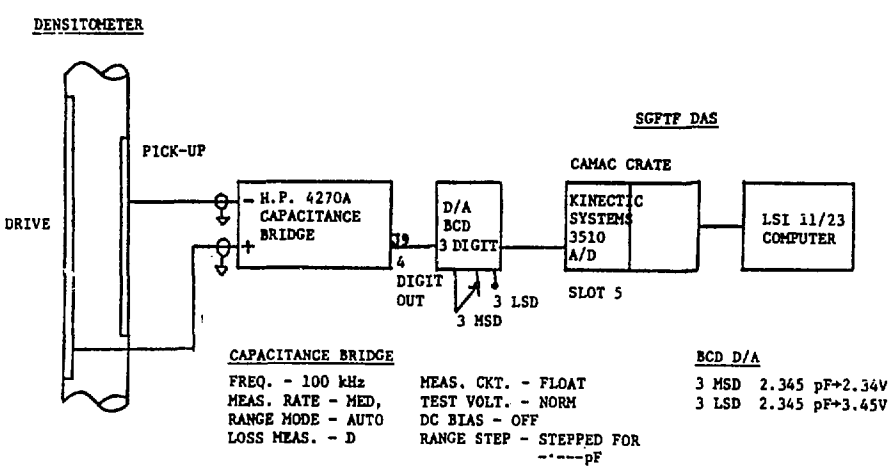

Fig. 3.3.2. Capacitive Measuring Circuit for the Densitometer

tivity of the capacitance reading by the DAS the three least significant digits of the capacitance were converted to an analog voltage such that a 0.001 pF capacitance change developed a 10 mV step. The most significant digit of capacitance, as anticipated, remained constant during the solid/gas flow tests.

4. EXPERIMENTAL RESULTS

4.1 SOLID VOLUME FRACTION

The SVF was measured with the CF and DM for the range of solid concentrations ranging from 0 to 1.6 vol%. Measurements are planned for higher concentrations. As mentioned earlier, the electrodes for the CF were on the outside surface of the liner, while the DM electrodes were on the inside duct surface. For the CF, the SVF electrode signals were demodulated and low-pass filtered with the resulting voltage signal being related to the actual SVF. The readout quantity for the DM was the actual capacitance which was related to the actual SVF and compared with the models discussed in Sec. 3.1 and Appendix A. The actual SVF at the location of each capacitive instrument was inferred from the solid feedrate and the average of 15 particle velocity measurements with the irradiated particle velocimeter at each location. The SVF was determined using

$$M_s = \rho_s \, \phi \, A_p \, v_p \tag{4.1.1}$$

where:

M_s = solid feedrate,

ρ_s = solid density,

ϕ = solid volume fraction,

A_p = pipe cross-sectional area, and

v_p = particle velocity

The SVF, expressed as a percentage, is given by

$$\phi = \frac{8.54 \, M_s}{v_p} \tag{4.1.2}$$

where

A_p = 21.65 cm^2 (3.36 $in.^2$) for 2-in. schedule 40 pipe,

ρ_s = 2.46 g/cm^3 for the glass beads,

M_s is in lb/s, and

v_p is in m/s.

The uncertainty in the DM capacitance measurement arises from the variances of individual measurements using Eq. 4.1.3[23]

$$\sigma_G^2 = \sigma_M^2 \left(\frac{\partial G}{\partial C_M}\right)^2 + \sigma_F^2 \left(\frac{\partial G}{\partial C_F}\right)^2 \tag{4.1.3}$$

where

$G = \frac{C_M}{C_F} - 1$,

C_M = DM capacitance with solid and gas,

C_F = DM capacitance with gas,

σ_{CM}^2 = Variance of C_M,

σ_F^2 = Variance of C_F, and

σ_G^2 = Variance of the relative change in DM capacitance.

Solution of Eq. 4.1.3 yields

$$\sigma_G^2 = \left(\frac{\sigma_{CM}}{C_F}\right)^2 + \left(\sigma_F \frac{C_M}{C_F^2}\right)^2. \tag{4.1.4}$$

The variance attached to the capacitance measurement can be estimated from the uncertainty of 0.001 pF and the measured capacitance of the order of 2 pF. This yields the propagated uncertainty in G of 0.0007 when the actual measured value of G is in the range of 0.02 to 0.08.

A similar statistical analysis for the SVF computed from Eq. 4.1.2 yields

$$\left(\frac{\sigma_\phi}{\phi}\right)^2 = \left(\frac{\sigma_M}{M_s}\right)^2 + \left(\frac{\sigma_v}{v_p}\right)^2 \tag{4.1.5}$$

where

σ_ϕ^2 = variance of ϕ,

σ_M^2 = variance of M_s, and

σ_v = variance of v_p.

The measured standard deviations for M_s and v_p and the final computed standard deviation for the SVF are tabulated in Table 4.1.1. The computed fractional error in SVF is nominally 2%.

4.1.1 Capacitive Flowmeter

The mass flow measurements of the CF are separated into SVF and particle velocity. The SVF measurements for solid concentrations ranging from 0 to 1.6 vol% are shown in Fig. 4.1.1. A linear relationship of

$$\text{VOLTS} = -0.004 + 0.418\phi \ (\%) \qquad (4.1.6)$$

where ϕ is SVF in %,

was measured between the CF electrode signal, conditioned with the amplitude demodulator (VOLTS), and the actual SVF measured by the methods described in Sec. 4.1. This measured CF relationship shows an appreciable sensitive response of 0.418 v for 1% SVF increments and extrapolates to 0.0V when the SVF is zero. Table 4.1.2 summarizes the SVF data measured with the CF; the lowest SVF measured with solids was 0.65%. For each SVF measurement the CF signal deviation was ~5%.

Table 4.1.1. Statistical Errors for the Solid Volume Fraction Measurement

Run	M_s (lb/s)	σ_M	V_p (m/s)	σ_V	ϕ (%)	σ_ϕ	σ_ϕ/ϕ (%)
112	1.09	0.0085	21.98	0.3	0.42	0.007	1.7
110	1.87	0.02	24.48	0.4	0.65	0.013	2.0
109	3.17	0.03	25.09	0.5	1.08	0.024	2.2
111	4.39	0.081	24.01	0.5	1.56	0.043	2.8
114	2.65	0.024	30.41	0.4	0.75	0.012	1.6
113	3.75	0.031	30.56	0.3	1.05	0.013	1.3

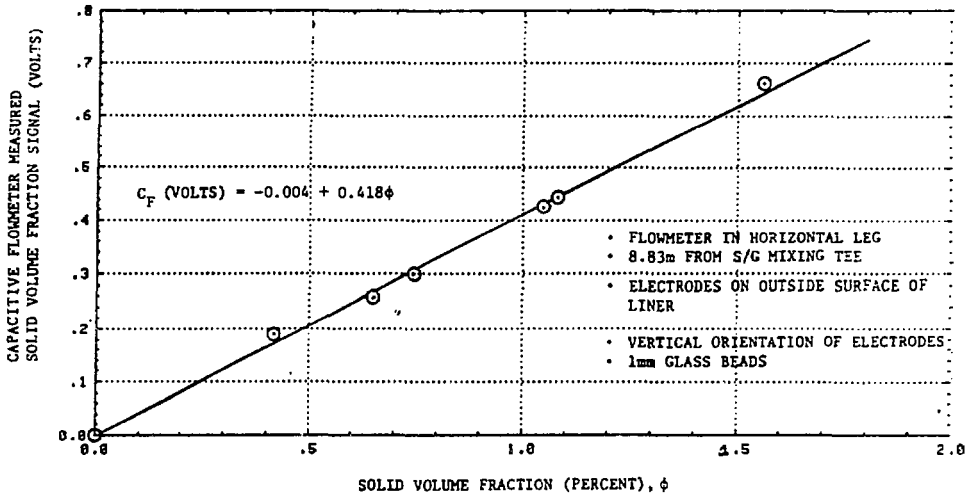

Fig. 4.1.1. Capacitive Flowmeter Solid Volume Fraction Signal for a Range of Solid Volume Fraction Values

Table 4.1.2 Capacitive Flowmeter Solid Volume Fraction Signal for a Range of Solid Volume Fraction Values

Run	Solid Feedrate M_s (lb/s)	Irradiated Particle Velocity at Capacitive Flowmeter m/s	Solid Volume Fraction (%)(2)	Capacitive Flowmeter SVF Signal (V)(1)
112	1.09	21.98	0.42	0.189 ± 0.01
110	1.87	24.48	0.65	0.258 ± 0.017
109	3.17	25.09	1.08	0.445 ± 0.016
111	4.39	24.01	1.56	0.663 ± 0.025
114	2.65	30.41	0.75	0.300 ± 0.027
113	3.75	30.56	1.05	0.425 ± 0.02

(1) CF SVF (V) = -0.004 + 0.418 ϕ with 0,0 data point, where ϕ = SVF(%)

(2) SVF = $M_s/v_p \rho_s A$, where:

M_s = Solid feedrate (lb/s),

ρ_s = glass bead density = 2.46 g/cm^3,

A = 21.65 cm^2 for 2-in. Sch. 40 pipe,

v_p = Irradiated particle velocity (m/s), and reduces to

$$SVF(\%) = 8.54 \frac{M_s}{v_p}$$

While the amplitude demodulator signal conditioning scheme provides a measure of the SVF, it is more appropriate, as was discussed with the models in Sec. 3.1.1, to infer the SVF from a direct capacitance reading. For these tests the single available capacitance bridge was used for the DM but, during a series of solid/gas flow tests in October 1984, the CF SVF response was measured with the capacitance bridge[24]. The results of these measurements showed a linear relationship between the actual capacitance of the SVF electrode and the SVF electrode signal, conditioned with the amplitude demodulator. With this calibration curve the actual capacitance could be inferred from the voltage signal and, in turn, the SVF from the actual capacitance. While this assumes knowing the proper capacitance vs the SVF model, the DM measurements (Sec. 4.1.2) shows this to be the case.

4.1.2 Densitometer

The SVF response of the DM was measured twice with the irradiated particle velocimeter. Each time, the DM was located at 11.6 m (38.0 ft) from the solid/gas mixing tee and linear relationships of

$$\left(\frac{C_M - C_F}{C_F}\right) 100 = 0.01 + 2.19\phi \qquad (4.1.7)$$

$$\left(\frac{C_M - C_F}{C_F}\right) 100 = 0.02 + 2.22\phi \qquad (4.1.8)$$

were obtained by fitting the measured points where C_M is the measured capacitance with solid and gas, C_F is the measured capacitance with gas respectively and ϕ is the SVF in percent. Equation 4.1.7 is for the solid/gas flow tests performed on November 19-21, 1984, for solid concentrations ranging from 0 to 1.3 Vol%, and Eq. 4.1.8 is for the tests with the solid concentrations ranging from 0 to 1.6 Vol% as shown in Fig. 4.1.2. These results establish the repeatability of the DM SVF measurement and its capability to independently measure the solid concentration from which the average particle velocity can be determined if the solid feedrate is known. While this might suggest that the DM could be used in place of the irradiated particle velocimeter, the measured relative change in capacitance, as shown in these linear relationships, is small and nominally twice the SVF. The measured change in capacitance, as shown in Table 4.1.3 which summarizes the DM measured data, was 0.076 pF for the largest solid concentration of 1.6 Vol%. This fully extended the capacitance bridge measurement capability since its resolution was 0.001 pF. Likewise, the DM capacitance and measuring electronics for the condition of no solids must remain stable to 0.05% for a 5% accurate measure of a 0.05 SVF. Conversely, the measurement precision is enhanced for larger solid concentrations.

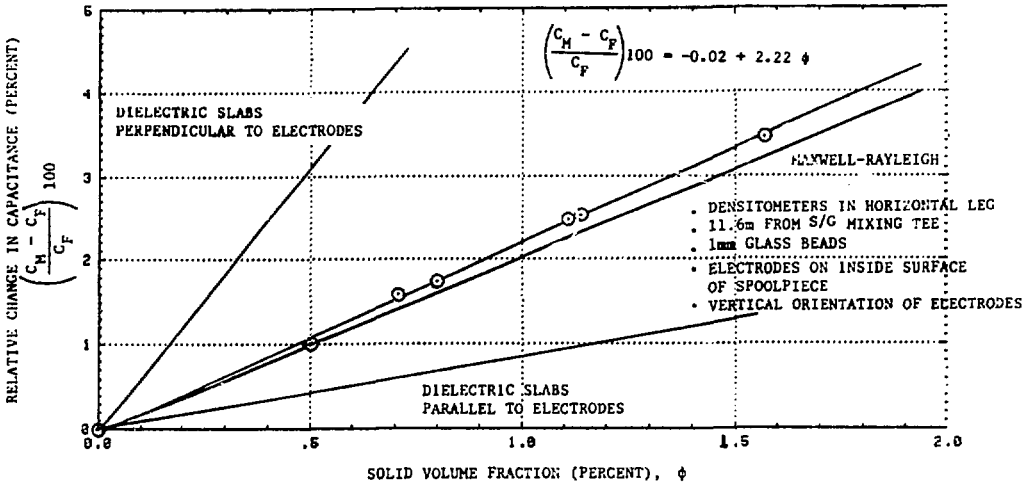

Fig. 4.1.2. Densitometer Capacitance of a Range of Solid Volume Fraction Values

Table 4.1.3. Densitometer Capacitance for a Range of Solid Volume Fraction Values

	Solid Feedrate (lb/s)	Particle Velocity(1) at Densitometer (m/s)	Solid Volume Fraction (%)	Relative Change(2) in Capacitance (%)
112	1.09	18.78	0.50	1.03
110	1.87	22.65	0.71	1.59
109	3.17	23.80	1.14	2.51
111	4.39	23.98	1.57	3.46
114	2.65	28.17	0.80	1.75
113	3.75	28.98	1.11	2.47

(1) Irradiated particle velocity.

(2) Equal to $\left(\frac{C_M - C_F}{C_F}\right) 100$, where

ϕ = SVF (%)

C_F = C (no solids) = 2.203 pF, and

C_M = capacitance with solids

$\left(\frac{C_M - C_F}{C_F}\right) 100 = 0.02 + 2.22\ \phi$ with 0,0 data point

$\left(\frac{C_M - C_F}{C_F}\right) (100) = 0.01 + 2.19\phi$ (Nov. 19, 21, 1984)

Figure 4.1.2, also shows the expected SVF responses for the three models described in Sec. 3.1 and Appendix A. The two elementary models for dielectric slabs normal and parallel to the electrodes significantly deviate from predicting the SVF with a capacitance reading for a distribution of solids in a solid/gas flow stream. The Maxwell-Rayleigh model for small concentrations of solids uniformly dispersed in the gas is in close agreement with the DM measured SVF. Assuming an average dielectric constant of 7.3 for the glass beads, as per Table 2.3.3, and 1.0 for the gas, the Maxwell-Rayleigh model described by Eq. 3.1.15 reduces to

$$\frac{C_M - C_F}{C_F} = \frac{6.3\ \phi}{1 + 2.1\ (1-\phi)} \tag{4.1.9}$$

which for $\phi \leq 0.02$ reduces to

$$\frac{C_M - C_F}{C_F} = 2.03\ \phi \tag{4.1.10}$$

with a 1.5% error.

For the solid concentrations ranging from 0 to 1.6 Vol% and the assumed solid dielectric constant the maximum deviation between the Maxwell-Rayleigh model and the DM SVF response is ~8%. This deviation is comprehensible for the tolerance levels of these measurements and the assumed uniform solid distribution of the model. If the solid dielectric constant is assumed to be 9.6, Eq. 3.1.15 for $\phi \leq 0.02$ becomes

$$\frac{C_M - C_F}{C_F} = 2.22\phi$$

and matches the sensitivity term of DM SVF linear relationship shown in Eq. 4.1.8.

4.2 PARTICLE VELOCITY

Nonintrusive sensing devices using the cross-correlation technique for the measurement of particle velocity have been used in a number of applications.[8,9,12,14,15,25-32] The present set of solid/gas flow tests with the CF included an independent measure of the solids velocity based on times-of-flight of injected radioactively tagged particles, and, thus provided a measure of flow instrument readout errors and scale factors.

With a 100 kHz driving frequency the CF velocity-sensing electrodes detected instantaneous changes in the dielectric media within the sensing fields defined by the lengths of the electrodes. Cross-correlation functions were computed from the amplitude-demodulated signals originating

from the velocity electrodes with the DSP described in Sec. 3.2.3. The basics of cross-correlation velocity measurements have been discussed in Sec. 3.1, yielding Eq. 3.1.10 that relates the peak offset time t_p to the true duct-averaged solid velocity. In these, as in previous tests, the CCF, defined by Eq. 3.1.5 was computed off-line from analog records derived from several electrodes. As described in Sec. 3.2.3 the records were stored on FM multitrack tape together with the time information that permitted selection of records coinciding with steady flow conditions.

In order to secure a level of time resolution that would allow an accurate peak location by visual inspection of a CCF display rather than through computation, the CCF was computed at a 20 kHz sampling rate. Samples of these CCF computations are presented in Fig. 4.2.1 for the three electrode spacings indicated on the figure of 4, 8, and 12 cm (1.6, 3.1, 4.7 in.) for solid feedrates of 3.2 and 4.4 lb/s with actual particle velocities of 25.1 and 24.0 m/s respectively. All CCFs are symmetrical with distinct maxima. Transit times, for the 3.2 lb/s flow test, are 1.65, 3.29, and 4.94 ms, respectively, for the 4, 8, and 12 cm spaced electrodes. This transforms to a 24.29 m/s particle velocity while the average particle velocity, as measured by the irradiated particle velocimeter, was 25.09 m/s (in a 5.25 cm [2-in.] Schedule 40 pipe). The particle velocities derived from the CF CCF agreed to within 5% of the actual average particle velocities for the range of 21 to 31 m/s and solid concentrations ranging from 0 to 1.6 Vol%.

Figure 4.2.1 shows the results of the derived CCFs for all the variously spaced electrodes during the two high solid feedrates, 3.8 and 4.4 lb/s (Runs 113 and 111 in Table 2.3.2). For the 4.4 lb/s test, there was a sharp symmetrical peak on a broadening increase in the CCF base level. As discussed in Appendix C, this could be the result of an oscillatory delivery in the mixing tee that tends to develop for high SGL ratios. The cluster length comes to about 30 cm for an estimated 12.5 ms time width at 25 m/s velocity; hence, the oscillation frequency should be less than 80 Hz (1/12.5 ms). Figure 4.2.2 shows the result of imposing a high-pass filter at 71 Hz, which effectively removes the CCF peak resulting from the passage of "natural" or Poisson configuration clusters (discussed in Appendix C), retaining the more or less pure "artificial" or injection tee cluster effect with a 12.5 ms width. The apparent shift to a faster transit time of 3.52 ms is not necessarily an indication of a higher cluster speed but could be a "Moiré" pattern effect, similar to effects observed in optics with discrete wavelength sources.

Another type of measurement that allows one to determine the optimum spacing between the electrodes is the cross-correlation coefficient. The degree of correlation between two electrode signals for the 4 to 18 cm range of electrode pair separations is determined by the correlation coefficient as given by,[33]

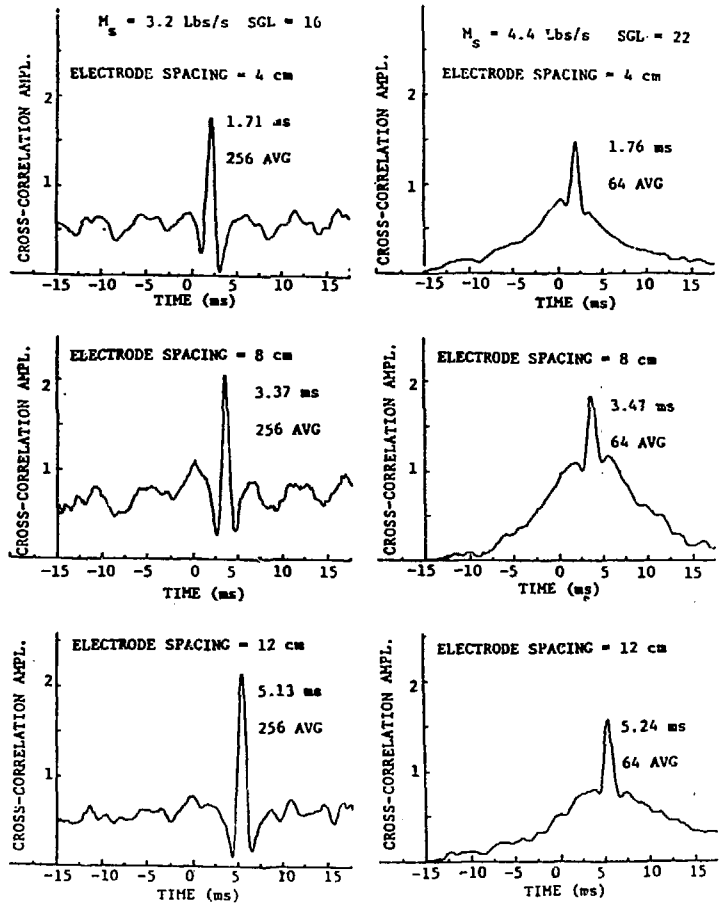

Fig. 4.2.1. Typical Capacitive Flowmeter Measured Cross-correlation Functions at (1) M_s = 3.2 lb/s and V_p 25.1 m/s and (2) Ms = 4.4 lb/s and V_p = 24.0 m/s for 4, 8 and 12 cm Spaced Electrodes

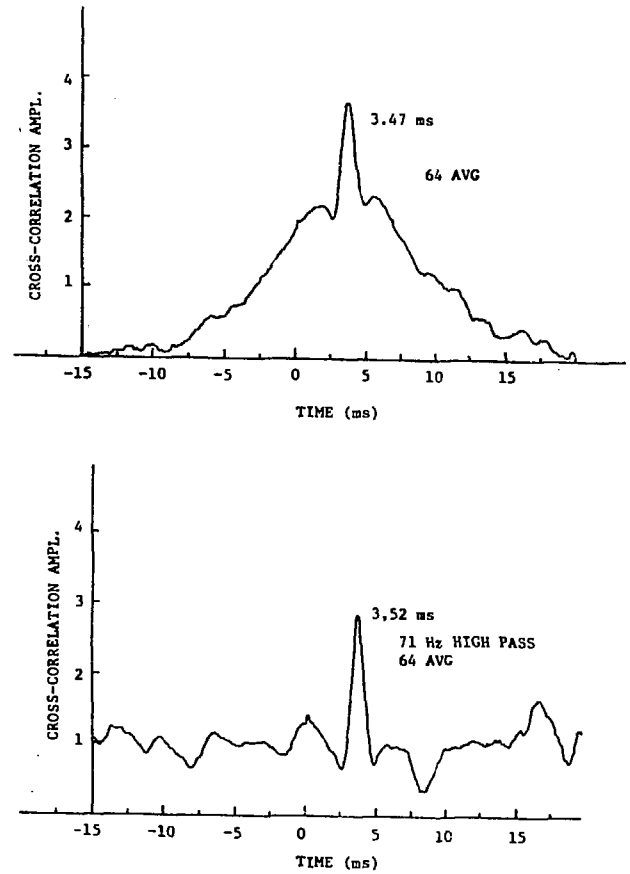

Fig. 4.2.2. Typical Capacitive Flowmeter Measured Cross-correlation Function With and Without 71 H_z High Pass Filter at M_s = 4.4 lb/s and SGL = 22 for 8 cm Spaced Electrodes

$$\rho_{xy} = \frac{CCF_{xy}(0)}{[ACF_x(0)ACF_y(0)]^{1/2}} \qquad 4.2.1$$

where ACF is the autocorrelation function. The autocorrelation functions peak at zero offset where they amount to ordinary signal variances. For two exactly equal signals, the variances are equal and a correlation coefficient of unity indicates a perfect correlation. The correlation coefficient equals zero where there is an absence of correlation.

The cross-correlation coefficient was computed on the DSP with signals from electrode pairs separated by 4, 8, 12, and 18 cm for SGL ratios of 6.5, 10.2, 16.6, and 22.0 corresponding to a range of SVF values extending from 0.004 to 0.016. A plot of the computed coefficients vs spacing is presented in Fig. 4.2.3. If the increase at 12 cm is disregarded the coefficient shows the predicted decline with increasing distance. Another trend is towards higher persistence as well as stronger correlation with increasing SGL's, whereas one would assume that a higher SVF and concomitant higher particle-particle collision frequency would lead to a more rapid reconfiguration of clusters. Here again, the appearance of density oscillations through injection that was noted in Fig. 4.2.2 might have a significant effect. Table 4.2.1 summarizes these data, including error estimates.

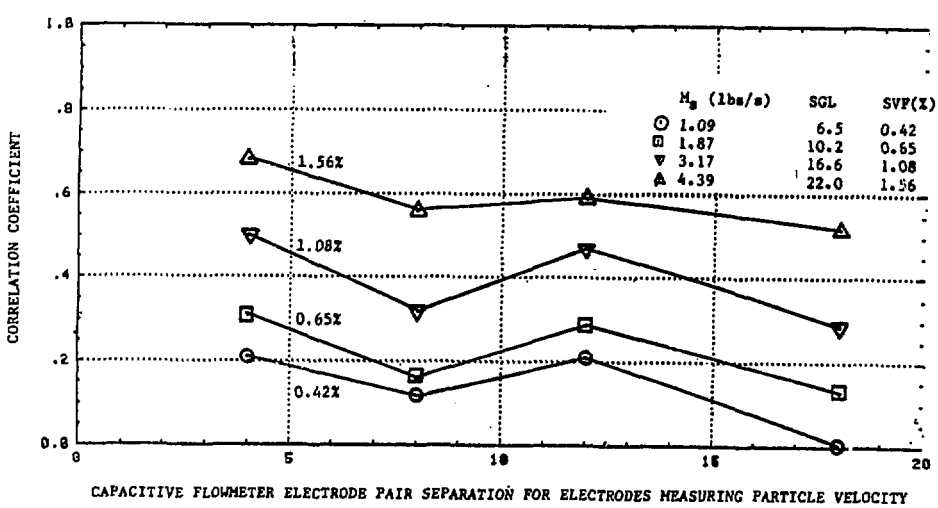

Fig. 4.2.3. Correlation Coefficient for Various Electrode Separations Used for the Capacitive Flowmeter Measured Particle Velocity for a Range of Solid Volume Fraction Values

Table 4.2.1. Correlation Coefficient for Various Electrode Separations Used for the Capacitive Flowmeter Measured Particle Velocity for a Range of Solid Volume Fraction Values

Run	Solid Feedrate (lb/s)	SVF (%)	Correlation Coefficient, by Electrode Separation Distance 4 cm	8 cm	12 cm	18 cm
112	1.09	0.42	0.21 ± 0.01	0.12 ± 0.01	0.21 ± 0.03	0.0
110	1.87	0.65	0.31 ± 0.01	0.16 ± 0.02	0.29 ± 0.02	0.13 ± 0.02
109	3.17	1.08	0.50 ± 0.09	0.32 ± 0.06	0.47 ± 0.04	0.29 ± 0.08
111	4.39	1.56	0.68 ± 0.05	0.56 ± 0.05	0.59 ± 0.02	0.52 ± 0.04

The time response of the CF particle velocity measurement is primarily determined by the cross-correlation processing time, which increases, as shown by Eq. 3.1.5 with the number of samples. The CCFs shown in Fig. 4.2.1 were obtained from the linear average of 256 CCFs where each CCF was computed with 1024 sample points at a 20 kHz sampling frequency and the resulting processing time was 16 s. If the number of CCFs averaged is reduced, the processing time can be shortened without reducing the sharpness of the peak being formed or altering the peak position. The CCF computed with 1, 2, and 4 linear averages is shown in Fig. 4.2.4. Correlograms with distinct maxima were observed for the 2 and 4 linear averaged CCF with the processing time being reduced from 16 s to 0.13 and 0.25 s respectively.

The cumulative results of the CF particle velocity measurement are summarized in Table 4.2.2 where the particle velocity for the 4, 8 and 12 cm spaced electrodes is tabulated along with the resulting computed average value and the actual particle velocity. For each electrode pair the average particle velocity was computed from

$$PV_{CF} = \sum_{i=1}^{10} \frac{d_e}{t_i} \qquad 4.2.2$$

where d_e is the center-to-center separation of a pair of velocity electrodes and t_i is the particle transit time computed with 1 to 10 CCFs where each CCF is an average of 64 CCFs. The CF-measured particle velocity was independent of the chosen electrode separation since the average relative deviations, as shown in Table 4.2.2, of the CF particle velocity computed with Eq. 4.2.3 for each of the 6 pairs of electrodes was <1%. Figure 4.2.5 shows a plot of the average CF particle velocity for 4, 8, and 12 cm electrodes versus the actual particle velocity, as measured by the irradiated particle velocimeter at the CF location. The particle velocities agreed to within 5% for the range of 21 to 31 m/s and solid concentrations ranging from 0 to 1.6 vol%. The CF measured particle velocity was linearly proportional to the actual particle velocity according to the relationship

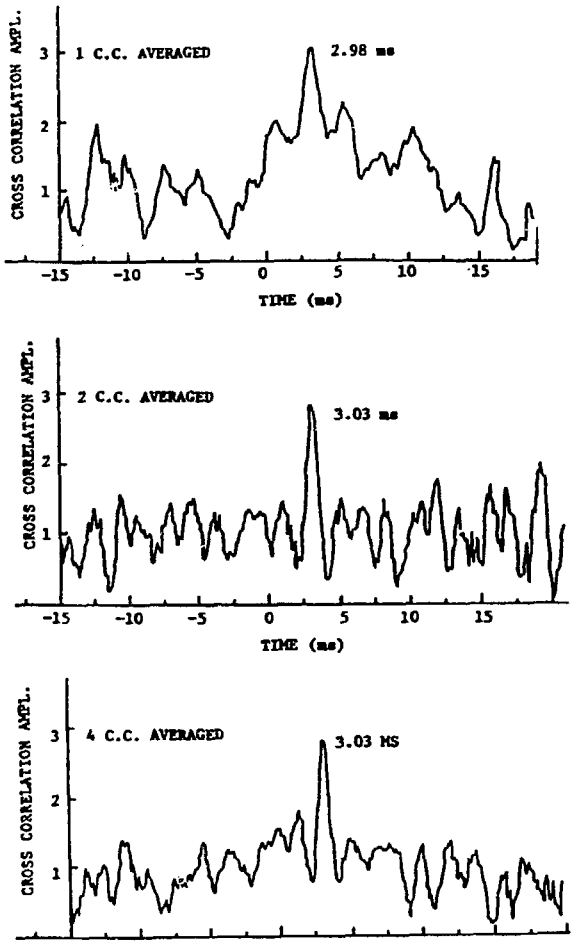

Fig. 4.2.4. Typical Capacitive Flowmeter Measured Cross-correlation Functions for 1, 2, and 4 Averaged Cross Correlations at M_S = 3.2 lb/s and SGL = 16 for 8 cm Spaced Electrodes

Table 4.2.2. Capacitive Flowmeter Measured Particle Velocities[5] for a Range of Irradiated Particle Velocities

	Gas Velocity (m/s) ← Region →			Mean Particle Velocity (m/s)[4]			
Run	Gas[1] Only	7.30m[2]	CF[3]	CF	Irrad. Part.	% Diff.	SVF (%)
112	25.79	28.04	28.25	21.87	21.98 ± 0.3	-0.5	0.42
110	25.92	29.68	30.02	23.36	24.48 ± 0.4	-4.5	0.65
109	24.58	29.63	30.28	24.29	25.09 ± 0.5	-3.2	1.08
111	23.46	29.08	29.59	23.57	24.01 ± 0.5	-1.8	1.56
114	30.72	37.68	38.08	30.66	30.41 ± 0.4	0.8	0.75
113	29.29	37.56	38.11	30.27	30.56 ± 0.3	0.9	1.05

(1) Orifice meter

(2) 7.30 m from Solid/Gas mixing tee

(3) 8.83 m from Solid/Gas mixing tee

(4) PV_{IP} = irradiated particle velocity
PV_{CF} = capacitive flowmeter measured particle velocity
PV_{CF} = -.16 + 0.99 PV with 0,0 data point

	CF Particle Velocity ← Electrode Separation →			
Run	4cm	8cm	12cm	Avg.
112	21.90 ± .4	21.98 ± .5	21.73 ± .3	21.87 ± .1
110	23.31 ± .2	23.36 ± .2	23.41 ± 0.0	23.36 ± .1
109	24.25 ± 1.	24.34 ± 1.	24.28 ± 1.	24.29 ± .1
111	23.24 ± .6	23.48 ± .7	23.99 ± 1.	23.57 ± .4
114	30.22 ± 1.	31.05 ± 1.	30.70 ± 1.	30.66 ± .4
113	30.05 ± .8	31.20 ± 1.	29.56 ± .3	30.27 ± .8

(5) All CF particle velocity measurements were made using the cross correlation technique. The time resolution was approximately 1% of the measured time delay.

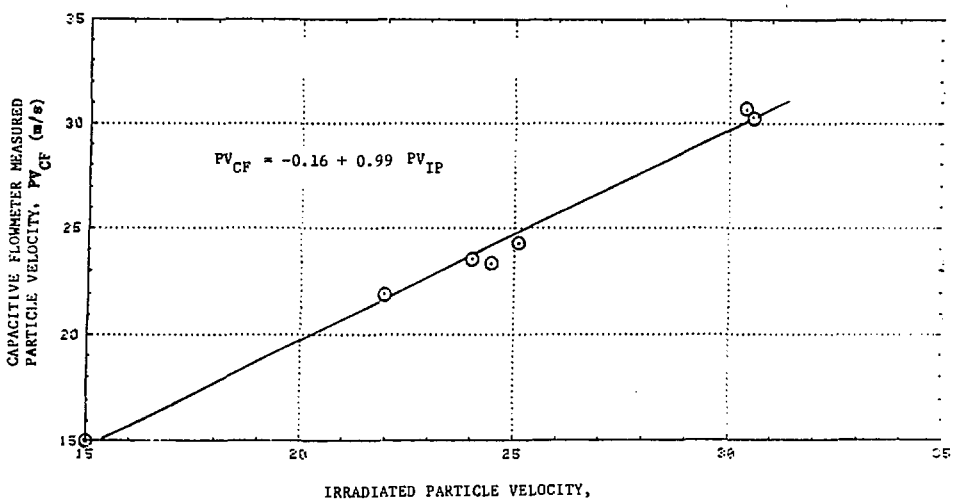

Fig. 4.2.5. Capacitive Flowmeter Measured Particle Velocity vs. Irradiated Particle Velocity

$$PV_{CF} = -0.16 + 0.99\ PV_{IP} \qquad 4.2.3$$

where

PV_{CF} = the CF measured particle velocity, and
PV_{IP} = the irradiated particle velocity.

The CF measured velocity reasonably extrapolated to zero particle velocity when the actual particle velocity was zero.

4.3 MASS FLOWRATE

Since the goal was to measure mass flow, the CF combined SVF and particle velocity measurements are plotted versus the measured solid feedrate in Fig. 4.3.1. As expected, the CF measured mass flow was linearly proportional to the solid feedrate by the relationship

$$CF_{MF} = -0.05 + 3.49\ M_s \qquad 4.3.1$$

where

CF_{MF} = the product of the CF measured SVF (volts) and the particle velocity (m/s), and

M_s = solid feedrate (lb/s).

This functional dependence permits the CF to predict the solid feedrate since the two CF separate measurements were calibrated during these solid/gas flow tests. Table 4.3.1 summarizes the CF SVF and particle velocity measurements.

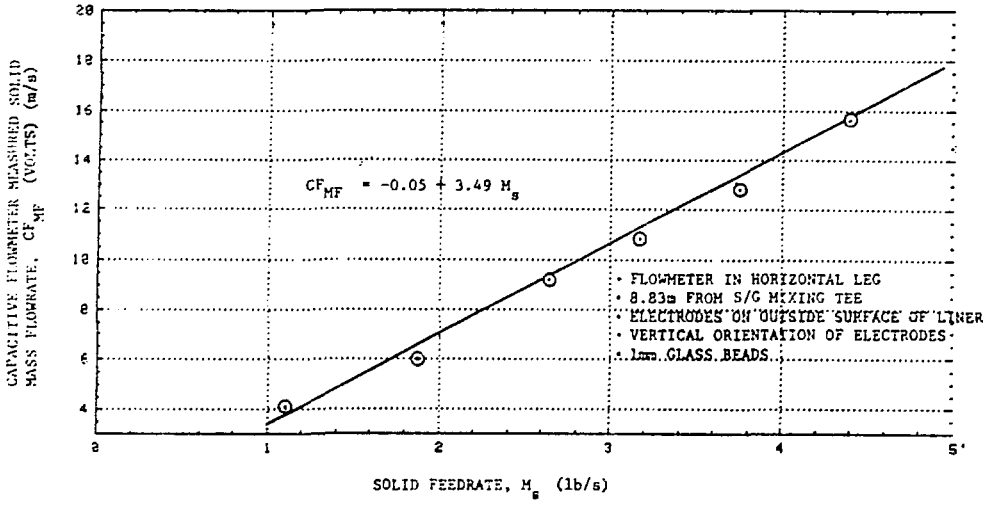

Fig. 4.3.1. Capacitive Flowmeter Measured Solid Mass Flowrate for a Range of Solid Feedrates

Table 4.3.1. Capacitive Flowmeter Measured Solid Mass Flowrate for a Range of Solid Feedrates

Run	Solid Feedate (lb/s)	Particle Velocity (m/s)	Capacitive Flowmeter: Solid Volume Fraction Signal (Volts)	Capacitive Flowmeter: Solid Mass Flowrate[1] (Volts)(m/s)
112	1.09	21.87	0.189	4.13
110	1.87	23.36	0.258	6.03
109	3.17	24.29	0.445	10.81
111	4.39	23.57	0.663	15.63
114	2.65	30.66	0.300	9.20
113	3.75	30.27	0.425	12.86

[1] CF solid mass flowrate = -0.05 + 3.49 M_s with 0,0 data point.

5. SUMMARY AND CONCLUSIONS

The work reported here has demonstrated the performance of two types of nonintrusive instruments using the capacitive principle, the capacitive flowmeter (CF) with electrodes on the outside surface of a ceramic liner and the densitometer with electrodes flush with the duct interior. They measure respectively the solid component feedrate and the solid volume fraction (SVF) in a solid/gas flow stream. Both instruments incorporate a simple, low-cost guard-strip-modified wrapped plate design with 120° coverage which results in sufficient sensing of the duct interior while minimizing the readout error due to a nonuniform electric field. It has been substantiated that the solid component feedrate can be measured accurately using the CF and associated electronics. This was shown by a separate measurement of the solid component velocity, made by determining the particle transit time between sensing electrodes with the computed cross-correlation function, and by an associated measurement of the SVF. The particle velocity measurement was within 5% of the actual particle velocity with a minimum processing time of 0.13 s for the 21 to 31 m/s range of particle velocities (Sec. 4.2). For a SVF less than 0.016, an accurate formula for predicting the SVF from the capacitance measurement and the known solid and gas component dielectric constants was presented and verified (Sec. 4.1.1 and 4.1.2).

Regarding the test series, an accurate solid component velocity scheme was used to evaluate the performance of the capacitive instruments. The maximum error of this irradiated particle velocimeter was 1.5% and allowed a reliable basis for calibrating the CF particle velocity measurement. The actual SVF at the location of each capacitive instrument was inferred from the solid feedrate and the irradiated particle velocimeter where the computed SVF uncertainty was <3%.

The serious problem connected with the instrument readout error when solid density distributions are nonuniform was addressed. While the error estimates cannot be directly applied to a duct of circular cross section, it can be concluded with reasonable assurance that the error remains negligible in magnitude. This again suggests that the simple and cheaply constructed wrapped plate geometry used in these tests provides the maximum plate area with a uniform field.

A final topic germane to the development of CFs is whether or not a different orientation of the plates, with respect to the vertical, yields a difference in the capacitance readout in horizontal and vertical pipe flows. For the CF to provide a readout of the solid feedrate suitable for long-term unattended operation in an industrial plant, the signal conditioning electronics, which includes a simple computer chip system, must be developed. Lastly, the capacitive flowmeter performance and verification of the mathematical model should be conducted with SVF in the range of 0.016 to 0.06.

ACKNOWLEDGMENTS

The authors acknowledge the assistance of R. J. Armani, E. F. Bennett, T. S. Yule, and R. R. Hopf (ATSR) in operating of the reactor and to OHS personnel for radiation monitoring of the irradiated particles during the tests. The authors want to thank E. D. Doss, W. Lawrence, S. H. Sheen, and M. G. Srinivasan for their assistance during the installation of the instrumentation and operation of the facility, and C. E. Cohn, J. A. Mormon, and Z. Johnson for assistance in the software development associated with the irradiated particle velocimeter. The authors thank N. Heeg and J. Fisher for their typing and preparation of the figures.

Finally the authors wish to thank L. G. LeSage, R. S. Zeno, G. S. Rosenberg, T. P. Mulcahey, and M. Petrick (ANL) for their managerial support and encouragement.

APPENDIX A
THE BULK DIELECTRIC CONSTANT OF UNIFORM MIXTURES

The quantitative prediction of bulk properties of two-phase mixtures is of an obvious interest for industrial process control. An on-line measurement of the bulk parameter and a prediction formula would allow the composition of the medium to be inferred, hence, the blend to be varied as desired. However, the detailed interactions within the mixed medium tend to be too complex to permit a straightforward derivation of a formula from a model. It is only when one of the components is present at high dilution, so that terms of higher powers in its concentration or volume fraction can be dropped, that a direct computation formula can be obtained that relates the solid fraction, bulk parameter, and individual phase parameters. Another approach, strongly represented in the voluminous literature on the subject, is to try fitting available measurements with a heuristic formula that can cover the complete range of volume fractions within a 10% error.

In particular, the bulk dielectric constant, magnetic permittivity or electrical conductivity of uniform solid/solid, solid/liquid, liquid/gas and solid/gas mixtures, alloys, suspensions and dispersions cannot be predicted or modeled accurately over the range of compositions that may be of interest in some specific application. Instruments using a bulk measurement capacitive densitometer, conductivity meter, nuclear magnetic resonance, or microwave dentitometer must be elaborately calibrated for the exact components and over a temperature range that encompasses site temperatures. The calibration must be repeated if one of the components changes.

Fortunately, however, typical conditions that promote smooth gas-entrained solids flow in a duct imply very low SVF values (<0.02), that are well within the range of the direct formulae based on modeling. Moreover, many of the heuristic formulas that have been proposed also tend to fit somewhat better at low concentrations of the solid than elsewhere, as will be shown in the following examples. First, however, we shall briefly discuss the obstacles that prevent an exact calculation of the bulk dielectric constant.

For expository purposes, we consider homogeneous and isotropic molecular medium. For that case, a certain polarization P per unit volume is induced by an applied electric field, to which it is related by the medium dielectric constant κ through

$$4\pi P = (K - 1)E_{appl} \qquad \text{A.1}$$

Equation A.1 is valid locally within the dielectric and its validity extends over the entire medium if the applied field E_{appl} is uniform, as for a parallel-plate capacitor; P and E_{appl} are always aligned if the medium is

isotropic. The polarization per unit volume is, in turn, the combined effect of n_m induced molecular dipoles per unit volume, each of strength

$$p = \alpha E_{loc} \qquad \text{A.2}$$

where α is defined as the molecular polarizability and has the dimension of a volume. E_{loc} is the electric field at the molecule, and includes both the external field E_{appl} and the effect of surrounding molecules. Now for uniform (homogeneous and isotropic) dielectrics such as gases or liquids, a straightforward calculation[34,35] yields

$$E_{loc} = E_{appl} + \frac{4\pi P}{3}. \qquad \text{A.3}$$

To the extent to which Eq. A.3 truly describes the local field, one finds, with the use of Eq. A.1, the Lorentz identity

$$E_{loc} = E_{appl}\frac{(K + 2)}{3} \qquad \text{A.4}$$

and with Eqs. A.1 and A.2 one finds

$$\frac{K - 1}{K + 2} = \frac{4\pi n_m \alpha}{3} \qquad \text{A.5}$$

which is known as the Clausius-Mosotti law for a homogeneous and isotopic dielectric that contains no permanent dipoles. If now the dielectric contains several (i.e., M) different molecules, Eq. A.5 becomes

$$\frac{K_m - 1}{K_m + 2} = \frac{4\pi}{3} \sum_{i=1}^{M} n_i \alpha_i \qquad \text{A.6}$$

in terms of the medium dielectric constant K_m. For a mixture of two gases, Eq. A.6 reduces to

$$\frac{K_m - 1}{K_m + 2} = \frac{4\pi}{3} \left(\frac{\phi_1 \alpha_1}{v_1} + \frac{(1 - \phi_1) \alpha_2}{v_2}\right) \qquad \text{A.7}$$

where

ϕ_1 = volume fraction of component 1,

v_1, v_2 = molecular volumes of components 1, 2.

For gases, $v_1 = v_2 = 3.7 \times 10^{20}$ cm^3. Substitution of Eq. A.5 reduces Eq. A.7 to

$$\frac{K_m - 1}{K_m + 2} = \frac{\phi_1 (K_1 - 1)}{K_1 + 2} + \frac{(1 - \phi_1)(K_2 - 1)}{K_2 + 2} . \qquad \text{A.8}$$

Equation A.8 has been verified for mixtures of gases.

Now, suppose that Eq. A.8 can predict, to a reasonable approximation, the bulk dielectric constant of a solid suspension of very small particles. The solid component can be denoted by subscript s ($K_1 = K_s$) and the fluid or gas by subscript f ($K_2 = K_f$). Rearranging Eq. A.8 yields

$$\frac{K_m - K_f}{K_m + 2} = \phi \frac{(K_s - K_f)}{K_s + 2} . \qquad \text{A.9}$$

Let us introduce, for convenience, the dielectric constant ratios

$$G = \frac{K_m - K_f}{K_f} \qquad \text{A.10}$$

which equals the relative change in capacitance, and

$$g = \frac{K_s - K_f}{K_f} . \qquad \text{A.11}$$

In terms of these ratios, Eq. A.9 becomes

$$G = \frac{g\phi}{1 + \frac{g(1 - \phi) K_f}{2 + K_f}} . \qquad \text{A.12}$$

More specifically, if the fluid is air, $K_f = 1$ and Eq. A.12 reduces to

$$G = \frac{g\phi}{1 + \frac{g(1 - \phi)}{3}} . \qquad \text{A.13}$$

This final result is a prediction based on the apparent analogy between a

molecular mixture of two different gases and a fine-particle suspension.

We turn now to another model, representing the solid component in the form of slabs interleaved with spaces that contain the fluid. The slab thickness-to-spacing ratio is adjusted to the desired solid volume fraction. Slabs can be set normal or parallel to the plates that produce a uniform field throughout, and thus form a set of parallel-connected or series-connected capacitors.

For the parallel connection (slabs normal to plates), as shown below,

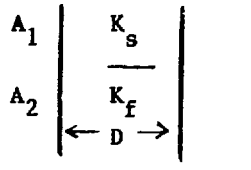

the total capacitence is

$$\frac{K_m A}{D} = \frac{K_s A_1}{D} + \frac{K_f A_2}{D} . \qquad \text{A.14}$$

The solid and fluid volume fractions are given, respectively, by

$$\phi = \frac{A_1 D}{AD} \qquad \text{A.15}$$

and

$$1 - \phi = \frac{A_2 D}{AD} . \qquad \text{A.16}$$

Substitution of Eqs. A.15 and A.16 into A.14 yields

$$K_m = K_s \phi + K_f (1 - \phi) \qquad \text{A.17}$$

which, upon introducing the dielectric constant ratios, reduces to

$$G = g\phi . \qquad \text{A.18}$$

For the series connection (slabs parallel to plates), as shown below,

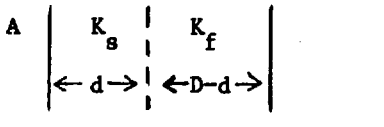

the total capacitance is

$$\frac{1}{\frac{K_m A}{D}} = \frac{1}{\frac{K_s A}{d}} + \frac{1}{\frac{K_f A}{D-d}} . \qquad \text{A.19}$$

The solid and fluid volume fractions are given, respectively, by

$$\phi = \frac{Ad}{AD} \qquad \text{A.20}$$

and

$$1 - \phi = \frac{A(D - d)}{AD} . \qquad \text{A.21}$$

Substitution of Eqs. A.20, A.21 into A.19 yields

$$\frac{1}{K_m} = \frac{\phi}{K_s} + \frac{1 - \phi}{K_f} \qquad \text{A.22}$$

which, upon introducing the dielectric constant ratios, reduces to

$$G = \frac{g\phi}{1 + g\,(1 - \phi)} \qquad \text{A.23}$$

The slab model, which has been used occasionally, agrees roughly with the molecular mixture model (Eq. A.13) when averaged over both slab orientations.

A more serious modeling scheme was introduced by Maxwell.[36] Representing the solid component as a regular array of spheres embedded in a continuum of different dielectric constant, he solved the Poisson equation with periodic boundary conditions by expanding in spherical harmonics. This yields a set of conditional equations for the coefficients of the Legendre Polynomials; the coefficients can be expressed in terms of the solid and continuum dielectric constants and the SVF. Including coefficients to the second order only, one thus obtains the approximate relation

$$\frac{K_m - K_f}{K_m + 2K_f} = \frac{\phi(K_s - K_f)}{K_s + 2K_f} \qquad \text{A.24}$$

which, upon introducing the dielectric constant ratios, yields

$$G = \frac{g\phi}{1 + \frac{g}{3}(1 - \phi)} \qquad A.25$$

which is identical to the molecular mixture model.

Thus, A.25 that was derived from a model in which solid particles were explicitly modeled, and is known to be accurate only to the second order in the SVF, agrees with a model that proceeded by ad hoc assumptions, and then was restricted to a gas only, but not to small solid fractions. Rayleigh[37] computed the next higher Legendre polynomial coefficient, and found that calculation to be very complex, requiring a number of simplifying assumptions to obtain a closed form. Moreover, if the solid fraction is large enough, terms of the fourth and higher orders cannot be neglected, but can no longer be based on a regular array; instead these terms must allow for the random location of the solid grains. This was discussed more recently by Brown,[38] who obtained a number of integral equations involving statistical distributions of particles.

From this, it becomes clear that the approximate treatment of a suspension of small particles as a molecular gas mixture can be acceptable only for a highly dilute suspension when the local induced dipoles that the particles represent are too far apart to interact, but will break down when such interactions become more prominent. On the other hand, the concentration of the solid component into slabs is not allowable because the extremely strong local interactions through the slab evidently cause a concomitant field distortion that carries into the adjacent continuum. The reverse case, that of gas bubbles within a solid, yields quite different predictions when modeled (Rayleigh-Maxwell) and when based on an ad hoc analogy (molecular mixture).

Another sphere model, more recently developed by Bottcher,[39] was based on the Onsager equation[40] (an improved version of the Clausius-Mosotti law in Eq. A.5). Bottcher's formula is as follows:

$$\frac{G}{1 + G} = \frac{3g\phi}{g + 3 + 2G} \qquad A.26$$

which can be rearranged in the form

$$G = \frac{g\phi}{1 + \frac{g(1 - \phi)}{3} - \frac{2g^2\phi}{3(g + 3)} \cdots} \qquad A.27$$

which differs from Eq. A.13 only by a small term.

We turn now to a number of formulas for representing the bulk dielectric constant approximately, over the full range of component volume fractions. Since such formulas are "anchored" at both extremes, one would expect them to yield predictions for small solid fractions that are in reasonable agreement with the modeling formulas presented above.

First, the empirical fit by Bruggeman[41] can be expressed as

$$\frac{g - G}{g} = (1 - \phi)\,(1 + G)^{1/3} \qquad \text{A.28}$$

which upon rearrangement becomes

$$G = \frac{g\phi}{1 + g\,\frac{(1 - \phi)}{3} - \frac{g^2\phi}{3(g + 3)} \ldots} \qquad \text{A.29}$$

Secondly, an equation suggested by Landauer,[42] based on a symmetry argument that seems unconvincing, comes to

$$\frac{\phi(g - G)}{g + 3 + 2G} = \frac{(1 - \phi)G}{3 + 2G}\,. \qquad \text{A.30}$$

This can be rearranged to read

$$G = \frac{g\phi}{1 + g\,\frac{(1 - \phi)}{3} - 2\,\frac{g^2\phi}{3(3 + g)} \ldots} \qquad \text{A.31}$$

and thus seems to agree to the second order with the Bottcher modeling equation.

Lastly, a model formerly much used, by Lichtenecker,[43] averages the logarithms of component dielectric constant in the same way as the slab model averaged the constants linearly or reciprocally. This formula reads

$$\log K_m = \phi \log K_s + (1 - \phi)\log K_f \qquad \text{A.32}$$

hence

$$\frac{K_m}{K_f} = \left(\frac{K_s}{K_f}\right)^{\phi}$$

leading to

$$G = (1 + g)^{\phi} - 1 \ , \qquad \text{A.33}$$

or, expanded,

$$G = g\phi[1 - \frac{g(1 - \phi)}{2} + \frac{(1 - \phi)\ (2 - \phi)g^2}{6}$$

$$- \frac{(1 - \phi)\ (2 - \phi)\ (3 - \phi)g^3}{24} \ldots] \qquad \text{A.34}$$

Equation A.34 evidently deviates considerably from the rest of these expressions.

The model formulas are summarized in Table A.1. Inspection shows that $G = 0$ and $G = g$, respectively, for $\phi = 0$ and $\phi = 1$. In sum, a number of formulas that is by no means inclusive but may be representative of the literature on the subject can be shown, by means of expansion and dropping of third and higher-order terms, to resemble each other. This lends some support to the basic Maxwell-Rayleigh formula (Eq. A.13). Of all these equations, Eq. A.13 has the most solid foundation in a model that also serves to illustrate why a really accurate expression that covers the entire range of compositions is likely to remain unavailable.

Table A.1. Model Formulas for Solids Suspended in Fluid[1]

Name	Model	
Dielectric perpendicular to electrodes	$G = g\phi$	$K_m = K_s\phi + K_f(1-\phi)$
Dielectric parallel to electrodes	$G = \frac{g\phi}{1 + g(1-\phi)}$	$\frac{1}{K_m} = \frac{\phi}{K_s} + \frac{(1-\phi)}{K_f}$
Maxwell-Rayleigh	$G = \frac{g\phi}{1 + \frac{g}{3}(1-\phi)}$	$\frac{K_m - K_f}{K_m + 2K_f} = \frac{(K_s - K_f)\phi}{K_s + 2K_f}$
Bottcher-Onsager	$G = \frac{g\phi}{1 + \frac{g}{3}(1-\phi) - \frac{2g^2\phi}{3(g+3)}}$	$\frac{K_m - K_f}{3K_m} = \frac{(K_s - K_f)\phi}{K_s + 2K_m}$
	$\frac{g - G}{g} = (1-\phi)(G+1)^{1/3}$	
Bruggeman	$G = \frac{g\phi}{1 + \frac{g}{3}(1-\phi) - \frac{g^2\phi}{3(g+3)}}$	$\frac{K_s - K_m}{K_s - K_f} = (1-\phi)\left(\frac{K_m}{K_f}\right)^{1/3}$
Landauer	$G = \frac{g\phi}{1 + \frac{g}{3}(1-\phi) - \frac{2}{3}\frac{g^2\phi}{g+3}}$	$\frac{(K_s - K_m)\phi}{K_s + 2K_m} = \frac{(\phi - 1)(K_f - K_m)}{K_f + 2K_m}$
Lichtenecker	$G = (1+g)\phi - 1 = g\phi\left[1 - g\frac{(1-\phi)}{2} + \frac{g^2(1-\phi)(2-\phi)}{3!} - \ldots\right]$	$\frac{K_m}{K_f} = \left(\frac{K_s}{K_f}\right)^{\phi}$

[1] In these equations ϕ = the solid volume fraction and the dielectric constant ratios g and G are defined as follows:

$$g = \frac{K_s}{K_f} - 1$$

$$G = \frac{K_m}{K_f} - 1$$

APPENDIX B
EFFECT OF NONUNIFORM SOLIDS DISTRIBUTION ON THE CAPACITIVE DENSITOMETER READOUT

In Appendix A it was established that even under the most favorable conditions, i.e., a uniform field and uniform solids distribution, there is no generally valid formula from which the composition can be inferred on the basis of a measurement of the effective medium capacity. However, several approximations that are valid for very low solid concentrations do exist and are in rough agreement.

While this seems to favor density measurement in gas-entrained solids flow where the solid fraction is inevitably small, a possibly serious problem may be connected with the typical existence of nonuniform density distributions in this flow regime. In particular, the solids tend to be concentrated along the axis (the "Magnus" effect) and are layered by gravitation in horizontal ducts. The Magnus effect has not been effectively addressed in existing capacitive densitometers, whereas the elimination or reduction of readout errors that might result from a vertical density gradient has received considerable attention, resulting in two somewhat similar "averaging" schemes.[20,22]

The basic supposition of any averaging stratagem is that readout errors of opposite sign and approximately equal magnitude are produced when the capacitor plates are aligned with, and normal to, the density gradient. A convincing verification of this supposition would require a rigorous analytical solution of the Poisson equation for a duct of circular cross section, in the presence of a realistic gradient, and for capacitor plates of a specified geometry. The complexity and difficulty of that task, and the cost of computer time it entails, suggest a reasonable alternative, a solution of the problem for a duct of square cross section, which is presented here. The density gradient is modeled as an exponential,

$$\phi(x) = \bar{\phi}\,\frac{e^{-\beta x}}{F} \qquad \text{B.1}$$

where

$$\bar{\phi} = \text{average solid volume fraction}\ , \qquad \text{B.2}$$

$$F(\beta) = \frac{1 - e^{-\beta}}{\beta} \qquad \text{B.3}$$

and

$$x = \frac{h}{H}, \qquad \text{B.4}$$

where

h = height above the bottom plane of the rectangular duct,

H = duct height.

The density gradient for several values of the scale parameter β is shown in Fig. B.1.

Initially the plates are assumed vertical, as indicated in Fig. B.2. The relation discussed in Appendix A is assumed to hold locally:

$$G(x) = \frac{3B\phi(x)}{1 - G_g\phi(x)} \qquad \text{B.5}$$

where

$$G(x) = \frac{C_M(x) - C_F}{C_F} \text{ (defined in Eq. A.10)} \qquad \text{B.6}$$

$$g = \frac{K_s}{K_f} - 1 \qquad \text{B.7}$$

$$B = \frac{g}{g + 3} \qquad \text{B.8}$$

and G_g corresponds to a particular model. Hence

$$C_M(x) = C_F[1 + \frac{3B\phi(x)}{1 - G_g\phi(x)}] \ . \qquad \text{B.9}$$

The models used in this analysis (Table A.1) and the expression for G_g are shown in Table B.1.

For this vertical plate arrangement, the individual slabs of thickness dx appear in parallel and hence from Eq. B.9 the overall solid plus gas capacitance, C_{MV}, is obtained by integration:

$$C_{MV} = \int_0^1 C_{MV}(x)dx = C_F \int_0^1 [\frac{3B\phi(x)}{1 - G_g\phi(x)}] \, dx \ . \qquad \text{B.10}$$

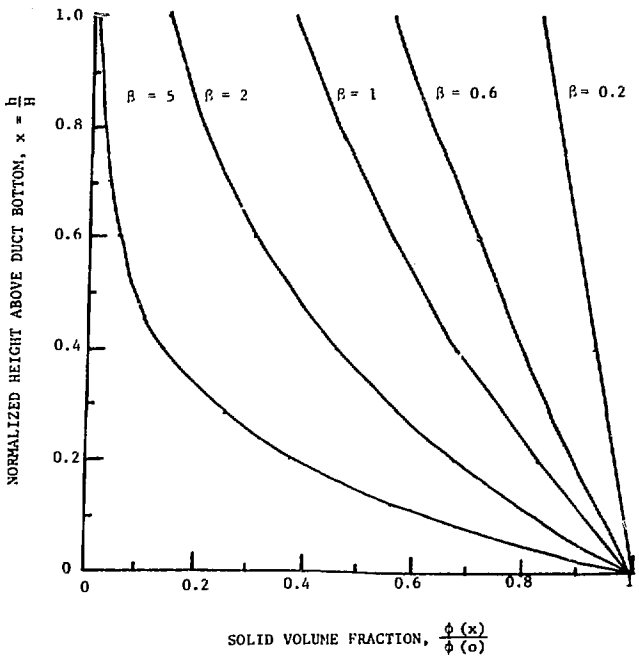

Fig. B.1. Solid Density Gradient as a Function of Scale Parameter β

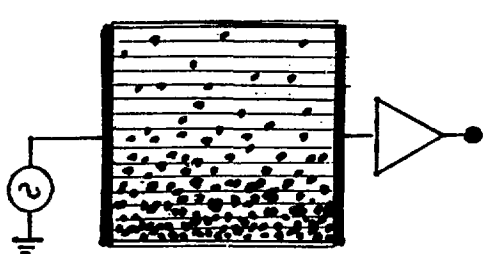

Fig. B.2. Parallel Vertical Plate Capacitor With Nonuniform Distribution of Solids

Table B.1. Model Formulas for Analysis of Nonuniform Solid Distribution in the Capacitive Flow Instrument†

Model	G	G_g
Maxwell/Rayleigh	$\dfrac{g\phi}{1 + \frac{g(1-\phi)}{3}} = \dfrac{\frac{3g}{3+g}\phi}{1 - \frac{g\phi}{3+g}}$	B
Bottcher-Onsager	$\dfrac{g\phi}{1 + \frac{g}{3}(1-\phi) - \frac{2}{3}\frac{g^2\phi}{(3+g)}} = \dfrac{\frac{3g}{g+3}}{1 - [\frac{g}{g+3} + \frac{2g^2}{(g+3)^2}]\phi}$	B(1 + 2B)
Bruggeman	$\dfrac{g\phi}{1 + \frac{g}{3}(1-\phi) - \frac{g^2\phi}{3+g}} = \dfrac{\frac{3g}{g+3}}{1 - [\frac{g}{g+3} + \frac{g^2}{(g+3)^2}]\phi}$	B(1 + B)
Landauer	$\dfrac{g\phi}{1 + \frac{g}{3}(1-\phi) - \frac{2}{3}\frac{g^2\phi}{3+g}} = \dfrac{\frac{3g}{g+3}}{1 - [\frac{g}{g+3} + \frac{2g^2}{(g+3)^2}]\phi}$	B(1 + 2B)

† The solid volume fraction, ϕ, is assumed to be <0.02.

Substitution of Eqs. B.1 and B.2 into Eq. B.10 and using the convenient second-order approximation

$$\frac{3B\phi(x)}{1 - G_g\phi(x)} = 3B\phi(x)\ [1 + G_g\phi(x)] \qquad \text{B.11}$$

yields

$$C_{MV} = C_F\int_0^1 [1 + \frac{3B\bar{\phi}e^{-\beta x}}{F} + \frac{3B\bar{\phi}^2}{F} G_g\ e^{-2\beta x}]\ dx \qquad \text{B.12}$$

$$C_{MV} = C_F\ [1 + 3B\bar{\phi} + 3BG_g\bar{\phi}^2\ \frac{\beta}{2}\ \coth\frac{\beta}{2}] \qquad \text{B.13}$$

For a uniformly dispersed solid with the same average solid fraction, $\bar{\phi}$, the capacitance is

$$C_{MU} = C_F\ [1 + 3B\bar{\phi} + 3BG_g\bar{\phi}^2] \qquad \text{B.14}$$

to the same approximation. The fractional error that results from the gradient becomes

$$e_v = \frac{C_{MV} - C_{MU}}{C_{MU}} = 3B\ G_g\bar{\phi}^2\ (1 - G_g\bar{\phi})[\frac{\beta}{2}\coth\left(\frac{\beta}{2}\right) - 1]/[1(3B - G_g)\bar{\phi}]\ . \qquad \text{B.15}$$

Expanding the hyperbolic cotangent, i.e.,

$$\coth\frac{\beta}{2} \simeq \frac{2}{\beta} + \frac{\beta}{6} - \frac{\beta^3}{360}$$

Eq. B.15 becomes

$$e_v = \frac{B\ G_g\bar{\phi}^2\beta^2\left(1 - \frac{\beta^2}{60}\right)}{4[1 + (3B - G_g)\ \bar{\phi}]}\ . \qquad \text{B.16}$$

This fractional error expression is sufficiently accurate when the average solid volume fraction, $\bar{\phi}$, is small in order to make Eq. B.5 valid at the highest concentration at the bottom of the duct.

The analysis is now repeated for a horizontal plate orientation, as indicated in Fig. B.3. The individual slabs of thickness appear in series and the overall solid plus gas capacitance, C_{MH}, is obtained by

$$\frac{1}{C_{MH}} = \frac{1}{C_F\int_0^1 \{1 + 3B\phi(x)\ [1 - G_g\phi(x)]\}^{-1}dx}\ . \qquad \text{B.17}$$

Rearranging and retaining again only second-order terms, this becomes

$$\frac{1}{C_{MH}} = \left(\frac{1}{C_F}\right)\int_0^1 [1 - 3B\phi + 3B(3B - G_g)\phi^2]\ dx \qquad \text{B.18}$$

$$= \left(\frac{1}{C_F}\right)\ [1 - 3B\bar{\phi} + 3B(3B - G_g)\bar{\phi}^2\ \left(\frac{\beta}{2}\right)\coth\left(\frac{\beta}{2}\right)]. \qquad \text{B.19}$$

Once again expanding and rearranging, one obtains, after some arithmetic, the fractional error due to settling,

$$e_h = \frac{-3B\ (3B - G_g)(1 - G_g\bar{\phi})\ \bar{\phi}^2\beta^2/1 - \beta^2/60)}{4\ [1 + (3B - G_g)\ \bar{\phi}]} \qquad \text{B.20}$$

The fractional error terms shown in Eqs. B.16 and B.20 are similar; their ratio is given by

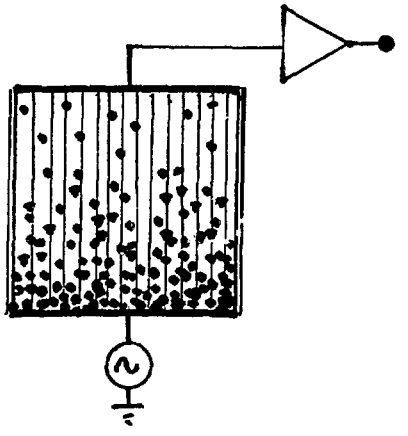

Fig. B.3. Parallel Horizontal Plate Capacitor With Nonuniform Distribution of Solids

$$\frac{e_V}{e_H} = \frac{G_g}{3B - G_g} . \qquad \text{B.21}$$

This ratio is presented in Table B.2 for the various models together with the values of the scaling parameter G_g for two cases of solid and fluid dielectric constants.

For the solid/gas case, glass beads with a dielectric constant of 7 are entrained by a gas with a dielectric constant of 1. The solid/liquid case corresponds to a solid with a dielectric constant of 5 entrained by a liquid with a dielectric constant of 2. A rather large dispersion of predicted error ratios is evident: while the errors have opposite signs the effective error cancellation through rotation or averaging remains in doubt. For gas-entrained solids, the error is in fact negligible inasmuch as β cannot be much larger than unity if saltation has not set in, while ϕ is at most 0.02.

The estimates summarized in Table B.2 cannot be directly applied to a duct of circular cross-section; however, it can be argued that they should represent the general trend for that case as well, assuming a quasi-uniform field and a highly dilute solid. Thus it can be concluded with some assurance that the error remains negligible in magnitude, hence, a simple and cheaply constructed plate configuration that provides the maximum feasible plate area and makes the field uniform seems to be a much more appropriate choice than the averaging geometries that have been described.[20,22]

For larger values of the solid fraction, as encountered in slurries, none of the formulas discussed in Appendix A can be relied on, nor can third-order terms be neglected. At the solid fraction level that is necessary to make slurry pipelines and/or direct combusion of coal slurries

Table B.2. Bulk Capacitance Error for a Nonuniform Solid Distribution in a Vertical and Horizontal Parallel Plate Capacitor

Name	Scaling Parameter, G_g	Ratio of Fractional Error Terms, $\frac{G_g}{3B - G_g}$	Solid/Gas Case(1)(2) G_g	Solid/Gas Case(1)(2) $\frac{G_g}{3B - G_g}$	Solid/Liquid Case(1)(3) G_g	Solid/Liquid Case(1)(3) $\frac{G_g}{3B - G_g}$
Maxwell-Rayleigh	B	$\frac{1}{2}$	$\frac{2}{3}$	$\frac{1}{2}$	$\frac{1}{3}$	$\frac{1}{2}$
Bottcher-Onsager	$B(1 + 2B)$	$\frac{1 + 2B}{2(1 - B)}$	$\frac{14}{9}$	$\frac{7}{2}$	$\frac{5}{9}$	$\frac{5}{4}$
Bruggeman	$B(1 + B)$	$\frac{1 + B}{1 - B}$	$\frac{10}{9}$	$\frac{5}{4}$	$\frac{4}{9}$	$\frac{4}{5}$
Landauer	$B(1 + 2B)$	$\frac{(1 + 2B)}{2(1 - B)}$	$\frac{14}{9}$	$\frac{7}{2}$	$\frac{5}{9}$	$\frac{5}{4}$

(1) $\frac{G_g}{3B - B_g} = \frac{e_v}{e_H}$ where e_v is as given in Eq. B.16 and e_H is given in Eq. B.20

(2) $K_s = 7$, $K_f = 1$, $g = 6$, and $B = \frac{2}{3}$

(3) $K_s = 5$, $K_f = 2$, $g = 1.5$ and $B = \frac{1}{3}$

cost-effective, one would not expect any significant gravitational settling, hence, the problem is moot. For more-dilute slurry flow, there may be some advantage in employing averaging capacitive densitometry. To the extent to which averaging samples the central region with more efficiency than the peripheral region, the Magnus effect, characteristic of dilute liquid/solid flow, could result in an error that is not addressed with the averaging stratagem. A convincing validation of these different plate geometries will have to be sought through a series of measurements for which a highly stable and accurately calibrated test system, such as the S/GFTF, is indispensable.

APPENDIX C
THE CROSS CORRELATION FUNCTION WITH CAPACITIVE SENSING IN GAS-ENTRAINED PARTICLE FLOW

This appendix traces the connection between what takes place within the duct and what is displayed on the screen of the correlator, i.e., plots as displaced in Fig. 4.2.1. It is well-established that the peak time offset in such a plot corresponds to the transit time of certain inhomogeneities in the moving medium between sensor stations (some 40 years have passed since the first reported use of cross correlation for velocity measurements). However, it has not been widely appreciated that other useful information can be learned from the processed signals, and that this information can then be applied to optimize the design of the system for a given medium. Some of this information will be discussed, using capacitive sensing as an example (though much of the material applies to other types of sensors).

As a preliminary step, consider the relation between the signal $S_i(t)$ and the number of particles within the detection volume V_D at time t, N(t). In terms of samples, S_i, taken at time t_i, is related to the number N_i. Let the overall channel conversion constant A_g include all fixed electronic parameters and let

$$K_{RS} = \frac{K_s - K_f}{K_s + 2K_f} . \qquad \text{C.1}$$

Then, assuming that $1 - \phi \cong 1$ in the denominator of the Rayleigh-Maxwell equation that is convenient for modeling the bulk dielectric constant,

$$S_i = A_g(C_{Mi} - C_F) = 3A_g K_{RS}\phi_i C_F \qquad \text{C.2}$$

where

C_{Mi} = capacitance measured at time C_i and
C_F = capacitance measured with no solids.

The solid volume fraction ϕ_i becomes

$$\phi_i = (v_p/V_D) \int dNi \qquad \text{C.3}$$

where

dN_i = number of particles in ith sample with radii between r and r + dr.

For particles that do not deviate strongly from an average particle volume V_d, Eq. C.3 becomes

$$\phi_i = \frac{N_i V_p}{V_D} . \qquad \text{C.4}$$

Let index j = u, d denote the sensing station. Then, using Eqs. C.2 and C.4 and letting

$$m = \frac{3K_{RS}V_p}{V_D} C_f , \qquad \text{C.5}$$

Eq. C.2 becomes

$$S_i = A_g m N_i . \qquad \text{C.6}$$

The fluctuations in the signal thus relate directly to fluctuations in the number of particles. Fluctuations in N_i evidently are similar in nature when samples are taken at successive times t_i at one point, and when simultaneous samples are taken at many points. To consider how the sample number varies in detail, let us first assume that ϕ = 0.001. At this high dilution, the mean number of 1 mm diameter particles in unit volume is only 2, the rate of collisions between particles is negligible and the sample number N_i is distributed entirely randomly:

$$P(N_i) = \bar{N}^{N_i} \frac{e^{-\bar{N}}}{N_i!} \qquad \text{C.7}$$

($\bar{N}$ = the average number of particles in volume V_D). Now consider a volume V_D that moves along the duct with the average solid velocity v_p, and that originally contains N_i particles. That number can change because of collisions between particles or because of individual particles having axial velocities that differ from the average. The latter effect only needs to be considered at high dilution and is of second order, whence N_i remains effectively unchanged in transit between the upstream and downstream detector.

It follows that fluctuations in the signals from these detectors are highly correlated and have a magnitude given by the second central moment of the Poisson distribution (Eq. C.7): var (N) = $\bar{N}$. Consequently,

$$\mathrm{var}(S)/S^2 = 1/\bar{N} = \left(\frac{V_p}{V_D\bar{\phi}}\right). \qquad \text{C.8}$$

To visualize this, we may think of the traffic on a freeway, where the vehicle count at two stations separated by a known distance could similarly be cross correlated to obtain the mean speed of traffic.

For a higher value of the solid loading or volume fraction, one may expect, on one hand, that collisions will play an increasingly important role in determining the rate of change of N_i, while on the other hand, the distribution will begin to deviate from the Poisson law (Eq. C.7), due to clustering. Clusters tend to form when particles can stick together, which may be promoted by electric charging. As a result, the variance increases, hence, the covariance or cross-correlation function (CCF) becomes stronger (however, it also may broaden as clusters tend to travel more slowly). For glass beads, this type of clustering is not an issue. Rather, clustering develops like grouping in vehicular traffic, once a certain density is exceeded, and may also be produced at the mixing tee. At mean solid velocities of the order of 20 m/s, the length of such groupings amounts to several meters, as suggested also by the peak shapes of Fig. 4.2.1.

The probability distribution that determines N_i can be expressed by a Polya law, and that law in turn can be expanded as a Poisson distribution multiplied by a correction series that results in enlarging the variance. For present purposes, this effect is minimal for the type of clustering that is produced in oscillatory release from the mixing tee; hence, a Poisson distribution may be assumed with negligible error.

To predict the change in particle number within the moving detector volume, we may invoke a binary collision model that gives the collision rate density dn_c/dt,

$$\frac{dn_c}{dt} = n^2\sigma\bar{u} \qquad \text{C.9}$$

where n = local particle, σ = collision cross section, approximately equal to πd_p^2 for particles of diameter d_p, and $\bar{u}$ = average random velocity of the particles along the collision path, in a coordinate frame that moves with $\bar{v}_p$. Assuming now that each collision removes both particles from the moving volume V_D through outscattering, $dn/dt = -2dn_c/dt$, Eq. C.9 can be solved for $n(t)$,

$$n(t) = \frac{n(0)}{[1 + 2n(0)\sigma\bar{u}t]} .$$

This yields the particle number N(t),

$$N(t) = \frac{N(0)}{1 + 2\sigma\bar{u}N(0)t/V_D} . \qquad \text{C.10}$$

Now let $N(0) = N_{ui}$, a sample at the upstream detector, and let $t = d_e/\bar{v}_p$, then Eq. C.10 yields the prediction that a number ΔN_i

$$\Delta N_i = \frac{bN_{ui}^2}{(1 + bN_{ui})} \qquad \text{C.11}$$

will be removed from the sample in transit to the downstream detector site, through outscattering. The collective parameter b introduced in Eq. C.11 comes to

$$b = (\bar{u}/\bar{v}_p)\left(\frac{2\sigma d_e}{V_D}\right) . \qquad \text{C.12}$$

On the average, the loss ΔN_i must be compensated for by inscattering. Let ΔN_i be the inscattered number for the ith sample. Then, from conservation of mass,

$$\overline{\Delta N} = \overline{\Delta N'} \text{ and } \overline{N_u} = \overline{N_d} \qquad \text{C.13}$$

Moreover, since the redistribution of particles is a stationary Markoff process, it further follows that

$$\mathrm{var}(N_u) = \mathrm{var}(N_d) . \qquad \text{C.14}$$

Now Eq. C.11 together with the observation that the sample offset k_o comes to

$$k_o = f_s \frac{d_e}{\bar{v}_p} ,$$

where f_s = sampling frequency, directly yields the relation

$$N_{i+k,\,d} = N_{iu} + \Delta N_i' - \Delta N_i = \frac{N_{iu}}{(1 + bN_{iu})} + \Delta N_i' . \qquad \text{C.15}$$

This relation can now be directly applied to a computation of the covariance

$$\mathrm{cov}(S_u, S_d)_k = A_u A_d m^2 \; \overline{(N_{iu} - \bar{N})\,(N_{i+k,d} - \bar{N})} \qquad \text{C.16}$$

at the offset of k_o samples that corresponds to the transit time. The bar denotes an average by summing over the index i, equivalent to a time average.

Equation C.16 involves nonlinear averaging of fluctuating quantities, which can be provided through Taylor expansions. For example,

$$\overline{\frac{N_i}{1 + bN_i}} = \overline{\bar{N}\left(1 + \frac{\delta_i}{\bar{N}}\right)\left[1 - \frac{bS_i}{1 + b\bar{N}} + \frac{b^2\delta_i^2}{(1 + b\bar{N})^2} \ldots\right]/(1 + bN)}$$

$$= \bar{N}[1 - b\mathrm{var}(N)/\bar{N}(1 + b\bar{N})^2]/(1 + b\bar{N}) \;, \qquad \text{C.17}$$

where

$$\delta_i = N_i - \bar{N} \;, \qquad \text{C.18}$$

hence,

$$\overline{\delta^2} = \mathrm{var}(N) \;. \qquad \text{C.19}$$

This yields, after some arithmetic manipulations, the covariance

$$\mathrm{cov}(S_u, S_d)_k = \frac{A_u A_d m^2 \mathrm{var}(N)}{(1 + b\bar{N})^2} \;. \qquad \text{C.20}$$

From Eq. C.6,

$$\mathrm{var}(S_j)^{1/2} = A_j m \mathrm{var}(N)^{1/2}, \; j = u,d \;. \qquad \text{C.21}$$

Equation C.20 thus can be written

$$\mathrm{cov}(S_u, S_d)_k = \frac{[\mathrm{var}(S_u)\mathrm{var}(S_d)]^{1/2}}{(1 + b\bar{N})^2} \qquad \text{C.22}$$

This identifies the cross correlation coefficient

$$\rho_{ud} = (1 + b\bar{N})^{-2} = \frac{\mathrm{cov}(S_u, S_d)_k}{\mathrm{var}(S_u)\mathrm{var}(S_d)^{1/2}} . \qquad \text{C.23}$$

The quantity $b\bar{N}$ that determines the coefficient comes to

$$b\bar{N} = \frac{\bar{u}}{\bar{v}_p} \frac{12\phi\, d_e}{d} . \qquad \text{C.24}$$

It is noteworthy that this quantity does not depend on the detection volume or length, but increases with d_e and the solid fraction while declining with the particle diameter. Estimating the velocity ratio $\bar{u}/v_p$ to be about 0.02, letting $\phi = 0.01$, $d_e = 10$ cm and $d = 0.1$ cm, one obtains a correlation coefficient of 0.65, which is roughly, the same as what has been observed (Sec. 4.2).

Equations C.22 and C.23 predict that the correlation will decline very rapidly for increased loading, since that not only raises the solid fraction but also tends to boost the random velocity component $\bar{u}$. Moreover, the correlation should vanish in the limit of micron particle size (fine dust). Dust tends to travel at the velocity of the entraining fluid or gas, and since its contribution to the CCF of a mixed particle/dust solid is virtually nil, the correlation flowmeter would slightly underpredict the actual solid feedrate. However, many solids produce fines that tend to form clusters, causing the variance to become larger than that estimated in Eq. C.9 and thus compensating for the correlation coefficient.

The decline of the correlation with increasing distance d_e would favor a close location of the sensors, however the accuracy of the measurement in terms of, say a 0.1 channel width that can just be determined through interpolation must be considered:

$$e = \frac{0.1}{k_o} = \frac{0.1\bar{v}_p}{f_s\, d_e} . \qquad \text{C.25}$$

To make that error fall within 0.01, a minimum value of d_e at $f_s = 5$ kHz and $\bar{v}_p = 25$ m/s would be 5 cm.

A final point is the maximization of the signal variance, suggesting

is relatively small. Again, that stratagem eventually fails when the signal strength (capacity difference) becomes weak in comparison to random input noise within the bandwidth that is encompassed by the correlated fluctuations.

In sum, a number of relations between flow parameters and detection system parameters have been developed, using a binary collision model to account for the decline in the correlation coefficient. This model predicts a behavior roughly in agreement with some preliminary observations. These equations allow some useful conclusions with respect to optimizing the system design.

APPENDIX D
THE EFFECT OF A LINER ON THE CAPACITIVE FLOWMETER SOLID VOLUME FRACTION MEASUREMENT

The external electrode scheme used for the capacitive flowmeter (CF) is immune to erosion and the mullite liner can be shown to have negligible effect on the CF SVF measurement. Consider two capacitors as shown

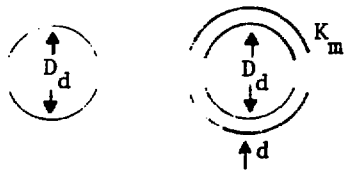

d = the thickness of the liner
D = the electrode separation, and
K_m = the liner dielectric constant.

For this parallel plate arrangement, the following terms are defined:

C_F and C_F^* = D and CF capacitance, respectively, with no solids,
C_M and C_M^* = D and CF capacitance, respectively, with solids, and
C_m = liner capacitance.

The total capacitance of the CF is the series combination of C_m (twice) and the capacitance between the electrodes. The electrode dimensions and separation are equal for both instruments. For the case with no solids, the capacitance is

$$C_F^* = \frac{1}{\frac{1}{C_m} + \frac{1}{C_m} + \frac{1}{C_F}} = \frac{C_m\, C_F}{C_m + 2C_F}. \qquad \text{D.1}$$

For the case with solids, the capacitance is

$$C_M^* = \frac{1}{\frac{1}{C_m} + \frac{1}{C_m} + \frac{1}{C_M}} = \frac{C_m\, C_M}{C_m + 2C_M} \qquad \text{D.2}$$

The relative change in capacitance is given by

$$\frac{C_M^* - C_F^*}{C_F^*} = \frac{C_M^*}{C_F^*} - 1 = \frac{C_M\,(C_m + 2C_F)}{C_F\,(C_m + 2C_M)} - 1$$

$$= \frac{C_m\,(C_M - C_F)}{C_F\,(C_m + 2C_M)} = \frac{\frac{C_M}{C_F} - 1}{2\,\frac{C_M}{C_m} + 1} \qquad \text{D.3}$$

If the denominator term, $2C_M/C_m$, is <1, the relative change in capacitance for both capacitive instruments would be identical. The question arises as to the magnitude of this error term. The liner capacitance is given by

$$\frac{K_\ell A}{d} \qquad \text{D.4}$$

where A = the electrode area and the densitometer experimental results declare that

$$\frac{C_M}{C_F} - 1 = 2.2\phi \qquad \text{D.5}$$

and thus $C_M = (1 + 2.2\phi)\ C_F$ D.6

The densitometer capacitance with no solids, C, is given by

$$C_F = \frac{A}{D} \qquad \text{D.7}$$

Hence, the error term, $2C_M/C_m$, is

$$2\ \frac{C_M}{C_m} = 2(1 + 2.2\phi)\ \frac{d}{D\ K_\ell} \qquad \text{D.8}$$

For a 0.32 cm (0.12 in.) liner, 5.40 cm (2.12 in.) electrode spacing, and a mullite dielectric constant of 6, the error term is given by

$$2\ \frac{C_M}{C_m} = 0.02\ (1 + 2.2\phi) \qquad \text{D.9}$$

For a SVF of 0.01 which is (typical of these tests, as shown in Table 2.3.2), the error term, $2C_M/C_m$, is

$$2\ \frac{C_M}{C_m} = 0.02 \qquad \text{D.10}$$

and the SVF measurement by the CF is thus approximately 2% lower than that by the DM. This difference is a small price to pay for electrodes never being eroded.

APPENDIX E
AMPLITUDE DEMODULATED SIGNAL THEORY FOR PARTICLE VELOCITY MEASUREMENT WITH A CAPACITIVE FLOWMETER

The amplitude-modulated consequence experienced by the CF with a solid/gas flow is related to the total current, I, sensed by the pre-amplifier and is given by

$$I = \frac{dQ}{\Delta t} = \frac{d}{dt}\left[(C_F + \Delta C)\ V_{osc}\right] \qquad \text{E.1}$$

where

C_F = capacitance of the CF electrode pair without solids,

ΔC = change in capacitance due to the solids, and

V_{osc} = the applied CF voltage.

With the applied voltage, $V_p \sin\omega t$ where $\omega = 2\pi(100\text{kHz})$, across the electrodes and a change of capacitance at the CF, the current I is

$$I = C_F\omega V_{Pk} \cos \omega t + V_{Pk}\sin \omega t \left(\frac{d\ C_f}{dt}\right) + \Delta C_F\omega V_{Pk}\cos \omega t + V_{Pk}\sin \omega t \left(\frac{d\Delta C}{dt}\right). \qquad \text{E.2}$$

The first term is a steady-state term and the second term is zero if the dielectric constant of air and the physical dimensions of the CF electrode arrangement remain constant. If it is assumed that the change in capacitance due to the solids, ΔC, is $k \sin \omega_a t$ (which can be the first term of a Fourier series expansion of an arbitrary function), then the third term transforms to

$$\Delta C\omega V_{Pk}\cos \omega t = \frac{kV_{Pk}\omega}{2}\left[\sin (\omega + \omega_a)t + \sin (\omega - \omega_a)t\right] \qquad \text{E.3}$$

and the fourth term transforms to

$$V_{Pk}\sin \omega t \left(\frac{d\Delta c}{dt}\right) = \frac{k\omega_a V_{Pk}}{2}\left[\sin(\omega + \omega_a)\ t + \sin(\omega - \omega_a)t\right] \qquad \text{E.4}$$

These terms are recognized as amplitude-modulated effects that can be demodulated and cross-correlated to measure particle velocity.

REFERENCES

1. L. R. Dates and J. P. Bobis, "The ANL Solid/Gas Flow Test Facility," Argonne National Laboratory Report ANL/FE-82-22 (1982).

2. G. Arnason and D. E. Stock, "Dispension of Particles in Turbulent Pipe Flow," J. Exper. in Fluids (Nov. 1983).

3. K. Porges, R. J. Armani, E. Bennett, J. P. Bobis, W. E. Brewer, and L. T. Bernovich, "A Solid Velocity Measurement in Gas-Solid Flow by the 'Hot Particle' Method," American Physical Society 36th Annual Meeting of the Division of Fluid Dynamics, Houston, TX, (Nov. 20-22, 1983).

4. A. Fortier and C. P. Chen, "Ecoulement Turbulent Stationnaire Biphasique Air-Solide dens un Tube Cylindrique a Forte Concentration Massique," J. de Mecanique 15, 1 (1976).

5. Z. M. Johnson and J. P. Bobis, Argonne National Laboratory, Private Communication, 1984.

6. M. T. Shu, C. B. Weinberger and Y. H. Lee, "A Simple Capacitance Sensor for Void Fraction Measurement in Two-Phase Flow," Ind. Eng. Chem. Fundam. 21, 181-183 (1982).

7. G. A. Irons and J. S. Chang, "Particle Fraction and Velocity Measurement in Gas-Powder Streams by Capacitance Transducers," Int. J. Multiphase Flow 9 (3) 289-297 (1983).

8. W. W. Managan, J. J. Eichholz, and R. W. Doering, "Field Test of a Capacitive Transducer for Density/Velocity (Mass Flow) Measurement on the HYGAS Pilot Plant Solvent/Coal Feedline," Argonne National Laboratory Report ANL-78-62, 193-221 (1978).

9. J. P. Bobis, W. E. Brewer, J. R. McQuinn, N. M. O'Fallon, and R. J. Armani, "Performance Characteristics of a Capacitive Flowmeter on the ANL Solid/Gas Flow Test Facility," Argonne National Laboratory Report ANL-82-62, CONF-820612, pp. 50-64 (1982).

10. T. E. Murphy, M. J. Post, J. P. Bobis, and H. L. Farley, "Real-Time Velocity Measurements of Airborne Solids Flow with an Industrial Correlation Flowmeter," Argonne National Laboratory Report ANL-82-62, CONF-820612, pp. 65-76 (1982).

11. J. P. Bobis, E. D. Doss, A. C. Raptis, W. E. Brewer, and L. T. Bernovich, "Experimental Results of Capacitive Flowmeter and Analytical Modeling of Solid-gas Flow Mixture at ANL S/GFTF," Proc. Midwest Universities Energy Consortium Conf. on Elec. Utility Research C. Bullard, and P. Womeldorft), pp. 287-304 (April 1984).

12. J. P. Bobis, S. H. Sheen, K. G. Porges, H. B. Karplus, M. M. Farahat, W. E. Brewer, N. M. O'Fallon, and A. C. Raptis, "Preliminary Report on Development of Non-intrusive Flow Instrumentation at the ANL Solid-Liquid Test Facility," Argonne National Laboratory Report ANL/FE-83-18 (Dec. 1983).

13. K. G. Porges and J. P. Bobis, (in preparation).

14. M. S. Beck, G. Calvert, J. H. Hobson, K. T. Lee, and P. T. Mendies, "Total Volume and Component Flow Measurement in Industrial Slurries and Suspensions Using Correlation Techniques," Trans. of the Institute of Measurement and Control 4 (8) (Aug. 1971).

15. W. Balachandran and M. S. Beck, "Solids Concentration Measurement and Flow Measurement of Slurries and Sludges Using Ultrasonic Sensor with Random Data Analysis," Argonne National Laboratory Report ANL-81-62, CONF-810607, 443-451 (1981).

16. R. Aris, "On the Dispersion of a Solute in a Fluid Flowing Through a Tube," Proc. Roy. Soc. London A-237, 67 (1957).

17. R. Aris, "On the Dispersion of a Solute by Diffusion, Convection, and Exchange Between Phases," Proc. Roy. Soc. London A-252, 538 (1959).

18. G. I. Taylor, "The Dispersion of Matter in Matter in Turbulent Flow Through a Pipe," Proc. Roy. Soc. London A-223, p. 446 (1954).

19. K. G. A. Porges, "Flow Characterization and Calibration of Slurries by Pulsed Neutron Activation," Argonne National Laboratory Report ANL/FE-84-16 (July 1984).

20. M. Merilo, R. L. Dechene, and M. W. Cichowlas, "Void Fraction Measurement with a Rotating Electric Field Conductance Gauge," J. of Heat Transfer, 99 (2) (1977).

21. M. S. A. Abouelwafa and E. J. M. Kendall, "Analysis and Design of Helical Capacitance Sensors for Volume Fraction Determination," Rev. of Scientific Inst. 50(7): 872 (July 1979).

22. G. A. Gregory and L. Mattar, "An In Situ Volume Fraction Sensor for Two-Phase Flows of Non-Electrolytes," J. of Canadian Petroleum Technology (April-June 1973).

23. P. R. Bevington, "Data Reduction and Error Analysis for the Physical Sciences," McGraw Hill, New York (1969).

24. Instrumentation and Control for Fossil Energy, Annual Report, FY 1985, Argonne National Laboratory, ANL/FE-85-17, (1985).

25. F. Mesch, R. Fritsche, and H. Kipphan, "Transit Time Correlation - A Survey on Its Applications to Measuring Transport Phenomena," Transactions of the ASME, p. 414 (Dec. 1974).

26. R. S. Flemons, "A New Nonintrusive Flowmeter," U.S. Natl. Bur. Stand. Spec. Publ. 484, p. 319 (1977).

27. A. C. Raptis, S. H. Sheen, P. D. Roach, and J. F. Mesch, "Acoustic Noise Background and Sound Transmission Tests in a Slurry Line at the HYGAS Pilot Plant," Argonne National Laboratory Report ANL/FE-49622-TM04 (1979).

28. A. C. Raptis and S. H. Sheen, "Ultrasonic Properties of Coal Slurries and Flow Measurements by Cross-correlation," IEEE Trans. on Sonics and Ultrasonics, SV-28 (4): 248 (1981).

29. R. G. Green, S. H. Foo and J. G. Phillips, "Flow Measurement for Optimizing the Feed Rate of Pulverized Fuel to Coal-Fired Boiler," Argonne National Laboratory Report ANL-81-62, CONF-810607, 180-185 (1981).

30. S. H. Sheen and A. C. Raptis, "Potential Acoustic Techniques for Monitoring Mass Flow Rate in Coal-air Ducts," Midwest Universities Energy Consortium Conf. on Electrical Utility Research (1984).

31. S. H. Sheen, A. C. Raptis, J. P. Bobis, S. Lee, and T. Simpson, "Evaluation of Active Ultrasonic Cross-correlation Technique in Coal/Liquid Pipe Flow Measurements," Argonne National Laboratory Report ANL/FE 84-19 (Oct. 1984).

32. M. P. Mathur and G. E. Klinzing, "Measurement of Particle and Slip Velocities in Coal/Gas System," Annual Meeting AIChE, Los Angeles (1982).

33. J. S. Bendat and A. G. Piersol, "Engineering Applications of Correlation and Spectral Analysis," John Wiley and Sons, New York (1980).

34. O. F. Mosotti, "Effetti di Polarisazione Nelle Materie Sull'influenza di un Campo Elettrico," Mem. Soc. Ital. di Sci. (Modena) 14 49 (1850).

35. H. A. Lorentz, "The Theory of Electrons," Leipzig: B. G. Teubner (1909); New York: Dover Publications Inc., (1952); a series of lectures on selected topics in classical electron theory.

36. J. C. Maxell, "Treatise on Electricity and Magnetism," 3d Ed; Oxford (1904).

37. G. Strutt Lord Rayleigh, "On the Influence of Obstacles Arranged in Rectangular Order Upon the Properties of a Medium," Phil Mag 34, 481 (1892).

38. W. F. Brown, "Dielectric Constants of Non-polar Fluids, I: Theory," Chem. Phys. 18 1193 (1950); "II: Analysis of Experimental Data," ibid 1200; "Solid Mixture Permittivities," Jour. Chem. Phys. 23, 1514 (1955).

39. C. J. F. Boettcher, "Theory of Electric Polarization," 2d Ed., Elsevier, Amsterdam (1972).

40. L. Onsager, J. Amer. Chem. Soc., pp. 1486-1493 (1936).

41. D. A. G. Bruggeman, "Berechnung Verschiedener Physikalischer Konstanten von heterogenen Substanzen," Annal. Phys. 24, 636 (1935).

42. R. Landauer, "The Electrical Resistance of Binary Metallic Mixtures," J. Appl. Phys. 23, 779 (1952).

43. K. Lichtenecker, "Die Dielektrizitaetskonstante von Mischungen," Physikal. Ztschr. 28, 417 (1927).

Distribution for ANL/FE-86-4

Internal:

W. E. Brewer
J. P. Bobis (6)
E. D. Doss
H. Drucker
W. A. Ellingson
P. S. Farber
N. Gopalsami
R. E. Holtz
A. B. Krisciunas
W. P. Lawrence
K. M. Myles
N. M. O'Fallon
M. Petrick
W. F. Podolski
K. G. Porges (6)
A. C. Raptis (10)
S. H. Sheen
M. Srinivasan
C. E. Till
R. W. Weeks
S. K. Zussman
ANL Contract File
ANL Libraries
ANL Patent Dept.
TIS Files (6)

External:

DOE-TIC, for distribution per UC-90a (160)
Manager, Chicago Operations Office, DOE
F. Herbaty, DOE-CH
M. Zahid, DOE-CH
Materials and Components Technology Division Review Committee:
  Dr. C. Benjamin Alcock, University of Toronto, Canada
  Dr. Paul G. Shewmon, Ohio State University, Ohio
D. L. Basdekas, Office of Nuclear Regulatory Research, USNRC
J. Byam, Morgantown Energy Technology Center, USDOE
J. Carr, Office of Fossil Energy, USDOE
C. S. Chen, U. Akron
J. S. Coleman, Office of Energy Research, USDOE
A. C. Dolbec, Electric Power Research Institute, Palo Alto
P. J. Ebert, Office of Energy Research, USDOE
F. Karlson, Electric Power Research Institute, Palo Alto
T. Keech, Morgantown Energy Technology Center, USDOE
J. Kovach, Morgantown Energy Technology Center, USDOE
S. Lee, Pittsburgh Energy Technology Center, USDOE
M. McMillian, Morgantown Energy Technology Center, USDOE
C. Nakaishi, Morgantown Energy Technology Center, USDOE
J. Notestein, Morgantown Energy Technology Center, USDOE
W. H. Piispanen, Battelle-Columbus Laboratories
S. Sami, Southern Illinois U., Carbondale
T. Schmidt, Shell Development, Houston
M. A. Scott, U. Tennessee Space Institute, Tullahoma
F. E. Senftle, U.S. Geological Survey, Washington, D.C.
V. Sethi, Kentucky Center for Energy Research, Lexington
T. Simpson, Office of Fossil Energy, USDOE
M. Singer, Office of Fossil Energy, USDOE
A. B. Tanner, U. S. Geological Survey, Washington, D.C.
O. Tassicker, Electric Power Research Institute, Palo Alto
T. Torkos, Pittsburgh Energy Technology Center, USDOE
E. S. Van Valkenburg, Leeds & Northrup Co., North Wales, PA
J. Wilson, Morgantown Energy Technology Center, USDOE